OPIS
Listă 6 publicaţii relevante

Candidat pentru obţinerea atestatului de abilitare în Domeniul Medicină:

LEBOVICI ANDREI

1. Claudia-Gabriela Moldovanu, Bianca Petresc, **Andrei Lebovici**, Attila Tamas-Szora, Mihai Suciu, Nicolae Crisan, Paul Medan, Mircea Marian Buruian. Differentiation of Clear Cell Renal Cell Carcinoma from other Renal Cell Carcinoma Subtypes and Benign Oncocytoma Using Quantitative MDCT Enhancement Parameters. Medicina-Lithuania 2020; 56(12p). 10.3390/medicina56110569. WOS:000593197400001. https://www.webofscience.com/wos/woscc/full-record/WOS:000593197400001. (FI = 2.43; Q2) **Pag 2 - 13**
2. Andrei Lebovici, Csaba Csutak, Paula Popa, Nicolae Crișan, Mihai Suciu, Bogdan Feciche, Iulia Andraș, Paul-Andrei Ștefan, Diana Sorina Feier. Magnetic resonance imaging characteristics of chronic prostatitis in patients under the age of 50: is it more than the eye can see? Acta radiologica 2021; 63:839-846. 10.1177/02841851211010397. WOS:000680728000001. https://www.webofscience.com/wos/woscc/full-record/WOS:000680728000001 (FI = 1.7; Q3) **Pag 14 -21**
3. Claudia-Gabriela Moldovanu, Bianca Boca, Andrei Lebovici, Attila Tamas-Szora, Diana Sorina Feier, Nicolae Crisan, Iulia Andras, Mircea Marian Buruian. Preoperative Predicting the WHO/ISUP Nuclear Grade of Clear Cell Renal Cell Carcinoma by Computed Tomography-Based Radiomics Features. Journal of personal medicine 2021; 11(16p). 10.3390/jpm11010008. WOS:000610343400001. https://www.webofscience.com/wos/woscc/full-record/WOS:000610343400001. (FI = 3.508; Q2) **Pag 22-37**
4. Roxana-Adelina Ștefan, Paul-Andrei Ștefan, Carmen Mihaela Mihu, Csaba Csutak, Carmen Stanca Melincovici, Carmen Bianca Crivii, Andrei Mihai Maluțan, Liviu Hîțu, **Andrei Lebovici.** Ultrasonography in the Differentiation of Endometriomas from Hemorrhagic Ovarian Cysts: The Role of Texture Analysis. Journal of personal medicine 2021; 11(15p). 10.3390/jpm11070611. WOS:000676608600001. https://www.webofscience.com/wos/woscc/full-record/WOS:000676608600001 (FI = 3.508; Q2) **Pag 38-52**
5. Caravan I, Ciortea CA, Contis A, Lebovici A. Diagnostic value of apparent diffusion coefficient in differentiating between high-grade gliomas and brain metastases. Acta Radiol. 2018 May;59(5):599-605. WOS:000429744900013. (ISI IF= 1.586 Q3) https://www.webofscience.com/wos/woscc/full-record/WOS:000429744900013 **Pag 53-59**
6. Csaba Csutak, Paul-Andrei Ștefan, Lavinia Manuela Lenghel, Cezar Octavian Moroșanu, Roxana-Adelina Lupean, Larisa Șimonca, Carmen Mihaela Mihu, **Andrei Lebovici**. Differentiating High-Grade Gliomas from Brain Metastases at Magnetic Resonance: The Role of Texture Analysis of the Peritumoral Zone. Brain Sci. 2020 Sep 16;10(9):E638. doi: 10.3390/brainsci10090638. WOS:000580778000001. **(ISI IF= 3.394 Q3)** https://www.webofscience.com/wos/woscc/full-record/WOS:000580778000001 **Pag 60-76**

medicina

Article

Differentiation of Clear Cell Renal Cell Carcinoma from other Renal Cell Carcinoma Subtypes and Benign Oncocytoma Using Quantitative MDCT Enhancement Parameters

Claudia-Gabriela Moldovanu [1,2], Bianca Petresc [1,2], Andrei Lebovici [2,3,*], Attila Tamas-Szora [4], Mihai Suciu [5], Nicolae Crisan [6,7], Paul Medan [7] and Mircea Marian Buruian [1,8]

1 Department of Radiology and Medical Imaging, Faculty of Medicine, George Emil Palade University of Medicine, Pharmacy, Science and Technology of Târgu Mureș, 540139 Târgu Mureș, Romania; moldovanu_claudia@yahoo.com (C.-G.M.); bianca.petresc@gmail.com (B.P.); mircea.buruian@umfst.ro (M.M.B.)
2 Department of Radiology, Emergency Clinical County Hospital of Cluj-Napoca, 400006 Cluj-Napoca, Romania
3 Department of Radiology, Faculty of Medicine, Iuliu Hațieganu University of Medicine and Pharmacy, 400012 Cluj-Napoca, Romania
4 Department of Radiology, Clinical Municipal Hospital, 400139 Cluj-Napoca, Romania; attitamas@yahoo.com
5 Department of Urology, Clinical Institute of Urology and Kidney Transplant, 400000 Cluj-Napoca, Romania; suciu_umf@yahoo.com
6 Department of Urology, Faculty of Medicine, Iuliu Hațieganu University of Medicine and Pharmacy, 400012 Cluj-Napoca, Romania; drnicolaecrisan@gmail.com
7 Department of Urology, Municipal Clinical Hospital, 400139 Cluj-Napoca, Romania; medan.paul@gmail.com
8 Department of Radiology, Emergency Clinical County Hospital Târgu Mureș, 540136 Târgu Mureș, Romania
* Correspondence: andrei.lebovici@umfcluj.ro

Received: 5 September 2020; Accepted: 26 October 2020; Published: 28 October 2020

Abstract: *Background and objectives*: The use of non-invasive techniques to predict the histological type of renal masses can avoid a renal mass biopsy, thus being of great clinical interest. The aim of our study was to assess if quantitative multiphasic multidetector computed tomography (MDCT) enhancement patterns of renal masses (malignant and benign) may be useful to enable lesion differentiation by their enhancement characteristics. *Materials and Methods*: A total of 154 renal tumors were retrospectively analyzed with a four-phase MDCT protocol. We studied attenuation values using the values within the most avidly enhancing portion of the tumor (2D analysis) and within the whole tumor volume (3D analysis). A region of interest (ROI) was also placed in the adjacent uninvolved renal cortex to calculate the relative tumor enhancement ratio. *Results*: Significant differences were noted in enhancement and de-enhancement (diminution of attenuation measurements between the postcontrast phases) values by histology. The highest areas under the receiver operating characteristic curves (AUCs) of 0.976 (95% CI: 0.924–0.995) and 0.827 (95% CI: 0.752–0.887), respectively, were demonstrated between clear cell renal cell carcinoma (ccRCC) and papillary RCC (pRCC)/oncocytoma. The 3D analysis allowed the differentiation of ccRCC from chromophobe RCC (chrRCC) with a AUC of 0.643 (95% CI: 0.555–0.724). Wash-out values proved useful only for discrimination between ccRCC and oncocytoma (43.34 vs 64.10, $p < 0.001$). However, the relative tumor enhancement ratio (corticomedullary (CM) and nephrographic phases) proved useful for discrimination between ccRCC, pRCC, and chrRCC, with the values from the CM phase having higher AUCs of 0.973 (95% CI: 0.929–0.993) and 0.799 (95% CI: 0.721–0.864), respectively. *Conclusions*: Our observations point out that imaging features may contribute to providing prognostic information helpful in the management strategy of renal masses.

Keywords: renal cell carcinoma; histological subtypes; oncocytoma; multiphasic multidetector CT (MDCT); quantitative imaging

---

1. Introduction

Globally, the incidence of renal cell carcinoma (RCC) varies widely from region to region, with the highest rates being observed in the Czech Republic and North America [1]. According to the revised 2016 World Health Organization classification of RCCs [2], the major subtypes are clear cell RCC (ccRCC), papillary RCC (pRCC), and chromophobe RCC (chrRCC), which comprise 65–70%, 15–20%, and 5–7% of all RCCs, respectively. Oncocytomas are benign lesions that encompass 3% to 5% of renal adult's neoplasms, and they are the most commonly resected benign renal masses due to misinterpretation at imaging as RCCs [3]. Preoperative classification of RCC into subtypes and recognition of benign lesions has become important because each of them is associated with different treatment choices and prognosis [4,5]. Pre-treatment percutaneous renal mass biopsy is a highly accurate procedure that can be used to identify the histology, differentiate primary from secondary renal masses, and discriminate the less aggressive masses from the more aggressive ones, thus allowing better stratification of patient risk before treatment decisions are made [6]. Lane et al. [7] reported sensitivity for malignancy of 92% and specificity of 90% after more than 2000 renal mass biopsies, with an overall technical failure rate of 5%. Although percutaneous renal mass biopsy remains a valuable method to provide a presurgical histopathologic diagnosis of renal masses, it is an invasive procedure and is not always feasible [8,9].

The aim of our study was to assess if quantitative multiphasic multidetector computed tomography (MDCT) enhancement patterns of renal masses (malignant and benign) may be useful to enable lesion differentiation by their enhancement characteristics.

2. Materials and Methods

2.1. Patients

The Institutional Review Board of Regional Institute of Clinical Municipal Hospital Cluj-Napoca, Romania, approved this retrospective study and waived the requirement for written informed consent (Approval code: Nr. 15/2020; approval date: 11 June 2020). We performed a retrospective analysis in our electronic medical database from January 2017 to June 2020. The inclusion criteria were as follows: patients underwent radical, total, or partial nephrectomy; renal tumor pathologically confirmed (ccRCC, pRCC, chrRCC, oncocytoma); preoperative MDCT with a four-phase renal mass protocol. The exclusion criteria were as follows: other histological types; patients who opted for ablation or active surveillance; the image quality was deemed inadequate due to poor timing of the post-contrast phases or motion artifacts. Finally, 150 patients fulfilled the inclusion criteria with a total of 154 RCC lesions. Three patients had two lesions each (ccRCC subtype), but one had two subtypes of RCC, pRCC in one kidney and ccRCC in the other kidney.

2.2. CT Acquisition and Renal Mass Protocol

All CT examinations were performed by using 64—MDCT (Somatom Sensation 64, Siemens, Erlangen, Germany) helical scanner, with the following parameters: 120 kV variable tube current (200–400 mA, depending on patient size), section collimation, 0.6 mm; table feed, 5 mm/sec; and reconstruction interval, 3 mm. The pitch used with helical scanners was 1. The four-phase MDCT renal mass protocol included an unenhanced (UN) scan and contrast-enhanced acquisitions during the corticomedullary (CM), nephrographic (NP), and excretory (EX) phases. Patients received a power injection of nonionic intravenous contrast material into an antecubital vein at a rate of 3.0 mL/s and an infusion dose of 80–150 mL, and a bolus tracking algorithm (CareBolus, Siemens

Medical Solutions) was used to determine the onset of imaging in the contrast-acquisitions phases. For bolus tracking, a region of interest (ROI) was placed in the thoracoabdominal aorta junction, with a trigger set to begin at 150 HU, and CM phase imaging occurred 30 s, NP phase imaging occurred 90 s, and EX phase imaging occurred 8 min after the threshold level was reached.

2.3. CT Image Analysis

Image analysis was performed by two radiologists, a radiology resident (C.-G.M.) with 4 years of experience in agreement with a senior radiologist with 8 years of experience in the urogenital field (A.T.-S.). All images were reviewed using a workstation monitor for image archiving and the communication system (KODAK Carestream Version 10.2). The two radiologists were blinded by the pathological results.

Firstly, a ROI cursor approximately 0.1 cm^2 in size (2D ROI) was placed in the same location of the tumor on each of the four imaging phases of MDCT in the axial plane (Figure 1). For homogeneous lesions, ROIs were placed in the center of the lesion, and for heterogeneous lesions, the ROIs were placed in the maximally enhancing portion of the solid tumor by visual inspection in each imaging phase, excluding the areas of necrosis, calcification, cystic, or hemorrhagic. Thus, we calculated for each lesion the following measurements: the absolute peak lesion enhancement (CM phase (HU)—UN phase (HU)), absolute peak lesion de-enhancement (CM to NP (CM phase (HU)—NP phase (HU)); and NP to EX (NP phase (HU)—EX phase (HU)); and absolute peak lesion enhancement wash-out (%) using a CT formula developed by Kopp et al. [10].

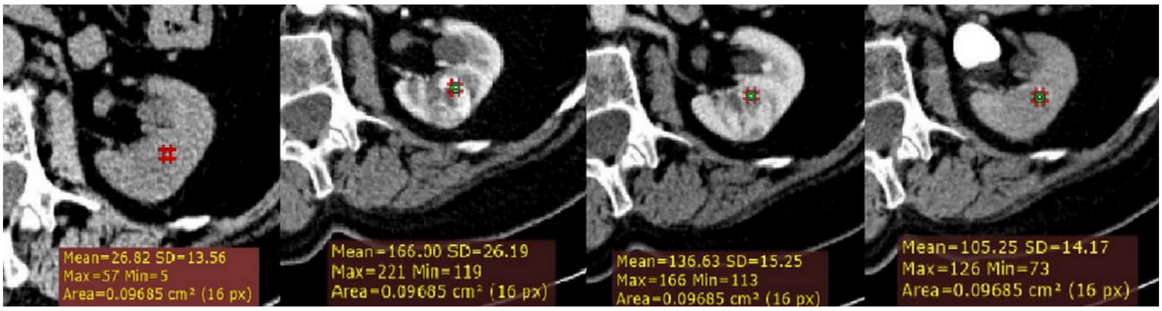

Figure 1. Example of quantitative enhancement measurements from a 72-year-old man with pathological assessment proven clear cell renal cell carcinoma (ccRCC): one circular region of interest (ROI) (0.1 cm^2 in size) was manually selected in the maximally enhancing portion of tumor by visual inspection in each imaging phase (green ROIs).

Secondly, to normalize for variation in attenuation due to individual patient and technical factors, a ROI cursor (0.1 cm2 in size) was placed in the same location of adjacent uninvolved renal cortex, on each of the four imaging phases of MDCT in the axial plane (Figure 2). Next, we calculated for all lesions, the relative tumor enhancement ratio for the CM, NP and EX phase, as follows: (HU tumor enhancement in the postcontrast phase–HU tumor in the unenhanced phase)/(cortex enhancement in the postcontrast phase–cortex in the unenhanced phase).

Thirdly, the multiphase MDCT acquisitions were exported from the picture archiving and communication system (PACS, Carestream, Concord, ON, Canada) and then transferred to an independent workstation for segmentation using an open-source software 3D Slicer, version 4.10.2 (www.slicer.org). Thus, all renal masses were manually segmented, slice by slice, to obtain a three-dimensional (3D) volume of interest (VOI) over the entire tumor (Figure 3). The nephrographic phase was used for segmentation as it provided the adequate demarcation between the tumor and the normal parenchyma. Contouring was carefully drawn within the borders of the tumors, including necrotic, cystic changes, and hemorrhagic areas. The 3D tumor VOI was used as the ROI to calculate the volume enhancement, de-enhancement (HU), and wash-out (%) values over the whole tumor. The same formulas were used for the peak lesion measurements mentioned above.

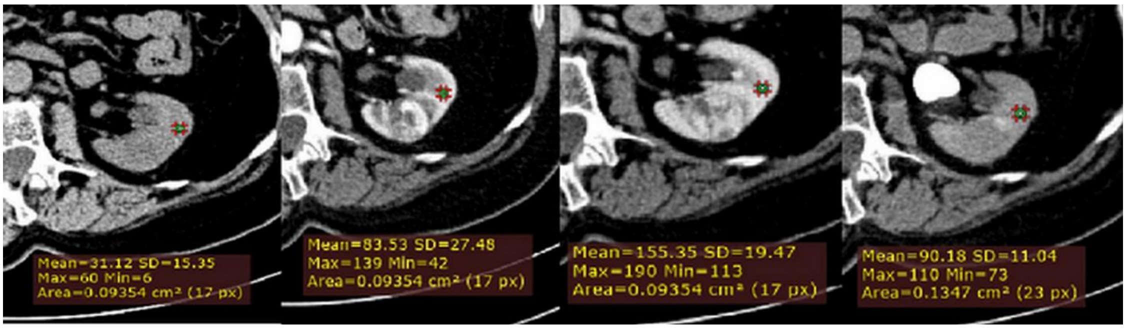

Figure 2. Example of quantitative enhancement measurements from a 72-year-old man with pathological assessment proven ccRCC: a second circular ROI was placed in the adjacent uninvolved renal cortex in each phase (green ROIs).

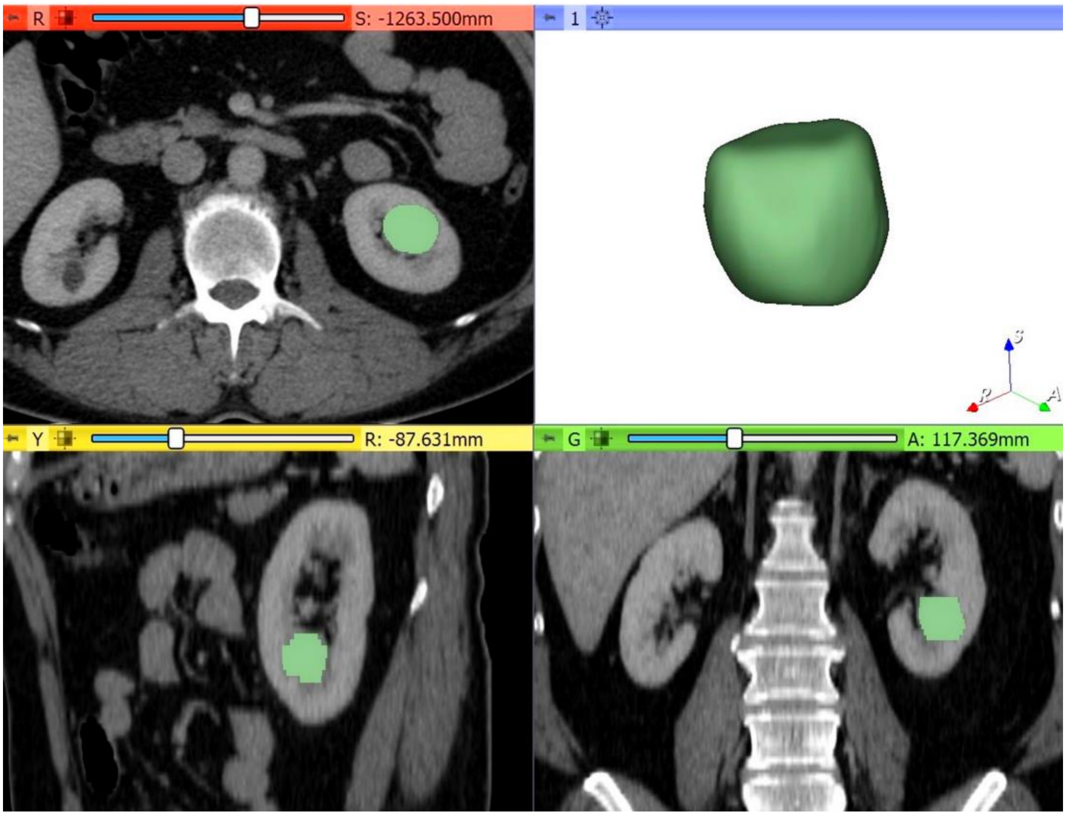

Figure 3. Example of quantitative enhancement measurements from a 52-year-old woman with pathological assessment proven ccRCC: the entire tumor volume was manually contoured in the axial plane in each of the four phases resulting in a 3D tumor volume of interest (VOI) representative of the entire mass (green color = tumoral mass).

2.4. *Interobserver Reproducibility*

The interobserver reliability of the attenuation values from two different ROI groups was evaluated with the intraclass correlation coefficient (ICC). The measurements were performed independently by another senior radiologist (with 8 years of experience in urogenital imaging, A. L.), also blinded by the pathological results. Quantitative enhancement measures with ICC values equal to or greater than 0.75 indicating good reproducibility were included for further analysis.

2.5. Statistical Analysis

Continuous variables with normal distribution were expressed as means ± standard deviation. Normality was tested with the Kolmogorov–Smirnov test. To compare the magnitude of enhancement, de-enhancement, and the % wash-out between ccRCCs and pRCCs, chrRCCs, and benign oncocytomas, we performed ANOVA with post hoc analysis (Dunnett T3 tests).

We also performed ANOVA with post hoc analysis (Dunnett T3 tests) to compare the magnitude of enhancement in the adjacent uninvolved renal cortex among the four histological types from each phase. Receiver operating characteristic (ROC) curves were computed, and corresponding areas under the ROC curves (AUCs) were calculated to compare the diagnostic performance of each independent parameter and the prediction model, respectively. To summarize the potential utility of the features, we calculated sensitivity, specificity, cut-off values, and the corresponding 95% confidence intervals (CI). Categorical variables were analyzed by $\chi 2$ test. A p value of <0.05 was considered statistically significant. All statistical analyses were performed using MedCalc for Windows, version 14.8 (MedCalc Software, Ostend, Belgium) and SPSS Statistics for Windows, version 18.0 (SPSS Inc., Chicago, IL, USA).

3. Results

A total of 150 patients were retrospectively included in this study (mean age 60 years, ±12.4 (standard deviation); range 30–84 years), including 98 men (mean age, 59 years, ±12.3; age range 30–84 years) and 52 women (mean age, 62 years, ±12.6; age range 30–83 years) with 154 renal masses. Of these, 123 were ccRCCs, 10 were pRCCs, 10 were chrRCCs, and 11 were oncocytomas. The clinicopathologic characteristics of our study population are summarized in Table 1.

Table 1. Characteristics of patients and renal lesions. Data are the number of patients (n = 150) and data in parentheses are percentages, except where otherwise indicated. * Data in parentheses are the range.

Characteristic	Clear Cell RCC n = 123 (79)	Papillary RCC n = 10 (6)	Chromophobe RCC n = 10 (6)	Oncocytoma n = 11 (7)
Gender				
Male	85 (55)	7 (5)	5 (3)	5 (3)
Female	38 (25)	3 (3)	5 (3)	6 (4)
Mean age (y) *	61 (30–84)	61 (49–79)	54 (34–71)	56 (34–73)
Method of specimen acquisition				
Partial nephrectomy	21 (14)	2 (2)	1 (1)	5 (3)
Radical nephrectomy	56 (36)	6 (4)	4 (3)	4 (3)
Total nephrectomy	46 (30)	2 (2)	5 (3)	2 (1)
Pathologic tumor stage				
T1a	31 (20)	3 (3)	1 (1)	-
T1b	29 (19)	1 (1)	4 (3)	-
T2a	11 (7)	3 (3)	1 (1)	-
T2b	3 (3)	0 (0)	1 (1)	-
T3a	32 (21)	3 (3)	1 (1)	-
T3b	13 (8)	0 (0)	2 (2)	-
T4	1 (1)	0 (0)	0 (0)	-
Fuhrman grade				
I	26 (17)	2 (2)	1 (1)	-
II	62 (40)	6 (4)	8 (5)	-
III	27 (18)	2 (1)	1 (1)	-
IV	8 (5)	0 (0)	0 (0)	-
Side				
Left	59 (38)	4 (3)	5 (3)	7 (5)
Right	59 (38)	6 (4)	5 (3)	4 (3)
Both kidneys	3 (3)	0 (0)	0 (0)	0 (0)
Lesion size (cm)				
<4	32 (21)	6 (4)	1 (1)	7 (5)
4–7	41 (27)	2 (2)	6 (4)	4 (3)
7–10	37 (24)	1 (1)	1 (1)	0 (0)
>10	13 (8)	1 (1)	2 (1)	0 (0)

First, we analyzed whether the renal masses enhance differently after contrast administration, both for the values obtained by 2D analysis and by 3D analysis. We found that, after contrast administration, oncocytoma had the highest enhancement change, and among the subtypes of RCC, ccRCC displays the highest enhancement, whereas chrRCC enhances moderately and pRCC enhances the least (Figure 4).

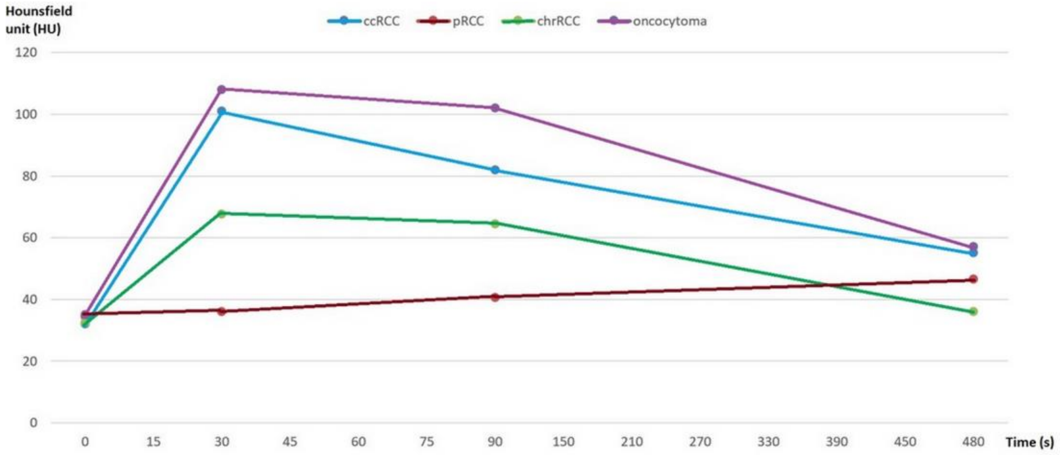

Figure 4. Multiphasic attenuation curves for ccRCCs (n = 123), pRCCs (n = 10), chrRCCs (n = 10), and benign oncocytomas (n = 11). Data points are mean attenuation for each phase. Time: 0 s (UN phase), 30 s (CM phase), 90 s (NP phase), and 480 s (EX phase).

Then, using the formulas mentioned above, quantitative enhancement MDCT measures were compared between ccRCC and other types of renal masses (pRCC, chrRCC, and oncocytoma). According to the standard of the ICC > 0.75 in the interobserver tests, we selected for further analysis only the measurements with good reproducibility. Of the quantitative enhancement MDCT measurements that were compared, we found high reproducibility at most values, except for a few: absolute peak lesion enhancement wash-out values, relative tumor enhancement ratio (EX phase), and 3D tumor volume de-enhancement (CM-NP phase).

We performed univariate analysis to determine if there are any differences between quantitative MDCT parameters and renal lesions (Table 2). Our results show a significant difference in the absolute peak lesion enhancement values between ccRCCs and pRCCs (62.28 vs. 3.40, $p < 0.001$), and ccRCCs and chrRCCs, respectively (62.28 vs. 35.10, $p = 0.010$). Furthermore, the values of absolute peak lesion de-enhancement from the NP to EX phase were significantly different among ccRCCs compared with pRCCs (27.04 vs. −5.10, $p < 0.020$) and oncocytomas, respectively (27.04 vs. 50.64, $p = 0.022$). However, we did not observe significant differences in the absolute peak lesion de-enhancement values from the CM to NP phase between ccRCC and other types of renal masses.

3D tumor ROI enhancement measurements were significantly different between ccRCCs and pRCCs (44.86 vs. 9.80, $p < 0.001$), between ccRCCs and chrRCCs (44.86 vs. 30.20, $p = 0.046$), and between ccRCCs and oncocytomas, respectively (44.86 vs. 74.36, $p = 0.010$). 3D tumor ROI de-enhancement values from the NP phase to the EX phase were also found to be significantly different between ccRCCs and pRCCs (21.93 vs. 3.20, $p = 0.022$), and ccRCCs and oncocytomas, respectively (21.93 vs. 44.64, $p = 0.005$). 3D tumor ROI wash-out measurements were only significant between ccRCCs and oncocytomas (43.34 vs. 64.10, $p < 0.001$).

As suggested previously [11], the measured attenuation of the renal masses should be normalized by using the measured attenuation of the uninvolved renal cortex to ensure that attenuation is independent of the patient or technical variability. Our findings show that the relative tumor enhancement ratio was significantly in the CM phase between ccRCCs and pRCCs (0.97 vs. 0.02,

$p < 0.001$), and chrRCCs, respectively (0.97 vs. 0.36, $p < 0.001$), and in the NP phase between ccRCCs and pRCCs (0.57 vs. 0.01, $p = 0.003$), and chrRCCs, respectively (0.57 vs. 0.34, $p = 0.024$).

Table 2. Quantitative enhancement characteristics of renal masses of the study population. Data are the mean and 95% CI of the mean in parentheses. * p value < 0.05 was considered statistically significant.

Enhancement Characteristic	Clear Cell RCC	Papillary RCC	Chromophobe RCC	Oncocytoma
Absolute peak lesion enhancement (HU)	67.28 (60.49–74.06)	3.40 (−3.45–10.25)	35.10 (18.17–52.03)	81.36 (56.08–106.65)
p vs. clear cell RCC		<0.001 *	0.010 *	0.792
p vs. papillary RCC	<0.001 *		0.012 *	<0.001 *
p vs. chromophobe RCC	0.010 *	0.012 *		0.019 *
p vs. oncocytoma	0.792	<0.001 *	0.019 *	
Absolute peak lesion de-enhancement (HU)				
Corticomedullary to nephrographic	17.67 (13.02–22.31)	−1.20 (−16.01–13.61)	5.00 (−4.55–14.55)	10.18 (−16.95–37.32)
p vs. clear cell RCC		0.101	0.101	0.988
p vs. papillary RCC	0.101		0.958	0.951
p vs. chromophobe RCC	0.101	0.958		0.999
p vs. oncocytoma	0.988	0.951	0.999	
Nephrographic to excretory	27.04 (22.78–31.30)	−5.10 (−23.94–13.74)	23.80 (16.76–30.84)	50.64 (36.55–64.72)
p vs. clear cell RCC		<0.020 *	0.943	0.022 *
p vs. papillary RCC	<0.020 *		0.040 *	<0.001 *
p vs. chromophobe RCC	0.943	0.040 *		0.010 *
p vs. oncocytoma	0.022 *	<0.001 *	0.010 *	
Relative tumor enhancement ratio				
Corticomedullary phase	0.97 (0.78–1.17)	0.02 (−0.07–0.12)	0.36 (0.19–0.53)	0.76 (0.49–1.02)
p vs. clear cell RCC		<0.001 *	<0.001 *	0.655
p vs. papillary RCC	<0.001 *		0.008 *	<0.001 *
p vs. chromophobe RCC	<0.001 *	0.008 *		0.069
p vs. oncocytoma	0.655	<0.001 *	0.069	
Nephrographic phase	0.57 (0.50–0.63)	0.01 (−0.23–0.267)	0.34 (0.20–0.47)	0.77 (0.42–1.11)
p vs. clear cell RCC		0.003 *	0.024 *	0.743
p vs. papillary RCC	0.003 *		0.119	0.005 *
p vs. chromophobe RCC	0.024 *	0.119		0.112
p vs. oncocytoma	0.743	0.005 *	0.112	
3D tumor volume enhancement (HU)	44.86 (40.08–49.64)	9.80 (4.88–14.72)	30.20 (20.67–39.73)	74.36 (58.65–90.07)
p vs. clear cell RCC		<0.001 *	0.046 *	0.010 *
p vs. papillary RCC	<0.001 *		0.005 *	<0.001 *
p vs. chromophobe RCC	0.046 *	0.005 *		<0.001 *
p vs. oncocytoma	0.010 *	<0.001 *	<0.001 *	
3D tumor volume de-enhancement (HU)				
Nephrographic to excretory	21.93 (18.86–25.01)	3.20 (−7.91–14.31)	13.60 (7.00–20.20)	44.64 (33.51–55.77)
p vs. clear cell RCC		0.022 *	0.125	0.005 *
p vs. papillary RCC	0.022 *		0.395	<0.001 *
p vs. chromophobe RCC	0.125	0.395		<0.001 *
p vs. oncocytoma	0.022 *	<0.001 *	<0.001*	
3D tumor volume enhancement wash-out (%)	43.34 (37.79–48.89)	−5.33 (−73.72–63.05)	38.97 (15.25–62.69)	64.10 (58.71–69.48)
p vs. clear cell RCC		0.540	0.999	<0.001 *
p vs. papillary RCC	0.540		0.672	0.220
p vs. chromophobe RCC	0.999	0.672		0.199
p vs. oncocytoma	<0.001 *	0.220	0.199	

Furthermore, to discriminate ccRCC from pRCC, chrRCC, and oncocytoma, all the statistically significant different measurements resulted in AUCs > 0.6 (Figure 5, Table 3). To differentiate between ccRCC and pRCC, absolute peak lesion enhancement measurement demonstrated the highest AUC of 0.976 (95% confidence interval (CI): 0.924–0.995) with 92.7% sensitivity and 100% specificity, when using 17 HU as the cutoff value. Between ccRCC and chrRCC, relative tumor enhancement ratio CM phase showed the highest AUC of 0.799 (95% CI: 0.721–0.864) with 50.4% sensitivity and 100% specificity, when using 0.72 as the cutoff value. Regarding the differentiation between ccRCC and oncocytoma, 3D tumor ROI de-enhancement NP to EX phase measurement had the highest AUC of 0.827 (95% CI: 0.752–0.887) with 74.8% sensitivity and 81.8% specificity, when using 33 HU as the cutoff value.

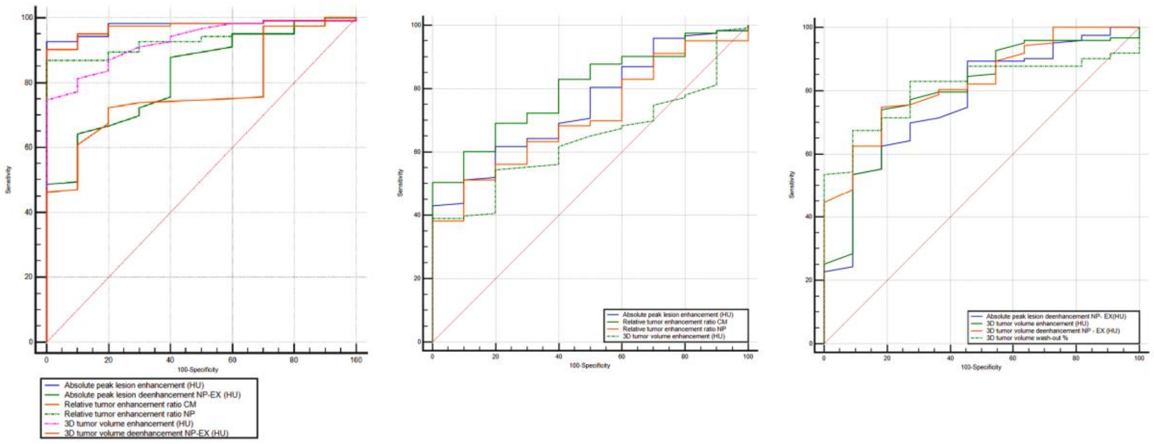

Figure 5. Receiver operating characteristic (ROC) curves for the combination of quantitative features for differentiation of ccRCC from other RCC subtypes (pRCC and chrRCC) and benign oncocytoma. RCC, renal cell carcinoma; AUC, area under the ROC curve; NP, nephrographic phase; EX, excretory phase.

Table 3. ROC curves for combination of quantitative features for differentiation of ccRCC from other RCC subtypes (pRCC and chrRCC) and benign oncocytoma. RCC, renal cell carcinoma; AUC, area under the ROC curve; NP, nephrographic phase; EX, excretory phase; * p value < 0.05 was considered statistically significant.

Discrimination of Clear Cell RCC	AUC (95%CI)	* *p* Value	Sensitivity (95%CI)	Specificity (95%CI)	Cutoff Value
From papillary RCC					
Absolute peak lesion enhancement	0.976 (0.924–0.995)	<0.001	92.7 (86.6–96.6)	100 (69.2–100)	17
Absolute peak lesion de-enhancement NP to EX phase	0.825 (0.750–0.886)	<0.020	64.2 (55.1–72.7)	90 (55.5–99.7)	15
Relative tumor enhancement ratio CM phase	0.973 (0.929–0.993)	<0.001	90.2 (83.6–94.9)	100 (69.2–100)	0.21
Relative tumor enhancement ratio NP phase	0.931 (0.874–0.968)	0.003	87 (79.7–92.4)	100 (69.2–100)	0.24
3D tumor volume enhancement	0.928 (0.871–0.966)	<0.001	74.8 (66.2–82.2)	100 (79.2–100)	22
3D tumor volume de-enhancement NP to EX phase	0.778 (0.698–0.846)	0.022	72.4 (63.6–80)	80 (64.2–97.5)	10
From chromophobe RCC					
Absolute peak lesion enhancement	0.759 (0.668–0.821)	0.010	43.1 (34.2–52.3)	100 (69.2–100)	71
Relative tumor enhancement ratio CM phase	0.799 (0.721–0.864)	<0.001	50.4 (41.2–59.5)	100 (69.2–100)	0.72
Relative tumor enhancement ratio NP phase	0.711 (0.626–0.787)	0.024	51.2 (42.0–60.3)	90.0 (55.5–99.7)	0.54
3D tumor volume enhancement	0.643 (0.555–0.724)	0.046	39 (30.4–48.2)	100 (69.2–100)	51
From oncocytoma					
Absolute peak lesion de-enhancement NP to EX phase	0.771 (0.690–0.839)	0.022	53.7 (44.4–62.7)	90.9 (68.7–99.8)	32
3D tumor volume enhancement	0.798 (0.720–0.862)	0.010	74.0 (65.3–81.5)	81.8 (68.2–97.7)	67
3D tumor de-enhancement NP to EX phase	0.827 (0.752–0.887)	0.005	74.8 (66.2–82.2)	81.8 (68.2–97.7)	33
3D tumor volume wash-out	0.798 (0.720–0.862)	<0.001	74 (65.3–81.5)	81.8 (48.2–97.7)	67

4. Discussion

Although the goals of radiologic imaging are to detect and stage renal tumors, in the last decade there has been a substantial clinical interest for preoperative classifications of renal masses subtypes using MDCT quantitative assessments. Since clinical implications and therapeutic strategies may differ for subtypes of renal cortical tumors, the development of noninvasive techniques and markers to predict the histological type of renal masses would be of great clinical interest. The noninvasive characterization of renal masses with images would have some advantages: no additional cost to the patient, no subsequent appointment for additional testing, no added direct procedure-related risk, and it can be used to evaluate the whole tumor (especially important when a heterogeneous tumor is characterized) [12–14].

Our study is one of the few that included 3D tumor ROI for the analysis of attenuation enhancement values. Using a 3D tumor ROI can avoid inter- and intra-observer variability associated with manual placement of ROI [15], especially in heterogeneous tumors [16].

Like the studies conducted by Bird et al. [17] and Zhang et al. [18], we found that after contrast administration, oncocytoma showed the highest enhancement change, and among the subtypes of RCC, ccRCC displayed the highest enhancement, whereas chrRCC enhanced moderately and pRCC enhanced the least. In our study, these results were obtained both when we used a 2D ROI in the most avidly enhancing portion of the tumor and also when we used a 3D ROI representative for the entire tumor to quantify whole lesion enhancement. However, research by Young et al. [19] is in contradiction with these results, which found that the magnitude of the enhancement of ccRCC was significantly greater than that of pRCC, chrRCC, and oncocytoma in all postcontrast phases. This may be due to the different designs of the studies. Young et al. included patients who were not scanned on the same scanner with the same four-phase MDCT protocol and they used subjectively selected smaller ROIs from 2D images so that each level of the enhancement threshold was assessed for statistical analysis.

Most papers [20–29] that have analyzed the association between attenuation values on MDCT and histological types have shown that the magnitude of enhancement at MDCT can help differentiate ccRCC from pRCC, chrRCC, and oncocytoma. Using measurements of quantitative MDCT enhancement values, our study showed that, among solid cortical renal tumors, the greatest utility in terms of differentiations was between ccRCC and pRCC. The ROC analysis showed that absolute peak lesion enhancement values (2D analysis) can discriminate ccRCC and pRCC with the highest AUC of 0.976 (95% CI: 0.924–0.995) when using 17 HU as the cutoff value. Regarding the values of the measurements obtained from 3D ROI (over the whole tumor), our work demonstrates that between ccRCC and pRCC, significant differences are obtained both for the values of volume enhancement, de-enhancement (HU), and wash-out (%). Research by Chen et al. [30] also assessed whole lesion quantitative enhancement parameters, proving significant differences between ccRCC and pRCC on all postcontrast phases.

Kopp et al. [10] proposed a CT wash-out formula for differentiating ccRCC from other renal masses. Their study found rapid wash-out in ccRCC and they did not observe this to be significantly different from that seen in oncocytoma. Due to the fact that they did not include CM phase in the MDCT protocol in their study, including only UN, NP, and EX phases. In our study, we used this proposed formula using a four-phase MDCT protocol to calculate wash-out values. When we used 2D ROIs we did not observe significant differences between ccRCC and the other renal masses, but when we used 3D ROIs, we found that the measurements were only significant between ccRCCs and oncocytomas (43.34 vs. 64.10, $p < 0.001$).

Another paper [24] proposed an enhancement correcting method in order to differentiate the renal carcinomas on MDCT. They used a formula created to obtain attenuation values that are corrected to a certain standard in the aorta at the level of the organ-supplying vessel. The results of this paper proved that the differentiation of ccRCC from pRCC, using the corrected attenuation in the CM and NP phase, was accurate (95.7% and 94.8%, respectively), with a cutoff value of 100 HU in the CM phase and 85 HU in the NP phase. In our opinion, this method is useful when evaluating the measurements of ROIs on the most avidly enhancing portions of the tumor, but it is hard to reproduce when assessing the measurements of ROIs on the whole lesion enhancement.

The research of Zhang et al. [18], using a three-phase MDCT protocol, did not find a difference in enhancement between ccRCCs and oncocytomas. This is in contradiction with our results, we found differentiation between ccRCC and oncocytoma in the enhancement, de-enhancement, and wash-out values. Measurement of 3D tumor ROI de-enhancement NP to EX phase had the highest AUC of 0.827 (95% CI: 0.752–0.887) with 74.8 % sensitivity and 81.8 % specificity when using 32 HU as the cutoff value.

Regarding the relative enhancement parameter, the research of Ruppert-Kohlmayr et al. [24] demonstrated a significant difference between ccRCC and pRCC both in the CM phase and in the NP phase ($p < 0.05$). They reported that ccRCC had higher values than the cutoff value in CM (of 2.0) and NP phase (of 1.8), whereas pRCC had lower values than the cutoff value in the CM and NP phase. Findings in this paper are partially supported by our study; we found a lower cutoff value in the CM ad NP phase of 0.21 and 0.24, respectively. This may be because of two key differences between our study and theirs. Firstly, Ruppert-Kohlmayr et al. used a three-phase MDCT protocol (UN, CM, and NP phase), whereas we used a four-phase MDCT protocol (UN, CM, NP, and EX phase). Secondly, Ruppert-Kohlmayr et al. used another formula for calculating the relative enhancement of the lesions than the one we used. They defined the relative enhancement ratio as the ratio between the corrected attenuation in a contrast phase and the measured attenuation in an unenhanced phase. In addition, we used a formula proposed by Coy et al. [15]: (HU tumor enhancement in the postcontrast phase—HU tumor in the unenhanced phase)/(cortex enhancement in the postcontrast phase—cortex in the unenhanced phase).

The present study has some limitations. The major one was the relatively small number of lesion subtypes. Further studies would be needed to demonstrate these promising results. Secondly, due to its retrospective nature, it could have a selection bias. Thirdly, the results depended on where the ROIs are drawn and, therefore, a standardized method of ROI measurement should be developed. Assessment of whole lesion attenuation values of renal lesions is technically more challenging than 2D ROI-based assessment of renal tumors, and may not be feasible in all clinical practice. Moreover, it is also not yet clear whether the assessment of the whole lesion is more accurate than 2D ROI-based assessment. Therefore, further studies are needed to compare the assessment of the whole lesion and the ROI assessment of renal cell carcinoma, both for accuracy and ease of use. Another limitation is that the four-phase MDCT renal mass protocol results in a high patient radiation dose and should be reserved only for cases in which lesion discrimination is required before treatment selection. Moreover, many of the renal tumors resected at our institution (approximately 400 lesions) did not have preoperative multiphasic MDCT scans available for review and were not included in our analysis. Even with these potential limitations, the results of our analyses suggest that there may be a consistent relationship between enhancement at MDCT and renal tumor histologic findings. However, these results should be validated in a large cohort, preferably in a prospective manner.

5. Conclusions

Based on our findings, we believe that quantitative MDCT enhancement patterns can help distinguish ccRCC from malignant RCC subtypes and benign oncocytoma. Given our findings, quantitative MDCT enhancement patterns may be a preliminary step in the development of a multiparametric decision model that can serve as an adjunct in clinical decision making for proper management.

Author Contributions: Conceptualization, C.-G.M., A.L., A.T.-S., and M.M.B.; methodology, A.L., A.T.-S., N.C., P.M., and M.S.; software, C.-G.M. and A.L.; formal analysis, B.P.; investigation, C.-G.M. and A.T.-S.; resources, C.-G.M. and P.M.; data curation, C.-G.M. and B.P.; writing—original draft preparation, C.-G.M.; writing—review and editing, A.L., A.T.-S., N.C., M.S., B.P., and M.M.B.; visualization, C.-G.M.; supervision, M.M.B.; project administration, M.M.B. All authors have read and agreed to the published version of the manuscript.

Funding: This research received no external funding.

Conflicts of Interest: The authors declare no conflict of interest.

References

1. Chow, W.-H.; Dong, L.M.; Devesa, S.S. Epidemiology and risk factors for kidney cancer. *Nat. Rev. Urol.* **2010**, *7*, 245–257. [CrossRef]
2. Moch, H.; Cubilla, A.L.; Humphrey, P.A.; Reuter, V.E.; Ulbright, T.M. The 2016 WHO Classification of Tumours of the Urinary System and Male Genital Organs—Part A: Renal, Penile, and Testicular Tumours. *Eur. Urol.* **2016**, *70*, 93–105. [CrossRef] [PubMed]
3. Inamura, K. Renal Cell Tumors: Understanding Their Molecular Pathological Epidemiology and the 2016 WHO Classification. *Int. J. Mol. Sci.* **2017**, *18*, 2195. [CrossRef] [PubMed]
4. Finelli, A.; Ismaila, N.; Bro, B.; Durack, J.; Eggener, S.; Evans, A.; Gill, I.; Graham, D.; Huang, W.; Jewett, M.A.; et al. Management of Small Renal Masses: American Society of Clinical Oncology Clinical Practice Guideline. *J. Clin. Oncol.* **2017**, *35*, 668–680. [CrossRef]
5. Brookman-May, S.D.; Johannsen, M.; May, M.; Hoschke, B.; Gunschera, J.; Wieland, W.F.; Burger, M. Difference between Clinical and Pathologic Renal Tumor Size, Correlation with Survival, and Implications for Patient Counseling Regarding Nephron-Sparing Surgery. *Am. J. Roentgenol.* **2011**, *197*, 1137–1145. [CrossRef] [PubMed]
6. Davenport, M.S.; Caoili, E.M. Role of Percutaneous Needle Biopsy for Renal Masses. *Semin. Interv. Radiol.* **2014**, *31*, 20–26. [CrossRef] [PubMed]
7. Lane, B.R.; Babineau, D.; Kattan, M.W.; Novick, A.C.; Gill, I.S.; Zhou, M.; Weight, C.J.; Campbell, S.C. A Preoperative Prognostic Nomogram for Solid Enhancing Renal Tumors 7 cm or Less Amenable to Partial Nephrectomy. *J. Urol.* **2007**, *178*, 429–434. [CrossRef]
8. Campbell, S.; Uzzo, R.G.; Allaf, M.E.; Bass, E.B.; Cadeddu, J.A.; Chang, A.; Clark, P.E.; Davis, B.J.; Derweesh, I.H.; Giambarresi, L.; et al. Renal Mass and Localized Renal Cancer: AUA Guideline. *J. Urol.* **2017**, *198*, 520–529. [CrossRef]
9. Motzer, R.J.; Jonasch, E.; Agarwal, N.; Bhayani, S.; Bro, W.P.; Chang, S.S.; Choueiri, T.K.; Costello, B.A.; Derweesh, I.H.; Fishman, M.; et al. Kidney Cancer, Version 2.2017, NCCN Clinical Practice Guidelines in Oncology. *J. Natl. Compr. Cancer Netw.* **2017**, *15*, 804–834. [CrossRef]
10. Kopp, R.P.; Aganovic, L.; Palazzi, K.L.; Cassidy, F.H.; Sakamoto, K.; Derweesh, I.H. Differentiation of clear from non-clear cell renal cell carcinoma using CT washout formula. *Can. J. Urol.* **2013**, *20*, 6790–6797.
11. Herts, B.R.; Coll, D.M.; Novick, A.C.; Obuchowski, N.; Linnell, G.; Wirth, S.L.; Baker, M.E. Enhancement Characteristics of Papillary Renal Neoplasms Revealed on Triphasic Helical CT of the Kidneys. *Am. J. Roentgenol.* **2002**, *178*, 367–372. [CrossRef] [PubMed]
12. De Leon, A.D.; Davenport, M.S.; Silverman, S.G.; Schieda, N.; Cadeddu, J.A.; Pedrosa, I. Role of Virtual Biopsy in the Management of Renal Masses. *Am. J. Roentgenol.* **2019**, *212*, 1–10. [CrossRef] [PubMed]
13. Sanchez, A.; Feldman, A.S.; Hakimi, A.A. Current Management of Small Renal Masses, Including Patient Selection, Renal Tumor Biopsy, Active Surveillance, and Thermal Ablation. *J. Clin. Oncol.* **2018**, *36*, 3591–3600. [CrossRef]
14. Sheir, K.Z.; El-Azab, M.; Mosbah, A.; El-Baz, M.; Shaaban, A.A. Differentiation of Renal Cell Carcinoma Subtypes by Multislice Computerized Tomography. *J. Urol.* **2005**, *174*, 451–455. [CrossRef]
15. Coy, H.; Young, J.R.; Douek, M.L.; Pantuck, A.; Brown, M.S.; Sayre, J.; Raman, S.S. Association of qualitative and quantitative imaging features on multiphasic multidetector CT with tumor grade in clear cell renal cell carcinoma. *Abdom. Radiol.* **2018**, *44*, 180–189. [CrossRef]
16. Huhdanpaa, H.T.; Hwang, D.; Cen, S.; Quinn, B.; Nayyar, M.; Zhang, X.; Chen, F.; Desai, B.; Liang, G.; Gill, I.; et al. CT prediction of the Fuhrman grade of clear cell renal cell carcinoma (RCC): Towards the development of computer-assisted diagnostic method. *Abdom. Imaging* **2015**, *40*, 3168–3174. [CrossRef] [PubMed]
17. Bird, V.G.; Kanagarajah, P.; Morillo, G.; Caruso, D.J.; Ayyathurai, R.; Leveillee, R.; Jorda, M. Differentiation of oncocytoma and renal cell carcinoma in small renal masses (<4 cm): The role of 4-phase computerized tomography. *World J. Urol.* **2011**, *29*, 787–792. [CrossRef] [PubMed]
18. Zhang, J.; Lefkowitz, R.A.; Ishill, N.M.; Wang, L.; Moskowitz, C.S.; Russo, P.; Eisenberg, H.; Hricak, H. Solid Renal Cortical Tumors: Differentiation with CT. *Radiology* **2007**, *244*, 494–504. [CrossRef] [PubMed]

19. Young, J.R.; Margolis, D.; Sauk, S.; Pantuck, A.J.; Sayre, J.; Raman, S. Clear Cell Renal Cell Carcinoma: Discrimination from Other Renal Cell Carcinoma Subtypes and Oncocytoma at Multiphasic Multidetector CT. *Radiology* **2013**, *267*, 444–453. [CrossRef]
20. Coy, H.; Young, J.R.; Douek, M.L.; Brown, M.S.; Sayre, J.; Raman, S.S. Quantitative computer-aided diagnostic algorithm for automated detection of peak lesion attenuation in differentiating clear cell from papillary and chromophobe renal cell carcinoma, oncocytoma, and fat-poor angiomyolipoma on multiphasic multidetector computed tomography. *Abdom. Radiol.* **2017**, *42*, 1919–1928. [CrossRef]
21. Lee-Felker, S.; Felker, E.R.; Tan, N.; Margolis, D.; Young, J.R.; Sayre, J.; Raman, S. Qualitative and Quantitative MDCT Features for Differentiating Clear Cell Renal Cell Carcinoma from Other Solid Renal Cortical Masses. *Am. J. Roentgenol.* **2014**, *203*, 516–524. [CrossRef]
22. Kim, S.H.; Kim, C.S.; Kim, M.J.; Cho, J.Y.; Cho, S.H. Differentiation of Clear Cell Renal Cell Carcinoma from Other Subtypes and Fat-Poor Angiomyolipoma by Use of Quantitative Enhancement Measurement during Three-Phase MDCT. *Am. J. Roentgenol.* **2016**, *206*, 21–28. [CrossRef]
23. Kim, J.K.; Kim, T.K.; Ahn, H.J.; Kim, C.S.; Kim, K.-R.; Cho, K.-S. Differentiation of Subtypes of Renal Cell Carcinoma on Helical CT Scans. *Am. J. Roentgenol.* **2002**, *178*, 1499–1506. [CrossRef] [PubMed]
24. Ruppert-Kohlmayr, A.J.; Uggowitzer, M.; Meissnitzer, T.; Ruppert, G. Differentiation of Renal Clear Cell Carcinoma and Renal Papillary Carcinoma Using Quantitative CT Enhancement Parameters. *Am. J. Roentgenol.* **2004**, *183*, 1387–1391. [CrossRef] [PubMed]
25. Pierorazio, P.M.; Hyams, E.S.; Tsai, S.; Feng, Z.; Trock, B.J.; Mullins, J.K.; Johnson, P.T.; Fishman, E.K.; Allaf, M.E. Multiphasic Enhancement Patterns of Small Renal Masses (≤4 cm) on Preoperative Computed Tomography: Utility for Distinguishing Subtypes of Renal Cell Carcinoma, Angiomyolipoma, and Oncocytoma. *Urology* **2013**, *81*, 1265–1272. [CrossRef]
26. Yuan, Q.; Kapur, P.; Zhang, Y.; Xi, Y.; Carvo, I.; Signoretti, S.; Dimitrov, I.E.; Cadeddu, J.A.; Margulis, V.; Brugarolas, J.; et al. Intratumor Heterogeneity of Perfusion and Diffusion in Clear-Cell Renal Cell Carcinoma: Correlation with Tumor Cellularity. *Clin. Genitourin. Cancer* **2016**, *14*, e585–e594. [CrossRef]
27. Shebel, H.M.; Elsayes, K.M.; Sheir, K.Z.; El Atta, H.M.A.; El-Sherbiny, A.F.; Ellis, J.H.; El-Diasty, T.A. Quantitative Enhancement Washout Analysis of Solid Cortical Renal Masses Using Multidetector Computed Tomography. *J. Comput. Assist. Tomogr.* **2011**, *35*, 337–342. [CrossRef]
28. Bindayi, A.; McDonald, M.L.; Beksac, A.T.; Rivera-Sanfeliz, G.; Shabaik, A.; Hughes, F.; Aganovic, L.; Hansel, D.E.; Derweesh, I.H. Can multiphase CT scan distinguish between papillary renal cell carcinoma type 1 and type 2? *Türk Ürol. Derg./Turk. J. Urol.* **2018**, *44*, 316–322. [CrossRef]
29. Jinzaki, M.; Tanimoto, A.; Mukai, M.; Ikeda, E.; Kobayashi, S.; Yuasa, Y.; Narimatsu, Y.; Murai, M. Double-Phase Helical CT of Small Renal Parenchymal Neoplasms: Correlation with Pathologic Findings and Tumor Angiogenesis. *J. Comput. Assist. Tomogr.* **2000**, *24*, 835–842. [CrossRef]
30. Chen, F.K.; Huhdanpaa, H.; Desai, B.; Hwang, D.; Cen, S.Y.; Sherrod, A.; Bernhard, J.-C.; Desai, M.M.; Gill, I.; Duddalwar, V.A. Whole lesion quantitative CT evaluation of renal cell carcinoma: differentiation of clear cell from papillary renal cell carcinoma. *SpringerPlus* **2015**, *4*, 66. [CrossRef]

Original Article

Acta Radiologica
0(0) 1–8

DOI: 10.1177/02841851211010397
journals.sagepub.com/home/acr
SAGE

Magnetic resonance imaging characteristics of chronic prostatitis in patients under the age of 50: is it more than the eye can see?

Andrei Lebovici[1,2,3], Csaba Csutak[1,3], Paula Popa[1], Nicolae Crișan[4,5], Mihai Suciu[4,6], Bogdan Feciche[7], Iulia Andraș[4,5], Paul-Andrei Ștefan[1,8] and Diana Sorina Feier[1,2,3]

Abstract

Background: The magnetic resonance (MRI) diagnosis of chronic prostatitis (CP) is insufficiently evaluated.

Purpose: To evaluate the MRI appearance of CP in young patients by comparing it to individuals with non-prostatic related pathology.

Material and Methods: The study included 47 patients with prostatitis-like symptoms evaluated by urologists and referred to pelvic MRI examination (mean age=40.23±7 years; age range=23–49 years) and 93 age-matched individuals with non-prostatic related pathology (mean age=37.5±7 years; age range=21–49 years). All MRI examinations were performed on a 1.5-T machine using a prostate-specific protocol for the prostatitis group and different protocols that included high-resolution small field of view T2-weighted (T2WI) and diffusion-weighted imaging (DWI), for the control group, depending on the clinical indication.

Results: Four different T2WI intensity patterns were observed: hyperintense homogenous; slightly to moderate homogenous hypointense; inhomogeneous; and marked hypointense. We found statistically significant differences between the two analyzed groups regarding mean ADC values ($P<0.001$), distribution of T2WI intensity patterns ($P<0.0001$), and the presence of dilated venous plexus ($P=0.0007$). No differences were found regarding prostate volume ($P=0.15$). In multivariate analysis, all four analyzed imaging parameters were independent predictors of chronic prostatitis ($R^2=0.67$; $P<0.0001$). Considered together, an age >28 years, an inhomogeneous or marked hypointense T2WI intensity pattern (types 3 and 4), an ADC value ≤1250, and the presence of dilated venous plexus are able to predict CP with an AUC of 93% (sensitivity=85.1%, specificity=88.4%).

Conclusion: MR parameters like T2WI intensity patterns, ADC values, and venous plexus appearance are promising non-invasive tools in the challenging environment of CP diagnosis.

Keywords

Prostatitis, prostate, magnetic resonance imaging, T2-weighted imaging, apparent diffusion coefficient

Date received: 29 October 2020; accepted: 19 March 2021

---

[1] Radiology, Surgical Specialties Department, “Iuliu Hatieganu” University of Medicine and Pharmacy, Cluj-Napoca, Romania
[2] Affidea Imaging Center, Cluj-Napoca, Romania
[3] Radiology and Imaging Department, County Emergency Hospital, Cluj-Napoca, Romania
[4] Department of Urology, “Iuliu Hatieganu” University of Medicine and Pharmacy, Cluj-Napoca, Romania
[5] Department of Urology, Clinical Municipal Hospital Cluj-Napoca, Cluj-Napoca, Romania
[6] Institute of Urology and Renal Transplant, Cluj-Napoca, Romania
[7] Department of Urology, Satu-Mare County Emergency Hospital, Satu-Mare, Romania
[8] Anatomy and Embryology, Morphological Sciences Department, “Iuliu Hatieganu” University of Medicine and Pharmacy, Cluj-Napoca, Romania

Corresponding author:
Csaba Csutak, Iuliu Haţieganu University of Medicine and Pharmacy, 3-5 Clinicilor street, Cluj-Napoca, 400006, Romania.
Email: csutakcsaba@yahoo.com

Introduction

Prostatitis is considered to be an enigmatic disease due to the inconsistency of the epidemiological data, the inadequacy of the diagnosis, and the absence of a standardized pharmacological treatment (1).

According to the United States National Institute of Health (NIH), prostatitis is classified in four categories using the Chronic Prostatitis Syndrome Index (NIH-CPSI): acute bacterial prostatitis (NIH-CPSI I); chronic bacterial prostatitis (NIH-CPSI II); chronic non-bacterial prostatitis (CP)/chronic pelvic pain syndrome (CPPS) with or without inflammatory cells present (NIH-CPSI III A and B); and asymptomatic prostatitis (NIH-CPSI IV) (2).

By definition, CP is a pathological condition characterized by urologic and anorectal pain or discomfort in the pelvic region, associated with urinary symptoms and/or sexual dysfunction, in the absence of infection, malignancy, or structural abnormality, lasting for at least three of the previous six months (3).

Epidemiological data report prostatitis to be the most common urologic disease in men aged younger than 50 years (4). Symptomatic CP accounts for up to 95% of all prostatitis cases with an estimated prevalence of 15% in men aged 35–45 years (3,5).

The use of ultrasound (US), computed tomography (CT), and magnetic resonance imaging (MRI) does not have an established role in the conventional workup of CP (3). The imaging is useful in ruling out other pathological conditions which may be mistaken for CP (6,7).

The main use of multiparametric MRI (mpMRI) in prostate-related pathologies is the detection and staging of prostate cancer (PC) (8).

When comparing whole-mount radical prostatectomy specimens with the corresponding mpMRI images, pure normal prostate glands are iso-intense on T2-weighted (T2W) imaging and the high signal intensity (SI) areas represent cystic atrophy or large-gland variant of simple atrophy (9). Inflammation, adenosis, post-atrophic hyperplasia, and high-grade prostatic intra-epithelial neoplasia may mimic well differentiated PC on mpMRI because they all show indistinct low SI onT2W imaging and moderate contrast enhancement on dynamic contrast-enhanced MRI (DCE) (10,11). On diffusion-weighted imaging (DWI), there is a considerable overlapping imaging characteristic between inflammation and well-differentiated PC (12).

The aim of the present study was to evaluate the intensity patterns on T2W images and apparent diffusion coefficient (ADC)/DWI signal intensity measurements of intra- and extra-prostatic changes in patients with symptomatic CP aged younger than 50 years and compare them with the appearance of the prostate and adjacent tissues in patients with non-prostatic related pathology from the same age category.

Material and Methods

Participants

This retrospective single–center study complied with the Health Insurance Portability and Accountability Act (HIPAA) and was approved by our institutional review board, with a waiver of informed consent.

The study included 193 male participants who underwent pelvic MRI examinations between October 2018 and December 2019.

Prostatitis group

The individuals were extracted from our hospital information system. The inclusion criteria were as follows: patients with symptomatic CP (NIH-CPSI category III) evaluated by urologists and referred for pelvic MRI examination in our institution; aged 20–49 years; and examined with standard dedicated prostate MRI protocol. After analyzing our database, 70 patients met these criteria. From this list we excluded patients with granulomatous prostatitis ($n = 2$), clinical and biochemical concomitant suspicion of prostate cancer ($n = 10$), prior prostate biopsy ($n = 3$), congenital abnormalities ($n = 3$), and important artifacts such as susceptibility and motion artifacts ($n = 8$). The final study population group consisted of 47 patients (mean age $= 40.23 \pm 7$ years; age range $=$ 23–49 years).

Control group

The control group consisted of patients in the same age interval that underwent a pelvic MRI in our institution in the same period of time, for non-prostatic related pathology. Initially 123 patients met these criteria. From this list we excluded patients who underwent neoadjuvant pelvic radiotherapy ($n = 14$), locally treated for bladder cancer ($n = 2$), and with important artifacts such as susceptibility and motion artifacts ($n = 14$). The final study population group consisted of 93 patients (mean age $= 37.5 \pm 7$ years; age range $=$ 21–49 years). MRI indications for these group were as followed: anorectal disorders (perianal fistula, $n = 36$; rectal/sigmoid cancer, $n = 17$; ulcerative rectocolitis, $n = 5$; appendicitis, $n = 1$), urinary bladder tumors at diagnosis ($n = 5$), musculoskeletal disorders ($n = 15$), testicular pathology (tumors, $n = 5$; cryptorchidism, $n = 5$), penile pathology (Peyronie disease, $n = 3$; trauma, $n = 1$), and other conditions (inguinal lymphadenopathy, $n = 2$).

MRI protocol

All MRI examinations were performed using a 1.5-T machine (Magnetom Symphony TIM system; Siemens AG, Erlangen, Germany) using an eight-channel phased-array body coil.

A prostate-specific protocol was used for the prostatitis group. Before the examination no bowel preparation or enema was performed. No antispasmodic agent was administrated. The acquisition protocol included: turbo spin echo (TSE) T2W imaging in the sagittal, coronal, and axial planes; axial DWI with three b-values of 50 s/mm^2, 400 s/mm^2, and 1000 s/mm^2; and axial plane DCE with fat saturated three-dimensional (3D) T1 spoiled gradient recalled (SPGR) sequence with a temporal resolution of 10 s and an intravenous contrast agent flow of 2.5 mL/s (Clariscan® 0.5 mmol/mL, GE Healthcare, Nycomed, Norway). All axial acquisitions were performed perpendicular to the long axis of the prostate while the coronal T2W imaging sequence was acquired parallel to the long axis of the prostate. In addition, an angulated transversal T1-weighted (T1W) acquisition TSE sequence was performed to cover the entire pelvis. The acquisition parameters are detailed in Table 1.

For the control group, different protocols were used depending on the clinical indication, 63 of the patients benefited from high-resolution, small field of view T2W imaging of the prostate region (urinary bladder and rectal protocols) while 69 of examinations included DWI with the same b-values but with different inclination.

Image analysis

Image interpretation was performed on a picture archiving and communication system (PACS) station (KODAK/Carestream Version 10.2; Carestream Health) by two radiologists in consensus, with 10 and 12 years of experience in pelvic imaging (LA and CC, each with at least 10 years of experience in pelvic MRI). The readers were unaware of the medical data and final diagnosis.

The prostate volume was determined for each patient by using the prolate ellipsoid formula (height × width × length × $\pi/6$).

The signal characteristics of the peripheral zone (PZ) on axial T2W imaging were divided into four patterns (the same for both prostatitis group and the control group), as follows (Fig. 1):

Type 1: Homogenous hyperintense.

Type 2: Homogenous slightly to moderate hypointense. The intensity of the PZ was compared to the central gland intensity, slightly/moderate was considered when the transition zone (TZ) had lower SI compared to the PZ.

Type 3: Inhomogeneous. In this category we included the alternating low signal with high signal PZ and the focal low signal non-contoured deforming lesion.

Type 4: Homogenous marked hypointense. In this category the low intensity of the PZ was equal to the TZ low signal areas.

Periprostatic venous plexus were analyzed on the same axial T2W imaging and the presence of vascular conglomerates with vessel caliber greater than 4 mm were considered as dilatation (Fig. 2).

ADC maps were generated from the DWI sequences, and regions of interest (ROIs) were placed in the most hypointense areas of the prostate. ROIs were drawn to occupy approximately 75% of the area to be sure that TZ, periprostatic tissue, and prostate margins would not be included (Fig. 3). The mean SI was measured automatically by the PACS system.

All MRI parameters are summarized in Table 2.

Statistical analysis

Continuous variables were summarized with means and ranges (age [years]) or medians and ranges (ADC values, prostate volume [mL], PSA [ng/mL] values, when available); categorical variables were described with frequencies and percentages (signal intensity patterns, dilated venous plexus). Box plots were provided for ADC values. Relationships between imaging characteristics and CP were assessed with the Wilcoxon rank-sum test for continuous variables and Fisher's exact test for categorical variables. Differences between groups were evaluated using one-way analysis of variance (ANOVA) for continuous variables. Through multiple regression analysis, independent predictors for the presence of CP were identified, and the coefficient of determination (R^2) was computed. The diagnostic value of these predictors was evaluated using the receiver operating characteristic curve (ROC) analysis. Optimal cutoff values were chosen using a common

Table 1. Acquisition protocol and sequence parameters for the prostatitis group.

	Sequence	Slices (n)	ST (mm)	TR (ms)	TE (ms)	Averages	Matrix	Voxel size (mm)
T1W imaging axial	TSE	40	5.0	740	12	1	240 × 320	0.8 × 0.8 × 5
T2W imaging sagittal	TSE	25	3.5	4050	92	3	320 × 320	0.5 × 0.5 × 3.5
T2W imaging axial	TSE	22	3	7000	82	6	320 × 320	0.5 × 0.5 × 3
T2W imaging coronal	TSE	18	3	5840	92	6	320 × 320	0.5 × 0.5 × 3
DWI	2D-EPI	40	3	4700	89	8	128 × 128	2 × 2 × 3
T1W imaging DCE-MRI	FS SPGR	24	3	4.87	1.67	1	137 × 224	2 × 1.4 × 3

DCE-MRI, dynamic contrast-enhanced magnetic resonance imaging; EPI, echo planar imaging; FOV, field of view; FS, fat saturation; SPGR, spoiled gradient recalled; ST, slice thickness; T1W/T2W, T1/T2-weighted; TE, time of echo; TR, time of repetition; TSE, turbo spin echo.

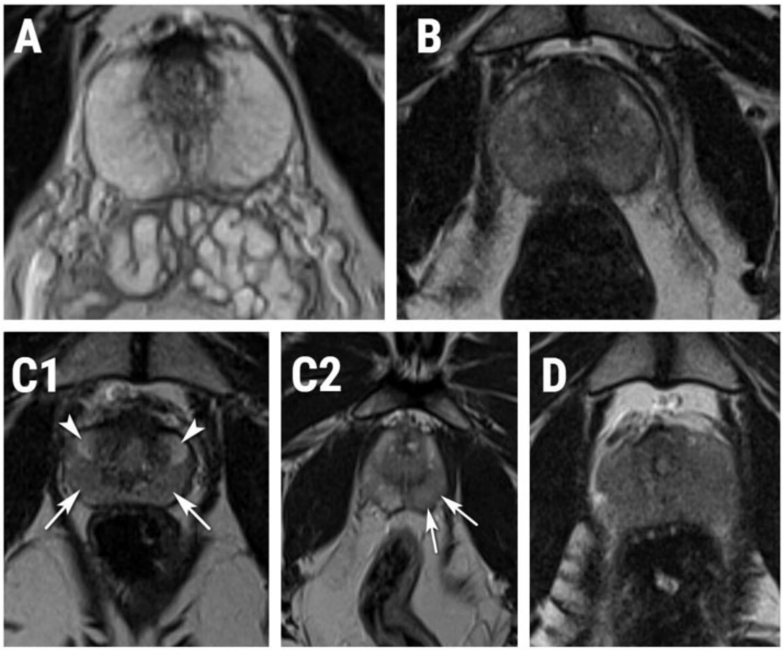

Fig. 1. T2W imaging axial views of different intensity patterns of the peripheral zone of the prostate. (a) A 45-year-old patient with non-prostatic pathology shows homogenous hyperintense peripheral zone (type 1 T2W imaging signal pattern). (b) A 46-year-old patient with non-prostatic pathology shows moderate homogenous hypointense peripheral zone. Compared with the TZ, the intensity of the PZ is slightly higher (type 2 T2W imaging signal pattern). (c) 1: A 41-year-old patient with CP shows inhomogeneous hyperintense PZ with alternating hyperintense (arrow heads) and hypointense (white arrows) regions (type 3 T2W imaging signal pattern). 2: A 47-year-old man with PSA level of 3.7 ng/mL shows focal hypointense non-contour deforming lesion (white arrows) in the PZ on the left side (type 3 T2W imaging signal pattern). This patient underwent prostate biopsy that revealed only focal prostatitis changes, the PSA levels dropped below 1 ng/mL after six months. No control MRI was performed. (d) A 26-year-old patient with prostatitis-like syndrome shows a marked homogenous hypointense PZ with almost no differentiation between the signal intensity of the PZ and the TZ (type 4 T2W imaging signal pattern). CP, chronic prostatitis; MRI, magnetic resonance imaging; PZ, peripheral zone; T2W, T2-weighted; TZ, transition zone.

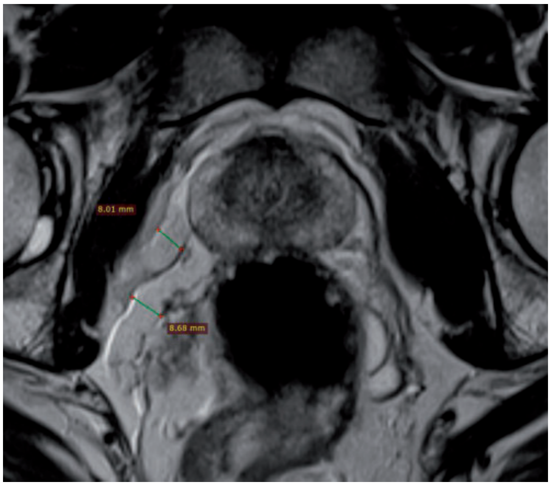

Fig. 2. T2W imaging axial view of the prostate in a 40-year-old patient with chronic prostatitis shows markedly enlarged venous plexuses with caliber up to 8.7 mm. The peripheral zone demonstrates a type 3 signal pattern.

optimization step that maximized the Youden index for predicting patients with CP, and sensitivity and specificity were computed from the same data, without further adjustments. The statistical analysis was performed using commercially available software, MedCalc, for Windows, version 9.3.2.0 (MedCalc Software) and SPSS for Mac, version 20.0 (SPSS Inc.).

Results

General characteristics of patients

A total of 140 participants (mean age = 38.40±7.69 years; age range = 21–49 years) were included in this study. The participants were divided in two groups: the prostatitis group included 47 patients (mean age = 40.23 ± 7.01 years; age range = 23–49 years) and the non-prostatic related pathology group included 93 patients (mean age = 37.48 ± 7.89 years; age range = 21–49 years).

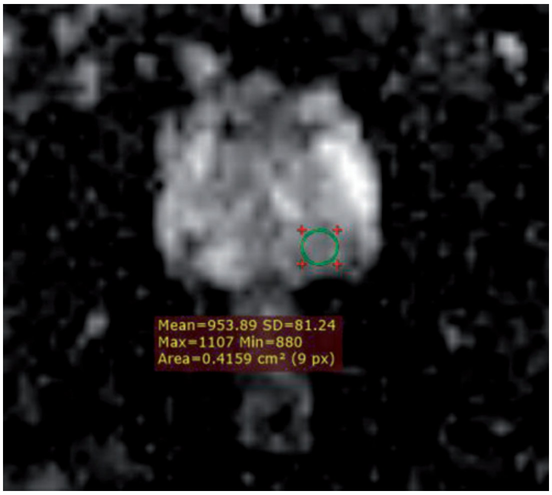

Fig. 3. ADC map in a 39-year-old patient with chronic prostatitis shows restricted diffusion in the peripheral zone on the left side with mean ADC value of 0.953 $\times 10^{-3}$mm^2/s. The PSA levels of this patient were <1 ng/mL during one-year follow-up. The control MRI performed after 14 months showed the stable aspect of the prostate. No biopsy was performed. ADC, apparent diffusion coefficient; MRI, magnetic resonance imaging; PSA, prostate-specific antigen.

Table 2. MRI imaging parameters investigated.

Imaging parameter	Method of quantification
Prostate volume	Height × width × length × π /6
PZ – T2W imaging	Type 1: Homogenous hyperintense Type 2: Homogenous slightly to moderate hypointense Type 3: Inhomogeneous Type 4: Homogenous marked hypointense
ADC values	ROI occupying 75% of the PZ
Periprostatic venous plexus	> 4 mm

ADC, apparent diffusion coefficient; MRI, magnetic resonance imaging; PZ, peripheral zone; ROI, region of interest; T2W, T2-weighted.

PSA measurements were available in 22 patients from the prostatitis group with a median value of 2.8 ng/mL (range = 0.5–8 ng/mL). The median prostate volume for the prostatitis group was 21.11 mL (range = 11.4–48.2 mL) while for the control group the median prostate volume was smaller, at 17.47 mL (range = 7.3–34.5 mL). The difference between the two groups was not statistically significant ($P = 0.063$).

Imaging parameters

Regarding the T2W imaging intensity pattern, the most common for the prostatitis group was type 3, seen in 26 of 47 patients (55.3%), followed by pattern types 2 and 4, observed in 11 (23.4%) and 10 (21.2%) patients, respectively, while type 1 was not observed in any patient. For the non-prostatic related pathology group, the most common pattern was type 2, seen in 54 of 93 patients (58.06%), followed by types 1 and 3, observed in 19 (20.4%) and 12 (12.9%) patients, respectively, while type 4 was identified in 8 (8.6%) patients (Table 3).

Table 3. Result distribution of T2W imaging patterns.

T2W imaging pattern	Prostatitis group	NPRP group
Type 1	-	19/93 (20.4)
Type 2	11/47 (23.4)	54/93 (58.06)
Type 3	26/47 (55.3)	12/93 (12.9)
Type 4	10/47 (21.2)	8/93 (8.6)

Values are given as n (%).
NPRP, non-prostate-related pathology; T2W, T2-weighted.

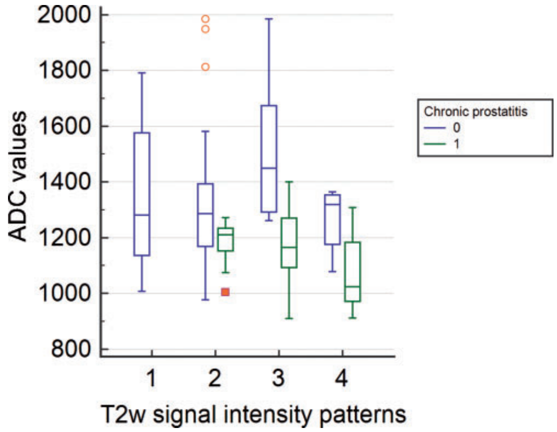

Fig. 4. Apparent diffusion coefficient values in patients with chronic prostatitis and non-prostatic related pathology, according to their T2-weighted imaging signal intensity patterns.

Mean prostatic ADC values for the prostatitis group and the non-prostatic-related pathology group were significantly different ($P < 0.001$). The mean ADC value for the prostatitis group was $1.153 \pm 0.125 \times 10^{-3}$mm^2/s while the mean ADC value for the non-prostatic related pathology group was $1.350 \pm 0.236 \times 10^{-3}$mm^2/s, significantly higher. Six patients from the prostatitis group had ADC values of $< 1.000 \times 10^{-3}$mm^2/s, mimicking prostate cancer. Distribution of the ADC measurements according to the T2W imaging intensity patterns in both groups are illustrated in Fig. 4 and Table 4.

Periprostatic venous plexus dilatation was observed in 27 patients (57.4%) from the prostatitis group, while in the non-prostatic related pathology group, 26 (27.95%) had dilated periprostatic venous plexus, with a statistically difference between the groups ($P = 0.001$).

Data analysis

In the univariate analysis, we found statistically significant differences between the two analyzed groups

Table 4. The ADC values ($\times 10^{-3}$mm^2/s) for each signal type pattern.

	T2W type 1	T2W type 2	T2W type 3	T2W type 4
ADC NPRP	1.281 ± 0.256	1.286 ± 0.228	1.449 ± 0.237	1.320 ± 0.120
ADC CP		1.211 ± 0.081	1.165 ± 0.123	1.024 ± 0.131

Values are given as mean ± SD.
ADC, apparent diffusion coefficient; CP, chronic prostatitis; NPRP, non-prostate-related pathology; T2W, T2-weighted.

Table 5. Multivariate analysis of factors independently associated with the presence of chronic prostatitis.

Independent variables	Odds ratio	Coefficient	Standard error	Wald	*P* value
Age (years)	1.16	0.15020	0.052615	8.1493	0.043
ADC	0.99	–0.0089628	0.0024321	13.5808	0.0002
T2W SI patterns	8.08	2.09038	0.47807	19.1190	<0.0001
Dilated venous plexus	6.94	1.93815	0.65492	8.7579	0.0031
Significance level	$P < 0.0001$				
Cox & Snell R^2	0.5058				
Nagelkerke R^2	0.6828				

ADC, apparent diffusion coefficient; SI, signal intensity; T2W, T2-weighted.

regarding patients' mean age, ADC median value ($P < 0.001$), distribution of T2W imaging intensity patterns ($P < 0.0001$), and the presence of dilated periprostatic venous plexus ($P = 0.0007$).

In multivariate analysis, according to logistic regression, all four analyzed imaging parameters were independent predictors of CP ($R^2 = 0.68$; $P < 0.0001$) (Table 5).

MRI diagnostic performance

Analyzed in an independent manner, in our group of patients the presence of T2W imaging SI patterns type 3 and 4 were able to predict CP with an area under the ROC curve (AUC) of 0.789 (sensitivity = 76.6%, specificity = 78.5%).

The presence of dilated periprostatic venous plexus alone were able to predict CP with an AUC of 0.647 (sensitivity = 57.4%, specificity = 72%).

For a cutoff level of $\leq 1.250 \times 10^{-3}$mm^2/s, the prostatitis group ADCs showed a sensitivity and specificity of 80.9% and 68.1%, respectively, while the AUC was 0.77.

Considered together, age > 28 years, an inhomogeneous or marked hypointense T2W imaging intensity pattern, an ADC value < 1.250 $\times 10^{-3}$mm^2/s, and the presence of periprostatic venous plexus are able to predict CP with an AUC of 93% (sensitivity =85.1%, specificity = 88.4%) (Fig. 5).

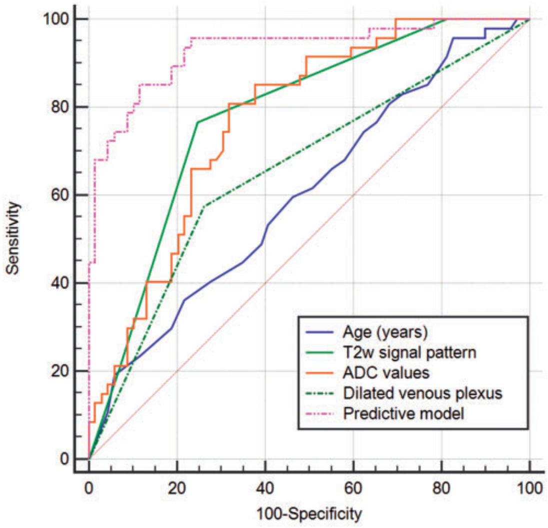

Fig. 5. Receiver operating characteristic curve for the multivariate in the assessment of chronic prostatitis.

Discussion

In our study, the PZ T2W imaging signal characteristics of the participants with non-prostatic-related pathology showed the classical aspect of homogenous hyperintensity in only 19 of 93 participants (20.4%) (13). The predominant signal pattern of the normal PZ on T2W imaging was actually a type 2 pattern, seen in more than half of the participants (54/93, 58.06%). These PZ T2W imaging intensity patterns can be explained by the physiological development of the prostate. Between the ages of 20 and 50 years, the glandular lumen volume increases. The increase in glandular volume is directly associated with the increase of the prostatic fluid content (14). De Visschere et al. (9) analyzed the characteristics of normal and benign prostate pathologies by comparing the MRI axial slices with whole-mount radical prostatectomy specimens. In their study, they observed that normal glandular tissue was isointense and not hyperintense. The T2W imaging hyperintensity was actually given by the much larger areas of simple atrophy and cystic atrophy present in these prostate specimens.

In the prostatitis group, the most common T2W imaging signal pattern was, as expected, type 3 (26 of 47 participants, 55.3%). In this group, we included the typical appearance of prostatitis with focal low signal lesion or alternating low and high signals (9,15). Type 1 pattern was not present in the prostatitis group, making it an important parameter in excluding CP.

The ADC measurements in our study showed statistically significant differences between the two groups ($P < 0.001$). The mean ADC value for the prostatitis group was lower compared to the control group. In 2008, Tamda et al. (15) measured the PZ ADC values of the normal prostate in different age groups; the mean ADC values for the age groups 20–39 and 40–59 were $1.37 \pm 0.18 \times 10^{-3}\text{mm}^2/\text{s}$ and $1.63 \pm 0.26 \times 10^{-3}\text{mm}^2/\text{s}$, respectively, similar to our findings (15). The ADC values for the prostatitis group correspond to a low to moderate grade of diffusion restriction, as expected and with concordance with the published data (15).

When comparing the ADC measurements of the type 3 pattern between groups, the non-prostatic related pathology group shows significantly higher ADC values. The result can be explained by the different origin of the hypointense tissue measured for the two groups: in the non-prostatic-related pathology group, the hypointense areas probably represent normal glandular tissue, while in the prostatitis group the hypointense areas represent prostatitis foci with higher grade of diffusion restriction.

An extra prostatic sign of PC is the enlargement of the periprostatic venous plexus (8). In our study, dilatation of the periprostatic venous plexus was observed in 27 patients (57.4%) from the prostatitis group while in the non-prostatic-related pathology group, a periprostatic venous plexus was seen in 26 patients (27.95%). These results contradict the limited available data. In a recent study by Clemente et al. (8) on a young population group (mean age = 41 years) with CPPS, the dilatation of the periprostatic venous plexus was observed in 70% of the patients with CPPS, more than in our study. Regarding the control group, Clemente et al. found a dilated periprostatic venous plexus in only 3 of 90 participants (3%). In both studies the same threshold of 4 mm was used. One explanation for the difference between the two studies regarding the control group is the fact that in the Clemente study the control group had musculoskeletal protocols (100%) while in our study, the majority of patients (n = 63, 67.7%) benefited from high-resolution T2W imaging of the prostate region.

When considering every parameter evaluated in this study individually, the MRI performance in the detection of CP changes is limited. There is a large overlap between normal and diseased prostate regarding T2W imaging intensity patterns, ADC analysis, and in the presence of dilated periprostatic venous plexus.

The diagnostic performance of MRI in the detection of PC changes dramatically when taking all relevant parameters into account. In the right clinical environment, an individual aged > 28 years, an inhomogeneous or marked hypointense T2W imaging intensity pattern, an ADC value $< 1.250 \times 10^{-3}\text{mm}^2/\text{s}$, and the presence of dilated periprostatic venous plexus were able to predict CP with an AUC of 93% (sensitivity = 85.1%, specificity = 88.4%). However, these results may be considered only in young patients with no suspicion of prostate cancer.

Although according to this study the diagnostic performance of T2W imaging and DWI in the detection of CP changes is very high, the clinical relevance is debatable. A true benefit of these findings would be the possibility to distinguish between focal CP and lesions suspicious of prostate cancer (PIRADS 3, 4, and 5 lesions). However, one of the shortcomings of a PI-RADS score of 4 is that lesions that moderately restrict diffusion but demonstrate focal enhancement could also be represented by inflammation. In addition, patients had PIRADS 4 lesions, with clear restriction of diffusion, making it impossible to differentiate these two entities in the absence of biopsy. Although patients lacked pathological evaluation, it would be fair to assume that prostate cancer is an extremely rare encounter in this age group. A useful sequence for further evaluation of diseased prostate is DCE, which can probably further boost the diagnostic performance of MRI by comparing the enhancing curves of normal and diseased prostates. Further studies are needed to characterize CP on MRI and by doing so trying to differentiate it from PIRADS 3, 4 and 5 lesions, for a final result of reducing unnecessary biopsies.

The present study has some limitations. First, the study population was relatively small. Second, because of the retrospective nature of this study, concomitant prostate pathology of the control group could not be excluded. Third, we do not have data on intra-observer and inter-observer variability. Fourth, absence of the comparison of the DCE sequence, momentary an essential sequence in the multiparametric analysis of the prostate, can also be regarded as a limitation. Fifth, the PSA values of the control group were not available. Sixth, the pathologies included in the control group were not histologically proven. Finally, the protocol did not include a b-value $> 1000\ \text{s/mm}^2$.

In conclusion, MR parameters such as T2W imaging intensity patters, ADC values, and venous plexus appearance are promising non-invasive tools in the challenging environment of the diagnosis of chronic prostatitis.

Authors' note

Paul-Andrei Ştefan is also affiliated with Radiology and Imaging Department, County Emergency Hospital, Cluj-Napoca, Romania.

Declaration of conflicting interests

The author(s) declared no potential conflicts of interest with respect to the research, authorship, and/or publication of this article.

Funding

The author(s) received no financial support for the research, authorship, and/or publication of this article.

ORCID iDs

Andrei Lebovici https://orcid.org/0000-0002-2815-2132
Csaba Csutak https://orcid.org/0000-0001-6669-6483
Paul-Andrei Ştefan https://orcid.org/0000-0001-5358-2137

References

1. Magri V, Boltri M, Cai T, et al. Multidisciplinary approach to prostatitis. Arch Ital Urol Androl 2019;90:227–248.
2. Nickel JC, Nyberg LM, Hennenfent M. Research guidelines for chronic prostatitis: consensus report from the first National Institutes of Health International Prostatitis Collaborative Network. Urology 1999;54:229–233.
3. Magistro G, Wagenlehner F. M, Grabe M, et al. Contemporary management of chronic prostatitis/chronic pelvic pain syndrome. Eur Urol 2016;69:286–297.
4. Collins MM, Stafford RS, O'Leary MP, et al. How common is prostatitis? A national survey of physician visits. J Urol 1998;159:1224–1228.
5. Nickel JC, Downey J, Hunter D, et al. Prevalence of prostatitis-like symptoms in a population based study using the National Institutes of Health chronic prostatitis symptom index. J Urol 2001;165:842–845.
6. Moore J. R, Pathak R. A, Snowden C, et al. Multispecialty retrospective review of the clinical utility of pelvic magnetic resonance imaging in the setting of pelvic pain. Transl Androl Urol 2017;6:1155–1158.
7. Sah VK, Wang L, Min X, et al. Multiparametric MR imaging in diagnosis of chronic prostatitis and its differentiation from prostate cancer. Radiology of Infectious Diseases 2015;1:70–77.
8. Turkbey B, Rosenkrantz AB, Haider MA, et al. Prostate Imaging Reporting and Data System Version 2.1: 2019 Update of Prostate Imaging Reporting and Data System Version 2. Eur Urol 2019;76:340–351.
9. DeVisschere PJ, Vral A, Perletti G, et al. Multiparametric magnetic resonance imaging characteristics of normal, benign and malignant conditions in the prostate. Eur Radiol 2017;27:2095–2109.
10. Hom JJ, Coakley FV, Simko JP, et al. High grade prostatic intraepithelial neoplasia in patients with prostate cancer: MR and MR spectroscopic imaging features–initial experience. Radiology 2007;242:483–489.
11. Sciarra A, Panebianco V, Ciccariello M, et al. Magnetic resonance spectroscopic imaging (1H-MRSI) and dynamic contrast-enhanced magnetic resonance (DCE-MRI): pattern changes from inflammation to prostate cancer. Cancer Invest 2010;28:424–432.
12. Nagel KN, Schouten MG, Hambrock T, et al. Differentiation of prostatitis and prostate cancer by using diffusion-weighted MR imaging and MR-guided biopsy at 3T. Radiology 2013;267:164–172.
13. Stabile A, Giganti F, Rosenkrantz A, et al. Multiparametric MRI for prostate cancer diagnosis: current status and future directions. Nat Rev Urol 2020;17:41–61.
14. Zaichick V, Zaichick S. Age-related histological and zinc content changes in adult non hyperplastic prostate glands. Age (Dordr) 2014;36:167–181.
15. Ren J, Huan Y, Wang H, et al. Diffusion-weighted imaging in normal prostate and differential diagnosis of prostate diseases. Abdom Imaging 2008;33:724–728.

Journal of
Personalized Medicine

Article

Preoperative Predicting the WHO/ISUP Nuclear Grade of Clear Cell Renal Cell Carcinoma by Computed Tomography-Based Radiomics Features

Claudia-Gabriela Moldovanu [1,2], Bianca Boca [1,2,*], Andrei Lebovici [2,3,*], Attila Tamas-Szora [4], Diana Sorina Feier [2,3], Nicolae Crisan [5], Iulia Andras [5] and Mircea Marian Buruian [1,6]

[1] Department of Radiology and Medical Imaging, Faculty of Medicine, George Emil Palade University of Medicine, Pharmacy, Science and Technology of Târgu Mureș, 540139 Târgu Mureș, Romania; moldovanu_claudia@yahoo.com (C.-G.M.); mircea.buruian@umfst.ro (M.M.B.)

[2] Department of Radiology, Emergency Clinical County Hospital of Cluj-Napoca, 400006 Cluj-Napoca, Romania; diana.feier@umfcluj.ro

[3] Department of Radiology, Faculty of Medicine, Iuliu Hațieganu University of Medicine and Pharmacy, 400012 Cluj-Napoca, Romania

[4] Department of Radiology, Clinical Municipal Hospital, 400139 Cluj-Napoca, Romania; attitamas@yahoo.com

[5] Department of Urology, Faculty of Medicine, Iuliu Hațieganu University of Medicine and Pharmacy, 400012 Cluj-Napoca, Romania; drnicolaecrisan@gmail.com (N.C.); dr.iuliaandras@gmail.com (I.A.)

[6] Department of Radiology, Emergency Clinical County Hospital Târgu Mureș, 540136 Târgu Mureș, Romania

* Correspondence: bianca.petresc@gmail.com (B.B.); andrei1079@yahoo.com (A.L.)

Abstract: Nuclear grade is important for treatment selection and prognosis in patients with clear cell renal cell carcinoma (ccRCC). This study aimed to determine the ability of preoperative four-phase multiphasic multidetector computed tomography (MDCT)-based radiomics features to predict the WHO/ISUP nuclear grade. In all 102 patients with histologically confirmed ccRCC, the training set ($n = 62$) and validation set ($n = 40$) were randomly assigned. In both datasets, patients were categorized according to the WHO/ISUP grading system into low-grade ccRCC (grades 1 and 2) and high-grade ccRCC (grades 3 and 4). The feature selection process consisted of three steps, including least absolute shrinkage and selection operator (LASSO) regression analysis, and the radiomics scores were developed using 48 radiomics features (10 in the unenhanced phase, 17 in the corticomedullary (CM) phase, 14 in the nephrographic (NP) phase, and 7 in the excretory phase). The radiomics score (Rad-Score) derived from the CM phase achieved the best predictive ability, with a sensitivity, specificity, and an area under the curve (AUC) of 90.91%, 95.00%, and 0.97 in the training set. In the validation set, the Rad-Score derived from the NP phase achieved the best predictive ability, with a sensitivity, specificity, and an AUC of 72.73%, 85.30%, and 0.84. We constructed a complex model, adding the radiomics score for each of the phases to the clinicoradiological characteristics, and found significantly better performance in the discrimination of the nuclear grades of ccRCCs in all MDCT phases. The highest AUC of 0.99 (95% CI, 0.92–1.00, $p < 0.0001$) was demonstrated for the CM phase. Our results showed that the MDCT radiomics features may play a role as potential imaging biomarkers to preoperatively predict the WHO/ISUP grade of ccRCCs.

Keywords: clear cell renal cell carcinoma; radiomics; WHO/ISUP nuclear grade; multiphasic multidetector computed tomography

Citation: Moldovanu, C.-G.; Boca, B.; Lebovici, A.; Tamas-Szora, A.; Feier, D.S.; Crisan, N.; Andras, I.; Buruian, M.M. Preoperative Predicting the WHO/ISUP Nuclear Grade of Clear Cell Renal Cell Carcinoma by Computed Tomography-Based Radiomics Features. *J. Pers. Med.* **2021**, *11*, 8. https://dx.doi.org/10.3390/jpm11010008

Received: 22 November 2020
Accepted: 21 December 2020
Published: 23 December 2020

1. Introduction

Clear cell renal cell carcinoma (ccRCC) encompasses around 70% of all renal cell carcinomas, making it the most common pathological subtype [1,2]. It has the worst prognosis of all types of RCC, and its biological aggressiveness significantly changes the prognosis [3].

Tumor grading is among the most important prognostic factors as an independent predictor of cancer-specific survival for ccRCC stages [4]. The World Health Organization/International Society of Urological Pathology (WHO/ISUP) grading system for ccRCC [5] has improved interobserver reproducibility compared to the former Fuhrman grading system, being easier to apply and more clinically relevant. This four-grade system is based primarily on nucleolar prominence assessed to determine grades 1–3. Grade 4 is defined by the presence of highly atypical "pleomorphic" cells and/or sarcomatoid or rhabdoid morphology. Grades 1–2 are classified as low grades, and grades 3–4 are classified as high grades. Patients with low-grade ccRCC may be candidates for less invasive procedures, such as nephron-saving surgery, radiofrequency ablation, or active surveillance, whereas radical interventions are acceptable in patients with high-grade ccRCC [6].

Percutaneous renal mass biopsy is an accurate procedure that can identify the histology of the lesions [7]. Due to the heterogeneity of ccRCCs, the accuracy of tumor grading through biopsy is controversial, as the biopsy shows some discrepancies of the resection sample for grading systems. Some studies focusing on renal tumor biopsies and tumor grading [8–11] have reported that biopsies usually underestimate the final grade and less often overestimate the final grade. The percentage of accurate biopsy grading was reported between 43% and 75%, and the percentage of differentiation between low and high grade was reported between 64% and 87%. Moreover, different parts of a tumor have distinct molecular characteristics and such differences change over time. Thus, optimal characterization of tumor grading by percutaneous biopsy cannot be obtained properly because it is not possible to biopsy each part of a tumor at different times [12,13].

The field of medical and biological image analysis has recently grown exponentially, and a new method called radiomics has been developed [14–16]. Radiomics is a promising technique that extracts and analyzes large numbers of imaging features to provide more information than only human imaging evaluation can offer. This method uses high-throughput extraction of large numbers of quantitative radiomics features obtained from medical images using advanced mathematical algorithms to determine tumor phenotypes [17–19]. Thus, the heterogeneity of the entire tumor volume is assessed compared to biopsies that assess the heterogeneity in a small portion of the tumor and at a single anatomical site [20–24]. Several previous studies [25–32] have shown that radiomics features based on multiphasic multidetector computed tomography (MDCT) images perform efficiently in differentiating between high-/low-grade ccRCC tumors. Given these promising results, we assume that MDCT-based radiomics features may play a feasible role in predicting high-/low-grade ccRCCs. This study aims to evaluate if radiomics features extracted from a four-phase MDCT study may be helpful to preoperatively differentiate the WHO/ISUP nuclear grades of ccRCCs.

2. Materials and Methods

The ethical approval for this retrospective study was obtained from the Institutional Review Board of Clinical Municipal Hospital of Cluj-Napoca (Approval Code: No. 15/2020; Approval Date: 11 June 2020). No formal written consent was required for this study.

2.1. Study Population

We performed a retrospective analysis of the medical database for patients with pathologically proven ccRCC from January 2018 to February 2020. The inclusion criteria were as follows: patients with four-phase MDCT scan before surgery; WHO/ISUP nuclear grades, which were available from the pathology reports. The exclusion criteria were: significant artifacts on images (motion or metal artifacts), previous tumor treatment, and patients with cystic lesions. Our study comprised 102 patients (mean age: 61.92 ± 13.03), which were divided into two groups: the training set (62 patients) and the validation set (40 patients).

2.2. Image Acquisition

MDCT scans were performed with a 64-row scanner (Somatom Sensation, Siemens, Erlangen, Germany) using: a 120 kV variable tube current (variable setting from 200 to 400 mAs based on patient size); section collimation, 0.6 mm; table feed, 5 mm/s; slice thickness, 3.0 mm; and a pitch of 1. Nonionic contrast material was injected via an antecubital vein at a rate of 3.0 mL/s using a CT-compatible power injector with a total volume of 80–150 mL. A region of interest (ROI) in the thoracoabdominal aorta junction was placed, with a trigger set to begin at 150 HU. The renal mass protocol consisted of a four-phase study: an unenhanced (UN) scan followed by contrast-enhanced acquisitions during the corticomedullary (CM, 30 s delay), nephrographic (NP, 90 s delay), and excretory (EX, 8 min delay) phases.

2.3. Histopathological Assessment of Nuclear Grade

WHO/ISUP nuclear grades were obtained from the pathology reports of the histopathological examination. The samples were obtained from the partial nephrectomy of 22 patients, total nephrectomy of 13 patients, and radical nephrectomy of 67 patients. All tumors were divided into low-grade ccRCC (WHO/ISUP grades 1 and 2) and high-grade ccRCC (WHO/ISUP grades 3 and 4).

2.4. Tumor Segmentation, Preprocessing, and Radiomics Feature Extraction

From the pictured archiving and communication system (PACS, Carestream, Canada), all MDCT acquisitions were exported and transferred to a workstation to be segmented using the open-source 3D Slicer software, version 4.10.2 (www.slicer.org). For each renal mass, the volume of interest (VOI) segmentation was manually and slightly delineated slice by slice by a radiology resident (Claudia-Gabriela Moldovanu), in accordance with a senior radiologist with 9 years of experience in urogenital imaging (Attila Tamas-Szora) to ensure the accuracy of the tumor boundaries. The two radiologists were blinded to the pathological results. To minimize the partial volume effect from surrounding structures, the segmentations were carefully delineated, reducing the size of the tumors by 1 mm from the current visible edge. The nephrographic phase was used for segmentation because it provides an adequate delimitation between the tumor and uninvolved adjacent parenchyma (Figure 1).

Prior to radiomics features extraction, the images of each patient were preprocessed: first, the images and VOIs were resampled to an isotropic voxel size of $1 \times 1 \times 1$ mm^3 using B-Spline interpolation; then, normalization of the images was performed by centering in the chosen place by division through standard deviation; finally, image discretization was performed of the gray level by a fixed bin width of 25 in the histogram.

A total of 4184 radiomics features of the four-phase MDCT study per patient (1046 features per phase) were extracted from the VOIs and divided into four groups: (1) image intensity (first-order statistics features); (2) shape and size-based features; (3) second-order statistics features (textural features); and (4) higher-order statistical features (obtained after applying filters and mathematical transforms to the images). We used Laplacian transforms of Gaussian-filter- and wavelet-transformed images. The Laplacian of Gaussian (LoG) filter was used with values of 2 mm, 4 mm, and 6 mm, representing fine, medium, and coarse patterns, respectively. Wavelet-based texture features were generated using eight different frequency band combinations, applying either a high- or low-pass filter in each of the three dimensions including high–high–high, high–high–low, high–low–low, high–low–high, low–high–low, low–high–high, low–low–high, and low–low–low. Radiomics features were extracted from images with and without preprocessing filters from all four MDCT phases separately. PyRadiomics version 2.1.2. was used for both preprocessing and feature extraction.

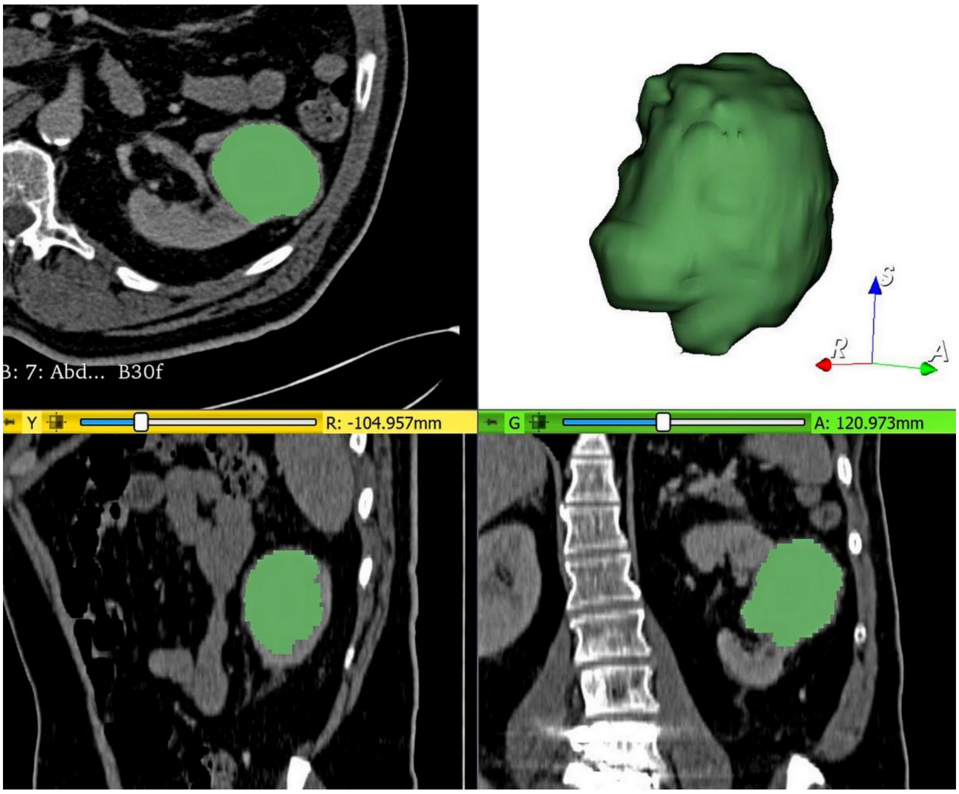

Figure 1. Example of volume of interest (VOI) segmentation in the nephrographic (NP) phase of a pathologically proven clear cell renal cell carcinoma (ccRCC).

2.5. Reliability Validation of Texture Features

According to previously published guidelines [33–35], the reproducibility of texture features was calculated using the interclass correlation coefficient (ICC) of the radiomics features. Another radiologist (Andrei Lebovici, with 8 years of experience in urogenital imaging) independently resegmented all renal masses and extracted radiomics features, also blinded by the pathological results. Thus, for each extracted texture features, the ICC was calculated. For the feature selection process, the features with an ICC value of $\geq$0.75 were included, indicating excellent reproducibility, resulting in a total of 3429 features (826 in the UN phase, 861 in the CM phase, 864 in the NP phase, and 878 in the EX phase).

2.6. Statistical Analysis

Statistical analysis was performed using SPSS Statistics software for Windows, version 18.0 (SPSS Inc., Chicago, IL, USA) and R software version 3.6.3 using the "glmnet" package. The Mann–Whitney U-test was used for univariate analysis to identify the features with a significant difference between low/high-grade ccRCC groups. The Benjamini–Hochberg (BH) correction method was applied to control the false discovery rate in multiple hypothesis testing. BH-adjusted p-values < 0.05 were considered significant. Spearman's correlation coefficient was used to assess the correlation between all radiomics features. This was performed between any two features, and when the Spearman coefficient was > 0.9/< $-$0.9, the feature with the higher p-value in the univariate analysis was eliminated. For standard comparison and mitigating the effects of the data splitting, the radiomics scores were built using the least absolute shrinkage and selection operator (LASSO) performed by 10-fold cross-validation. The radiomics score (Rad-Score) was computed for each MDCT phase of each patient through a linear combination of features weighted by their LASSO coefficients. To evaluate the predictive performance of the radiomics score for the differentiating ability of low/high-grade ccRCC in the training and validation sets, the area under the receiver operating characteristic (ROC) curve (AUC) was used, and $p < 0.05$ was considered statistically significant. Multivariate analysis using binary logistic regression (enter method) was conducted to detect independent predictors of the WHO/ISUP nuclear grade of ccRCCs, including the clinicoradiological characteristics and radiomics score as independent variables.

3. Results

3.1. Patients Characteristics

A total of 102 patients (mean age: 61.92 ± 13.03) were included in this study, divided into training sets and validation sets based on the random split method. Thus, 62 patients constituted the training set (40 men, 22 women; mean age: 61.09 ± 12.64), whereas 40 patients constituted the validation set (27 men, 13 women; mean age: 63.2 ± 13.66). In the training set, 40 patients were classified according to the WHO/ISUP grading system as low-grade ccRCC, and the remaining 22 patients were classified as high-grade ccRCC. The validation set comprised 29 patients with low-grade ccRCC and 11 patients with high-grade ccRCC. The baseline characteristics of training and validation sets are provided in Table 1.

Table 1. Demographic and clinicoradiological characteristics of the study population. * $p < 0.05$ was considered statistically significant.

	Training Set			**Validation Set**		
Characteristic	**Low Grade**	**High Grade**	***p*-Value**	**Low Grade**	**High Grade**	***p*-Value**
Number	40	22		29	11	
Age (years)	58.2 ± 12.92	66.36 ± 10.45	0.009 *	61.89 ± 13.30	66.63 ± 14.66	0.36
Gender			0.91			1.00
Male	26 (65%)	14 (35%)		20 (74.1%)	7 (25.9%)	
Female	14 (63.6%)	8 (36.4%)		9 (69.2%)	4 (30.8%)	
Tumor size (mm)	46.65 ± 28.53	73.22 ± 26.25	0.001 *	53.17 ± 22.68	79.45 ± 25.15	0.008 *
Tumor stage (n)			0.001 *			0.01 *
1	30 (85.7%)	5 (14.3%)		18 (94.7%)	1 (5.3%)	
2	3 (50%)	3 (50%)		6 (100%)	-	
3	7 (35%)	13 (65%)		5 (35.7)	9 (64.3%)	
4	-	1 (100%)		-	1 (100%)	
Vein thrombosis			0.02 *			0.009 *
No	33 (73.3%)	12 (26.6%)		22 (88%)	3 (12%)	
Yes	7 (41.1%)	10 (58.8%)		7 (46.6%)	8 (53.3%)	
Tumor necrosis			0.47			1.00
No	7 (77.7%)	2 (22.2%)		2 (66.6%)	1 (33.3%)	
Yes	33 (60%)	22 (40%)		27 (72.9%)	10 (27.0%)	
Perinephritic invasion			0.009 *			0.49
No	34 (73.9%)	12 (26.0%)		12 (80%)	3 (20%)	
Yes	6 (37.5%)	10 (62.5%)		17 (68%)	8 (32%)	
Intratumoral neovascularity			0.003 *			0.29
No	30 (78.9%)	8 (21.0%)		11 (85.6%)	2 (15.3%)	
Yes	10 (41.6%)	14 (58.3%)		18 (66.6%)	9 (33.3%)	
Hemorrhage			0.01 *			0.48
No	32 (74.4%)	11 (25.5%)		16 (80%)	4 (20%)	
Yes	8 (42.1%)	11 (57.8%)		13 (65%)	7 (35%)	
Lymphadenopathy			0.05			0.12
No	35 (71.4%)	14 (28.5%)		27 (77.1%)	8 (22.8%)	
Yes	5 (38.4%)	8 (61.5%)		2 (40%)	3 (60%)	

No significant difference in the gender of the patients, N stage, and intratumoral necrosis between low- and high-grade ccRCC in both the training and validation sets was observed. However, significant differences were observed in the ages of the patients, tumor size, tumor stage, vein thrombosis, perinephric fat invasion, intratumoral neovascularity, and intratumoral hemorrhage in the training set. These results are partially confirmed in the validation set, where tumor size, tumor stage, and vein thrombosis were the only significantly different characteristics.

3.2. Feature Selection and Radiomics Score Building: Training Set

Feature selection and radiomics score building were separately performed on each MDCT phase of each patient. According to the standard of ICC ≥ 0.75 in the inter-reader agreement evaluation, 826 radiomics features from the UN phase, 861 features from the CM phase, 864 features from the NP phase, and 878 features from the EX phase were highly reproducible and selected for further analysis.

To develop the radiomics signature, univariate analysis was performed to assess the potential of the radiomics features to differentiate between the low- and high-grade ccRCC groups. Excluding those with an adjusted p-value > 0.05, the number of features was further decreased to 1241 features (228 in the UN phase, 387 in the CM phase, 340 in the NP phase, and 286 in the EX phase). These features were included in the further selection process.

After applying the Spearman correlation analysis, these features were secondly reduced to 302 potential predictors (46 in the UN phase, 110 in the CM phase, 85 in the NP phase, and 61 in the EX phase). Furthermore, the LASSO binary logistic regression algorithm was used to reduce the dimensionality of the above high-dimensional features; thus, the best features were selected based on the optimal λ parameters. Forty-eight radiomics features with nonzero coefficients were then selected to construct the radiomics scores across all MDCT phases (10 in the UN phase, 17 in the CM phase, 14 in the NP phase, and 7 in the EX phase). Most of the features included in the radiomics scores were obtained from filtered images using LoG and wavelet-transformed filters, being mainly texture and first-order features (Table 2).

Table 2. List of selected radiomics features and their coefficients for calculating the radiomics score.

Radiomic Group	Radiomic Feature	Associated Filter	Coefficient
UN phase			
	Intercept		−0.872
Texture feature	JointAverage	LoG filter (2 mm)	0.409
Texture feature	SizeZoneNonUniformity	LoG filter (2 mm)	0.010
Texture feature	DependenceVariance	LoG filter (4 mm)	0.362
First-order	Minimum	LoG filter (4 mm)	−0.296
Texture feature	LongRunEmphasis	LoG filter (4 mm)	0.477
Texture feature	SmallAreaHighGrayLevelEmphasis	LoG filter (4 mm)	0.091
Texture feature	LargeAreaLowGrayLevelEmphasis	Wavelet-LHL	0.039
Texture feature	LongRunLowGrayLevelEmphasis	Wavelet-LLH	−0.431
Texture feature	SmallAreaLowGrayLevelEmphasis	Wavelet-LLH	−0.349
Texture feature	LongRunLowGrayLevelEmphasis	Wavelet-HHL	0.343
CM phase			
	Intercept		−1.184
Texture feature	SmallAreaLowGrayLevelEmphasis	Original	−0.387
First-order	Skewness	LoG filter (2 mm)	−0.311
First-order	Minimum	LoG filter (2 mm)	−0.052
First-order	10Percentile	LoG filter (2 mm)	0.303
Texture feature	LowGrayLevelEmphasis	LoG filter (4 mm)	−0.373
Texture feature	LongRunHighGrayLevelEmphasis	Wavelet-HLL	0.306
Texture feature	LowGrayLevelZoneEmphasis	Wavelet-HLL	−0.076
Texture feature	Imc2	Wavelet-LHL	0.797
First-order	Mean	Wavelet-LHL	0.516

Table 2. *Cont.*

Radiomic Group	Radiomic Feature	Associated Filter	Coefficient
Texture feature	GrayLevelNonUniformity	Wavelet-LHL	−0.153
Texture feature	SmallAreaEmphasis	Wavelet-LHL	0.823
Texture feature	LongRunLowGrayLevelEmphasis	Wavelet-LLH	−0.429
First-order	Maximum	Wavelet-HLH	0.583
Texture feature	GrayLevelVariance	Wavelet-HHL	0.084
First-order	Entropy	Wavelet-HHL	0.049
Texture feature	RunVariance	Wavelet-HHL	0.064
Texture feature	ShortRunLowGrayLevelEmphasis	Wavelet-LLL	−0.379
NP phase			
	Intercept		−0.765
Texture feature	HighGrayLevelRunEmphasis	Original	0.325
Texture feature	ShortRunHighGrayLevelEmphasis	LoG filter (6 mm)	−0.087
Texture feature	Imc2	Wavelet-HLL	0.191
Texture feature	ShortRunHighGrayLevelEmphasis	Wavelet-HLL	0.225
Texture feature	Contrast	Wavelet-LHL	0.192
Texture feature	SmallAreaHighGrayLevelEmphasis	Wavelet-LHL	0.353
Texture feature	ZoneEntropy	Wavelet-LHL	0.049
First-order	Entropy	Wavelet-LHH	0.070
Texture feature	DependenceNonUniformityNormalized	Wavelet-LLH	0.013
Texture feature	SumEntropy	Wavelet-HLH	−0.190
Texture feature	Imc2	Wavelet-HLH	0.331
Texture feature	GrayLevelVariance	Wavelet-HHL	0.019
Texture feature	Idn	Wavelet-LLL	0.223
Texture feature	SmallAreaLowGrayLevelEmphasis	Wavelet-LLL	−0.189
EX phase			
	Intercept		−0.653
Texture feature	DependenceVariance	LoG filter (4 mm)	−0.234
First-order	Kurtosis	LoG filter (4 mm)	0.139
Texture feature	RunVariance	LoG filter (4 mm)	0.163
Texture feature	SizeZoneNonUniformity	LoG filter (4 mm)	0.032
Texture feature	DependenceNonUniformityNormalized	Wavelet-HLL	0.165
Texture feature	SmallDependenceLowGrayLevelEmphasis	Wavelet-HLL	−0.046
Texture feature	SmallAreaHighGrayLevelEmphasis	Wavelet-LHL	0.028

A significant difference in the radiomics scores between low- and high-grade ccRCCs in all MDCT phases, with patients from the second group having higher values (Table 3), was observed. Rad-Score was calculated according to the following formula:

$$\mathrm{Rad-Score} = \sum_{c=0}^{a} Cc * \mathrm{Xc} + \mathrm{b}$$

where a is the number of radiomics features with nonzero coefficients for each MDCT phase (10 for the UN phase, 17 for the CM phase, 14 for the NP phase, and 7 for the EX phase), Cc is the coefficient of the cth feature, Xc the cth feature, and b the intercept.

3.3. Performance of the Radiomics Scores: Training Set

To compare the detection performance, the Rad-Scores were validated in terms of ROC curve and AUC in the training set (Figure 2). Sensitivity, specificity, positive predictive value (PPV), and negative predictive value (NPV) were also calculated. The radiomics scores showed a favorable predictive efficacy for differentiating low- from high-grade ccRCC based on each phase of the MDCT protocol. The results are summarized in Table 4. In the training set, the Rad-Scores derived from the UN and CM phases achieved the best predictive ability, with a sensitivity, specificity, and an AUC of 81.82%, 92.50%, and 0.89 in the UN phase and 90.91%, 95.00%, and 0.97 in the CM phase.

Table 3. Difference of the radiomics score (Rad-Score) between low- and high-grade ccRCC in the training and validation sets.

WHO/ISUP Nuclear Grades	Radiomic Score Mean ± SD	*p*-Value	MDCT Phase
Training set			
Low grade (n = 40)	−1.68 ± 1.16	$p < 0.001$	UN
	−2.50 ± 1.95	$p < 0.001$	CM
	−1.26 ± 0.68	$p < 0.001$	NP
	−0.92 ± 0.53	$p < 0.001$	EX
High grade (n = 22)	0.60 ± 1.34	$p < 0.001$	UN
	1.21 ± 1.29	$p < 0.001$	CM
	0.15 ± 1.18	$p < 0.001$	NP
	−0.16 ± 0.51	$p < 0.001$	EX
Validation set			
Low grade (n = 29)	−1.18 ± 1.70	$p = 0.051$	UN
	−2.21 ± 2.42	$p < 0.001$	CM
	−1.12 ± 0.72	$p = 0.001$	NP
	−0.80 ± 0.62	$p = 0.009$	EX
High grade (n = 11)	−0.03 ± 1.32	$p = 0.051$	UN
	1.53 ± 3.43	$p < 0.001$	CM
	0.19 ± 1.56	$p = 0.001$	NP
	−0.24 ± 0.45	$p = 0.009$	EX

Table 4. Radiomic score performance in the training and validation sets in all MDCT phases.

Variable	AUC (95% CI)	Se (95% CI)	Sp (95% CI)	PPV (95% CI)	NPV (95% CI)	Cut-Off Value	*p*-Value
Training set							
Radiomic score: UN phase	0.89 (0.796–0.961)	81.82 (59.7–94.8)	92.50 (79.6–98.4)	85.7 (63.7–97.0)	90.2 (76.9–97.3)	−0.34	<0.001
Radiomic score: CM phase	0.97 (0.89–0.99)	90.91 (70.8–98.9)	95.00 (83.1–99.4)	90.9 (70.8–98.9)	95.0 (83.1–99.4)	−0.25	<0.001
Radiomic score: NP phase	0.87 (0.76–0.94)	81.82 (59.7–94.8)	92.50 (79.6–98.4)	85.7 (63.7–97.0)	90.2 (76.9–97.3)	−0.55	<0.001
Radiomic score: EX phase	0.85 (0.73–0.92)	72.73 (49.8–89.3)	87.50 (73.2–95.8)	76.2 (52.8–91.8)	85.4 (70.8–94.4)	−0.34	<0.001
Validation set							
Radiomic score: UN phase	0.72 (0.56–0.85)	72.73 (39.0–94.0)	72.41 (52.8–87.3)	50.0 (24.7–75.3)	87.5 (67.6–97.3)	−0.43	0.0157
Radiomic score: CM phase	0.81 (0.66–0.92)	72.73 (39.0–94.0)	75.90 (56.5–89.7)	53.3 (26.6–78.7)	88.0 (68.8–97.5)	−0.85	<0.001
Radiomic score: NP phase	0.84 (0.69–0.93)	72.73 (39.0–94.0)	85.30 (68.3–96.1)	66.7 (34.9–90.1)	89.3 (71.8–97.7)	−0.58	<0.001
Radiomic score: EX phase	0.77 (0.61–0.89)	100.0 (71.5–100.0)	51.72 (32.5–70.6)	44.0 (24.4–65.1)	100.0 (78.2–100.0)	−0.88	<0.001

Using the variables with a significant difference among low- and high-grade ccRCCs in the training set (including age, tumor size, vein thrombosis, perinephric invasion, tumor stage (2–4), intratumoral neovascularity, and hemorrhage), we conducted a multivariate logistic regression analysis to develop a clinicoradiological model for the preoperative prediction of the WHO/ISUP nuclear grade of ccRCCs (Table 5). Further, we constructed four complex models, adding the radiomics score of each phase to the clinicoradiological model (Table 6).

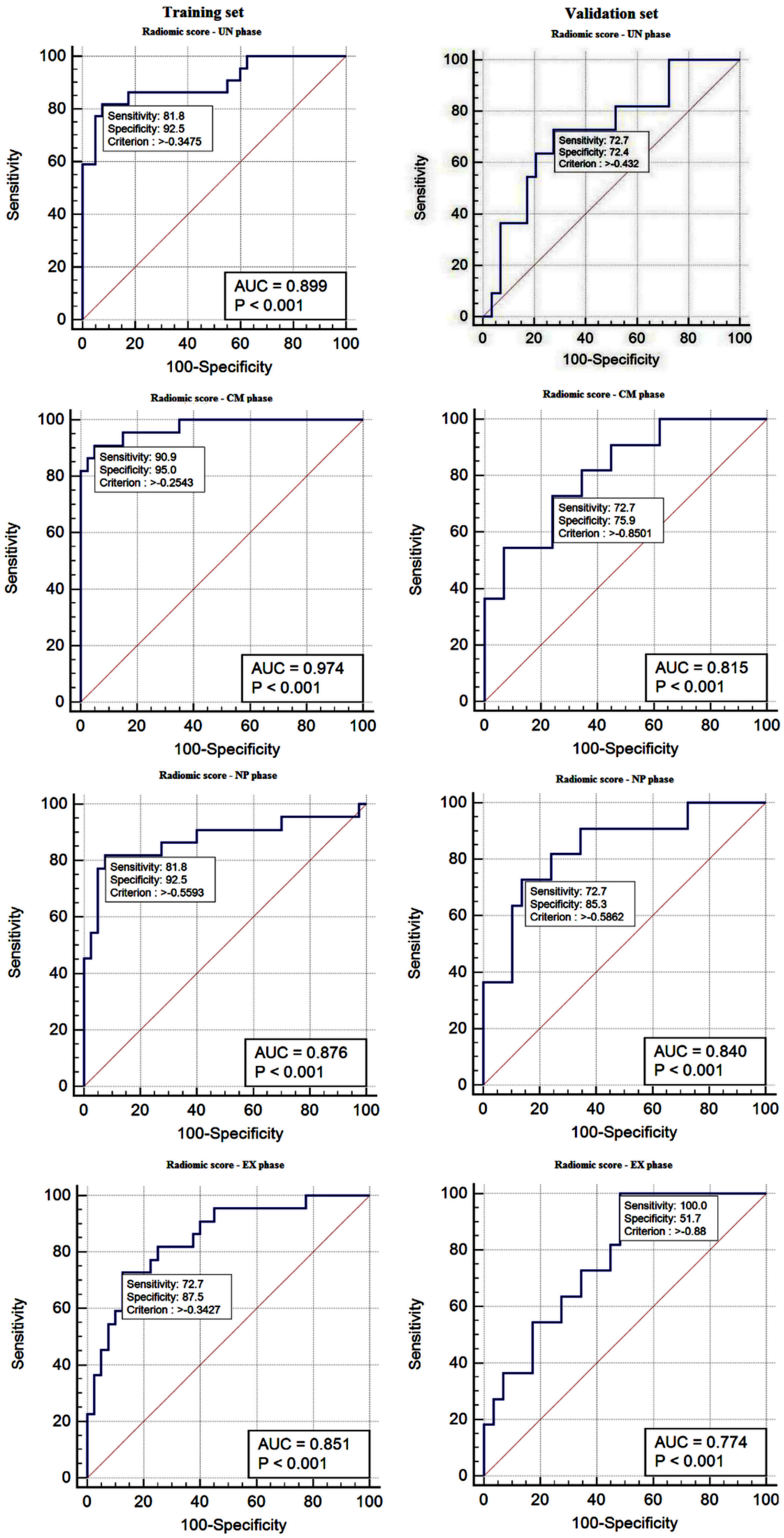

Figure 2. ROC curves of radiomics scores of all MDCT phases in the training and validation sets. ROC, receiver operating characteristic, AUC area under the curve.

Table 5. Multivariate logistic regression analysis for the preoperatively prediction of the WHO/ISUP nuclear grade of ccRCCs: clinicoradiological model.

Variable	Coefficient	Std. Error	p-Value	Odds Ratio (OR)
Age (years)	0.05	0.03	0.10	1.05
Tumor size (mm)	0.006	0.01	0.74	1.00
Vein thrombosis: positive	−1.32	1.22	0.27	0.26
Perinephric invasion: positive	1.60	1.39	0.25	4.98
Tumor stage (2, 3, or 4)	2.09	1.07	0.05	8.13
Intratumoral neovascularity: positive	1.04	0.99	0.29	2.85
Hemorrhage: positive	−1.81	1.55	0.24	0.16
Constant	−5.55			

Table 6. Multivariate logistic regression analysis for the preoperative prediction of the WHO/ISUP nuclear grade of ccRCCs: complex model.

Variable	Coefficient	Std. Error	p-Value	Odds Ratio (OR)
UN phase				
Age (years)	0.03	0.05	0.4997	1.03
Tumor size (mm)	−0.02	0.02	0.4156	0.97
Vein thrombosis: positive	1.64	1.81	0.3653	5.16
Perinephric invasion: positive	−0.17	1.73	0.9176	0.83
Tumor stage (2, 3, or 4)	0.99	1.42	0.4860	2.70
Intratumoral neovascularity: positive	0.07	1.17	0.9485	1.07
Hemorrhage: positive	−1.75	1.87	0.34	0.17
Radiomic score: UN phase	1.83	0.59	0.0021	6.27
Constant	−0.90			
CM phase				
Age (years)	0.12	0.09	0.1772	1.13
Tumor size (mm)	−0.08	0.07	0.2576	0.91
Vein thrombosis: positive	1.13	16.78	0.9460	3.11
Perinephric invasion: positive	2.76	17.36	0.8735	15.86
Tumor stage (2, 3, or 4)	3.62	3.38	0.2837	37.59
Intratumoral neovascularity: positive	−2.36	2.85	0.4075	3.11
Hemorrhage: positive	−4.07	17.52	0.8161	0.01
Radiomic score: CM phase	4.92	2.37	0.0384	137.75
Constant	−1.50			
NP phase				
Age (years)	0.11	0.05	0.03	1.12
Tumor size (mm)	−0.03	0.02	0.2121	0.96
Vein thrombosis: positive	−3.15	1.68	0.0610	0.04
Perinephric invasion: positive	3.88	2.23	0.0827	48.76
Tumor stage (2, 3, or 4)	2.19	1.50	0.1449	8.98
Intratumoral neovascularity: positive	0.34	1.24	0.7830	1.41
Hemorrhage: positive				
Radiomic score: NP phase	2.78	0.91	0.0023	16.17
Constant	−4.64			
EX phase				
Age (years)	0.05	0.04	0.2408	1.05
Tumor size (mm)	−0.05	0.03	0.0879	0.94
Vein thrombosis: positive	−0.24	1.42	0.8639	0.78
Perinephric invasion: positive	1.01	1.57	0.5184	2.77
Tumor stage (2, 3, or 4)	1.87	1.19	0.1170	6.49
Intratumoral neovascularity: positive	0.09	1.07	0.9263	1.10
Hemorrhage: positive	−1.20	1.71	0.4832	0.29
Radiomic score: EX phase	4.64	1.75	0.0081	103.88
Constant	1.40			

The ability of the clincoradiological model and the complex model to categorize nuclear grades was evaluated by the AUC of the ROC curves (Figure 3). The clincoradiological model showed a high performance in the discrimination of low- and high-grade ccRCCs with an AUC of 0.83 (95% CI, 0.71–0.91, $p < 0.0001$). We found that the addition of radiomics score to the clincoradiological characteristics improved their performance in all MDCT phases: AUC = 0.93 (95% CI, 0.84–0.98, $p < 0.0001$) vs. AUC = 0.89 (95% CI, 0.79–0.96, $p < 0.0001$) in the UN phase, AUC = 0.99 (95% CI, 0.92–1.00, $p < 0.0001$) vs. AUC = 0.97 (95% CI, 0.89–0.99, $p < 0.0001$) in the CM phase, AUC = 0.91 (95% CI, 0.81–0.97, $p < 0.0001$) vs. AUC = 0.87 (95% CI, 0.76–0.94, $p < 0.0001$) in the NP phase, AUC = 0.87 (95% CI, 0.77–0.94, $p < 0.0001$) vs. AUC = 0.85 (95% CI, 0.73–0.92, $p < 0.0001$) in the EX phase.

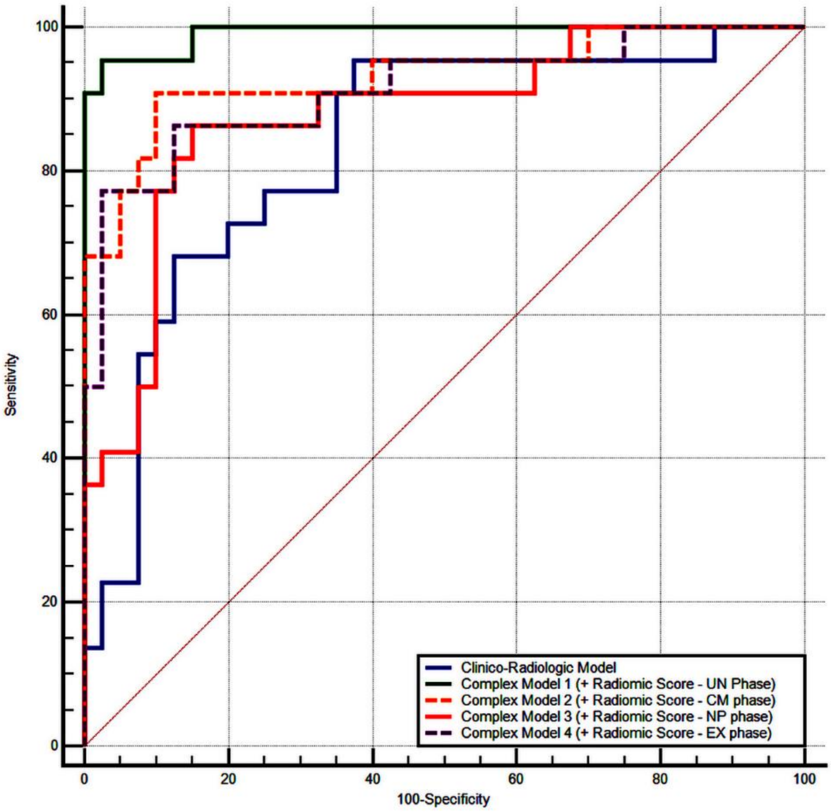

Figure 3. ROC curves of the clincoradiological model and complex models to categorize the nuclear grades of ccRCC.

3.4. Validation of the Radiomics Score

The performance of the Rad-Scores for the discrimination of low- and high-grade ccRCCs was confirmed in the validation set in each MDCT phase of each patient (Table 3). ROC curve analysis was conducted, and the AUC, sensitivity, specificity, PPV, and NPV for the determined cut-off values were calculated. The results are presented in Figure 2 and Table 4. Compared with the training set, in the validation set, the Rad-Scores derived from the CM and NP phases achieved the best predictive ability, with a sensitivity, specificity, and an AUC of 72.73%, 75.90%, and 0.81 in the CM phase and 72.73%, 85.30%, and 0.84 in the NP phase.

4. Discussion

In this study, we evaluated if radiomics features extracted from a four-phase MDCT study may be helpful to preoperatively differentiate the WHO/ISUP nuclear grades of ccRCC. In the era of personalized medicine, radiomics features, along with metabolic, histopathologic, and genetic datasets, may be useful to improve patient management, a biomarker that could be useful in tumor characterization, treatment selection, and prognosis [36–39]. Many radiomics features have proven to be useful in differentiating between early- and advanced-stage diseases of various types of cancers [40–43]. In recent years, concerning renal imaging, little research [25–32] has investigated the radiomics potential based on MDCT to predict the ccRCC nuclear grade. Regarding the histologic tumor grading system, the majority of studies used the Fuhrman classification system as a pathological reference. Although the Fuhrman and WHO/ISUP grading systems are linboth used in current medical practice for ccRCC grading, some studies [44–47] have reported that the Fuhrman grading system has poor interobserver reproducibility compared to the new WHO/ISUP grading system.

In recent years, the WHO/ISUP grading system has been accepted in current medical practice, replacing the former Fuhrman grading system. To the best of our knowledge, there are only a few published papers that have studied radiomics features based on MDCT for predicting the ccRCC WHO/ISUP nuclear grade [29,48–51]. However, no previous work used parameters extracted from a four-phase MDCT study to develop the prediction model, as our study does.

Our results show that our constructed MDCT-based radiomics scores using a four-phase protocol achieved a considerably promising performance in differentiating high- from low-grade ccRCCs. The Rad-Scores derived from the UN and CM phases achieved the best predictive ability in the training set. However, in the validation set, the Rad-Scores from the CM and NP phases achieved the best predictive ability. We found that the best predictive ability with an AUC of 0.94 was for the CM phase in the training dataset and 0.84 was for the NP phase in the validation datasets. This diversity illuminates that the CM and NP phases are valuable and necessary for ccRCC grading. Our results are in concordance with the results of previous studies on ccRCC grading using texture analysis or machine learning (ML), which reported an accuracy between 0.78 and 0.82 and an AUC between 0.71 and 0.98 [29,48,49].

Our feature selection results showed that the first-order features and second-order statistics features were significantly associated with the WHO/ISUP grade. In building our radiomics scores, most of the features included were obtained from filtered images, especially from wavelet-transformed filters. Shu et al. [50] used two predictive models constructed by radiomics features extracted from the nephrographic and medullary phases and reported no significant difference in the AUC between them to differentiate low- from high-grade ccRCC. Conversely, they showed that the combined model of radiomics features from two certain phases had the highest differential diagnostic efficiency (AUC: 0.82 (95% CI: 0.76–0.86). A recent study [51] showed that the value of the NP phase is limited in predicting the ISUP grade. This may be due to two reasons: firstly, regarding tumor delineation, Sun et al. used a single-slice approach (largest cross-section diameter of the tumor) and did not perform data analysis of the entire tumor VOI. Although VOIs segmentations are time-consuming processes, we believe that the single-slice approach does not fully reflect the heterogeneity of the tumor, and the information obtained from the VOI might be more reliable for the characterization of the tumor. Secondly, their features extraction algorithm is different; they extracted the radiomics features from original and wavelet-filtered images, without the use of LoG filters. It is known that filtered-based images can limit the impact of technical noise [52]. More and more studies are using them, but a current technical standardization regarding their use has not yet been established [53].

MRI-derived ADC values are useful in characterizing tumor activity [54]. Some studies [55,56] that evaluated the utility of ADC to differentiate low- from high-grade ccRCC reported that MRI has a favorable predictive accuracy in detecting high-grade ccRCC (AUC = 0.80). With all its advantages, MRI is not as widely used as MDCT for the analysis of renal masses, being used only in selected cases. Cui et al. [48] used MRI- and CT-based radiomics models to differentiate low- from high-grade ccRCCs, and then the authors compared their performance. They reported that radiomics models based on a three-phase

MDCT performed better than the radiomics model based on a single-phase MDCT, with an ACC ranging from 77 to 79% in internal validation and 61 to 69% in external validation.

Similarly, the radiomics model based on all-sequence MRI was also superior to the radiomics model based on single-sequence MRI, with an ACC ranging from 71 to 73% in internal validation and 64 to 74% in external validation. When comparing the performance between MDCT and MRI, they found that the MRI-based radiomics model had performed better than the MDCT-based radiomics model for diagnosing low-grade ccRCC and showed a similar ability for diagnosing high-grade ccRCC.

Regarding the statistical approach, our study included one classification method: the binary logistic regression method. This algorithm is used to predict the probability of the class of a categorical dependent variable [57]. Several studies [58,59] have assessed the performance of quantitative MDCT texture analysis combined with different machine-learning-based classifiers to discriminate low- from high-grade ccRCC. It was observed that the highest predictive performance was obtained by the support vector machine classifier. However, these results were obtained for the Fuhrman grading system of ccRCC. Despite differences in the procedure followed, we believe that all studies support each other with the same conclusion that MDCT-based radiomics features may be a promising noninvasive method in predicting preoperative ccRCC grades.

In this study, the radiomics scores combined with the clinicoradiological characteristics showed a high performance in the discrimination of ccRCC grades. Two characteristics (age and tumor stage) were consistent with previous studies [29,56]. Li et al. proved a correlation between radiological characteristics and the ccRCC nuclear grade [28]. Shape, margin, and necrosis may be independent predictors of high-grade ccRCC, whereas a regular shape can often be seen in low-grade ccRCC lesions [28]. Another paper [60] demonstrated statistically significant differences in WHO/ISUP grading and pT staging between ccRCCs. In addition, they found that coagulative necrosis often occurs in high-grade and high-stage tumors.

This study may have important practical implications. The new WHO/ISUP grading system is a prognostic factor for ccRCCs. ccRCC grades were strongly related to patient outcomes and tumor biological behavior [61,62]. If low-grade tumors can be identified preoperatively, the treatment would consist of less invasive procedures. Moreover, partial nephrectomy can preserve partial renal function, thus reducing overall mortality and the incidence of cardiovascular disease [63]. Therefore, medical images can become a valuable source of information, and radiomics features may be used as a noninvasive method for characterizing and classifying lesions. However, further larger prospective studies to validate the performance of our proposed radiomics model in differentiating high from low-grade ccRCC are necessary for the future.

The present study has some limitations. (1) It was a single-center retrospective study with a small sample size of patients. (2) The statistical approach included one classification method, the binary logistic regression method, and advanced classifiers may offer better prediction performance. (3) External validation in more centers with more samples size is needed to overcome these limitations and validate the results in order to improve generalization and evaluate the potential for clinical translation of our radiomics models. (4) Volume effect interference cannot be completely avoided due to the fact that the tumor boundary was manually drawn. (5) The four-phase MDCT renal mass protocol involves a high dose of radiation to the patient and should be performed where it is necessary to discriminate the lesions before treatment selection.

5. Conclusions

Although there are limitations with regard to sample size, we have shown that radiomics features extracted from the four-phase MDCT study may play a role as a potential imaging biomarker to predict preoperatively the WHO/ISUP grade of ccRCCs, helping urologists to better stratify patients and choose the best treatment.

Author Contributions: Conceptualization, C.-G.M., A.L., A.T.-S., D.S.F., and M.M.B.; methodology, C.-G.M., A.L., A.T.-S., N.C., D.S.F., and I.A.; software, C.-G.M., A.T.-S., and A.L.; formal analysis, B.B. and D.S.F.; investigation, C.-G.M., A.L., and A.T.-S.; resources, C.-G.M.; data curation, C.-G.M. and B.B.; writing—original draft preparation, C.-G.M.; writing—review and editing, A.L., A.T.-S., N.C., D.S.F., B.B., I.A., and M.M.B.; visualization, C.-G.M. and M.M.B.; supervision, M.M.B.; project administration, M.M.B. All authors have read and agreed to the published version of the manuscript.

Funding: This research received no external funding.

Conflicts of Interest: The authors declare no conflict of interest.

References

1. Medina-Rico, M.; López-Ramos, H.; Lobo, M.; Romo, J.; Prada, J.G. Epidemiology of renal cancer in developing countries: Review of the literature. *Can. Urol. Assoc. J.* **2018**, *12*, 154–162. [CrossRef] [PubMed]
2. Znaor, A.; Lortet-Tieulent, J.; Laversanne, M.; Jemal, A.; Bray, F. International Variations and Trends in Renal Cell Carcinoma Incidence and Mortality. *Eur. Urol.* **2015**, *67*, 519–530. [CrossRef] [PubMed]
3. Muglia, V.F.; Prando, A. Renal cell carcinoma: Histological classification and correlation with imaging findings. *Radiol. Bras.* **2015**, *48*, 166–174. [CrossRef] [PubMed]
4. Zhang, G.; Wu, Y.; Zhang, J.; Fang, Z.; Liu, Z.; Xu, Z.; Fan, Y. Nomograms for predicting long-term overall survival and disease-specific survival of patients with clear cell renal cell carcinoma. *Onco Targets Ther.* **2018**, *11*, 5535–5544. [CrossRef]
5. Perrino, C.M.; Cramer, H.M.; Chen, S.; Idrees, M.T.; Wu, H.H. World Health Organization (WHO)/International Society of Urological Pathology (ISUP) grading in fine-needle aspiration biopsies of renal masses. *Diagn. Cytopathol.* **2018**, *46*, 895–900. [CrossRef]
6. Bhatt, J.R.; Finelli, A. Landmarks in the diagnosis and treatment of renal cell carcinoma. *Nat. Rev. Urol.* **2014**, *11*, 517–525. [CrossRef]
7. Neuzillet, Y.; Lechevallier, E.; Andre, M.; Daniel, L.; Coulange, C. Accuracy and Clinical Role of Fine Needle Percutaneous Biopsy with Computerized Tomography Guidance of Small (Less Than 4.0 Cm) Renal Masses. *J. Urol.* **2004**, *171*, 1802–1805. [CrossRef]
8. Lebret, T.; Poulain, J.E.; Molinié, V.; Herve, J.M.; Denoux, Y.; Guth, A.; Scherrer, A.; Botto, H. Percutaneous Core Biopsy for Renal Masses: Indications, Accuracy and Results. *J. Urol.* **2007**, *178*, 1184–1188. [CrossRef]
9. Blumenfeld, A.J.; Guru, K.; Fuchs, G.J.; Kim, H.L. Percutaneous Biopsy of Renal Cell Carcinoma Underestimates Nuclear Grade. *Urology* **2010**, *76*, 610–613. [CrossRef]
10. Ficarra, V.; Brunelli, M.; Novara, G.; D'Elia, C.; Segala, D.; Gardiman, M.; Artibani, W.; Martignoni, G. Accuracy of on-bench biopsies in the evaluation of the histological subtype, grade, and necrosis of renal tumours. *Pathology* **2011**, *43*, 149–155. [CrossRef]
11. Jeldres, C.; Sun, M.; Liberman, D.; Leghezzani, G.; de la Taille, A.; Tostain, J.; Valeri, A.; Cindolo, L.; Ficarra, V.; Artibani, W.; et al. Can renal mass biopsy assessment of tumor grade be safely substituted for by a predictive model? *J. Urol.* **2009**, *182*, 2585–2589. [CrossRef] [PubMed]
12. Millet, I.; Curros, F.; Serre, I.; Taourel, P.; Thuret, R. Can Renal Biopsy Accurately Predict Histological Subtype and Fuhrman Grade of Renal Cell Carcinoma? *J. Urol.* **2012**, *188*, 1690–1694. [CrossRef] [PubMed]
13. Kutikov, A.; Smaldone, M.C.; Uzzo, R.G.; Haifler, M.; Bratslavsky, G.; Leibovich, B.C. Renal Mass Biopsy: Always, Sometimes, or Never? *Eur. Urol.* **2016**, *70*, 403–406. [CrossRef] [PubMed]
14. Rizzo, S.; Botta, F.; Raimondi, S.; Origgi, D.; Fanciullo, C.; Morganti, A.G.; Bellomi, M. Radiomics: The facts and the challenges of image analysis. *Eur. Radiol. Exp.* **2018**, *2*, 1–8. [CrossRef] [PubMed]
15. Keek, S.A.; Leijenaar, R.T.; Jochems, A.; Woodruff, H.C. A review on radiomics and the future of theranostics for patient selection in precision medicine. *Brit. J. Radiol.* **2018**, *91*, 20170926. [CrossRef]
16. Gillies, R.J.; Kinahan, P.E.; Hricak, H. Radiomics: Images Are More than Pictures, They Are Data. *Radiology* **2016**, *278*, 563–577. [CrossRef]
17. Mayerhoefer, M.E.; Materka, A.; Langs, G.; Häggström, I.; Szczypiński, P.; Gibbs, P.; Cook, G. Introduction to Radiomics. *J. Nucl. Med.* **2020**, *61*, 488–495. [CrossRef]
18. Lubner, M.G.; Smith, A.D.; Sandrasegaran, K.; Sahani, D.V.; Pickhardt, P.J. CT Texture Analysis: Definitions, Applications, Biologic Correlates, and Challenges. *Radiographics* **2017**, *37*, 1483–1503. [CrossRef]
19. Capobianco, E.; Dominietto, M. From Medical Imaging to Radiomics: Role of Data Science for Advancing Precision Health. *J. Pers. Med.* **2020**, *10*, 15. [CrossRef]
20. Van Timmeren, J.E.; Cester, D.; Tanadini-Lang, S.; Alkadhi, H.; Baessler, B. Radiomics in medical imaging—"How-to" guide and critical reflection. *Insights Imaging* **2020**, *11*, 1–16. [CrossRef]
21. Liu, Z.; Wang, S.; Dong, D.; Wei, J.; Fang, C.; Zhou, X.; Sun, K.; Li, L.; Li, B.; Wang, M.; et al. The Applications of Radiomics in Precision Diagnosis and Treatment of Oncology: Opportunities and Challenges. *Theranostics* **2019**, *9*, 1303–1322. [CrossRef] [PubMed]
22. Bera, K.; Velcheti, V.; Madabhushi, A. Novel Quantitative Imaging for Predicting Response to Therapy: Techniques and Clinical Applications. *Am. Soc. Clin. Oncol. Educ. Book* **2018**, *38*, 1008–1018. [CrossRef] [PubMed]

23. Aerts, H.J.; Velazquez, E.R.; Leijenaar, R.T.H.; Parmar, C.; Grossmann, P.; Carvalho, S.; Bussink, J.; Monshouwer, R.; Haibe-Kains, B.; Rietveld, D.; et al. Decoding tumour phenotype by noninvasive imaging using a quantitative radiomics approach. *Nat. Commun.* **2014**, *5*, 4006. [CrossRef] [PubMed]
24. Forghani, R.; Savadjiev, P.; Chatterjee, A.; Muthukrishnan, N.; Reinhold, C.; Forghani, B. Radiomics and Artificial Intelligence for Biomarker and Prediction Model Development in Oncology. *Comput. Struct. Biotechnol. J.* **2019**, *17*, 995–1008. [CrossRef] [PubMed]
25. Lin, F.; Cui, E.-M.; Lei, Y.; Luo, L. CT-based machine learning model to predict the Fuhrman nuclear grade of clear cell renal cell carcinoma. *Abdom. Radiol.* **2019**, *44*, 2528–2534. [CrossRef] [PubMed]
26. Ding, J.; Xing, Z.; Jiang, Z.; Chen, J.; Pan, L.; Qiu, J.; Xing, W. CT-based radiomic model predicts high grade of clear cell renal cell carcinoma. *Eur. J. Radiol.* **2018**, *103*, 51–56. [CrossRef] [PubMed]
27. Shu, J.; Tang, Y.; Cui, J.; Yang, R.; Meng, X.; Cai, Z.; Zhang, J.; Xu, W.; Wen, D.; Yin, H. Clear cell renal cell carcinoma: CT-based radiomics features for the prediction of Fuhrman grade. *Eur. J. Radiol.* **2018**, *109*, 8–12. [CrossRef]
28. Li, Q.; Liu, Y.; Dong, D.; Bai, X.; Huang, Q.; Guo, A.; Ye, H.; Tian, J.; Wang, H.-Y. Multiparametric MRI Radiomic Model for Preoperative Predicting WHO / ISUP Nuclear Grade of Clear Cell Renal Cell Carcinoma. *J. Magn. Reson. Imaging* **2020**, *52*, 1557–1566. [CrossRef]
29. Zhou, H.; Mao, H.; Dong, D.; Fang, M.; Gu, D.; Liu, X.; Xu, M.; Yang, S.; Zou, J.; Yin, R.; et al. Development and External Validation of Radiomics Approach for Nuclear Grading in Clear Cell Renal Cell Carcinoma. *Ann. Surg. Oncol.* **2020**, *27*, 4057–4065. [CrossRef]
30. Feng, Z.; Shen, Q.; Li, Y.; Hu, Z. CT texture analysis: A potential tool for predicting the Fuhrman grade of clear-cell renal carcinoma. *Cancer Imaging* **2019**, *19*, 1–7. [CrossRef]
31. Han, D.; Yu, Y.; Yu, N.; Dang, S.; Wu, H.; Jialiang, R.; He, T. Prediction models for clear cell renal cell carcinoma ISUP/WHO grade: Comparison between CT radiomics and conventional contrast-enhanced CT. *Br. J. Radiol.* **2020**, *93*, 20200131. [CrossRef] [PubMed]
32. Huhdanpaa, H.; Hwang, D.; Cen, S.Y.; Quinn, B.; Nayyar, M.; Zhang, X.; Chen, F.; Desai, B.; Liang, G.; Gill, I.S.; et al. CT prediction of the Fuhrman grade of clear cell renal cell carcinoma (RCC): Towards the development of computer-assisted diagnostic method. *Abdom. Imaging* **2015**, *40*, 3168–3174. [CrossRef] [PubMed]
33. Koo, T.K.; Li, M.Y. A Guideline of Selecting and Reporting Intraclass Correlation Coefficients for Reliability Research. *J. Chiropr. Med.* **2016**, *15*, 155–163. [CrossRef] [PubMed]
34. Zou, G. Sample size formulas for estimating intraclass correlation coefficients with precision and assurance. *Stat. Med.* **2012**, *31*, 3972–3981. [CrossRef] [PubMed]
35. Yen, M.; Lo, L.-H. Examining Test-Retest Reliability. *Nurs. Res.* **2002**, *51*, 59–62. [CrossRef] [PubMed]
36. Arimura, H.; Soufi, M.; Ninomiya, K.; Kamezawa, H.; Yamada, M. Potentials of radiomics for cancer diagnosis and treatment in comparison with computer-aided diagnosis. *Radiol. Phys. Technol.* **2018**, *11*, 365–374. [CrossRef] [PubMed]
37. Kumar, V.; Gu, Y.; Basu, S.; Berglund, A.; Eschrich, S.A.; Schabath, M.B.; Forster, K.; Aerts, H.J.; Dekker, A.; Fenstermacher, D.; et al. Radiomics: The process and the challenges. *Magn. Reson. Imaging* **2012**, *30*, 1234–1248. [CrossRef]
38. Lambin, P.; Leijenaar, R.T.; Deist, T.M.; Peerlings, J.; De Jong, E.E.; Van Timmeren, J.; Sanduleanu, S.; LaRue, R.T.H.M.; Even, A.J.; Jochems, A.; et al. Radiomics: The bridge between medical imaging and personalized medicine. *Nat. Rev. Clin. Oncol.* **2017**, *14*, 749–762. [CrossRef]
39. Shinagare, A.B.; Krajewski, K.M.; Braschi-Amirfarzan, M.; Ramaiya, N.H. Advanced Renal Cell Carcinoma: Role of the Radiologist in the Era of Precision Medicine. *Radiology* **2017**, *284*, 333–351. [CrossRef]
40. Dong, X.; Xing, L.; Wu, P.; Fu, Z.; Wan, H.; Li, D.; Yin, Y.; Sun, X.; Yu, J. Three-dimensional positron emission tomography image texture analysis of esophageal squamous cell carcinoma. *Nucl. Med. Commun.* **2013**, *34*, 40–46. [CrossRef]
41. Mu, W.; Chen, Z.; Liang, Y.; Shen, W.; Yang, F.; Dai, R.; Wu, N.; Tian, J. Staging of cervical cancer based on tumor heterogeneity characterized by texture features on18F-FDG PET images. *Phys. Med. Biol.* **2015**, *60*, 5123–5139. [CrossRef] [PubMed]
42. Petresc, B.; Lebovici, A.; Caraiani, C.; Feier, D.S.; Graur, F.; Buruian, M.M. Pre-Treatment T2-WI Based Radiomics Features for Prediction of Locally Advanced Rectal Cancer Non-Response to Neoadjuvant Chemoradiotherapy: A Preliminary Study. *Cancers* **2020**, *12*, 1894. [CrossRef] [PubMed]
43. Ganeshan, B.; Abaleke, S.; Young, R.C.; Chatwin, C.R.; Miles, K.A. Texture analysis of non-small cell lung cancer on unenhanced computed tomography: Initial evidence for a relationship with tumour glucose metabolism and stage. *Cancer Imaging* **2010**, *10*, 137–143. [CrossRef] [PubMed]
44. Lang, H.; Lindner, V.; De Fromont, M.; Molinié, V.; Letourneux, H.; Meyer, N.; Martin, M.; Jacqmin, D. Multicenter determination of optimal interobserver agreement using the Fuhrman grading system for renal cell carcinoma. *Cancer* **2005**, *103*, 625–629. [CrossRef] [PubMed]
45. Letourneux, H.; Lindner, V.; Lang, H.; Massfelder, T.; Meyer, N.; Saussine, C.; Jacqmin, D. Reproductibilité du grade nucléaire de Fuhrman. Avantages d'un regroupement en deux grades (Reproducibility of Fuhrman nuclear grade: Advantages of a two-grade system). *Prog. Urol.* **2006**, *16*, 281–285. [PubMed]
46. Al-Aynati, M.; Chen, V.; Salama, S.; Shuhaibar, H.; Treleaven, D.; Vincic, L. Interobserver and intraobserver variability using the Fuhrman grading system for renal cell carcinoma. *Arch. Pathol. Lab. Med.* **2003**, *127*, 593–596. [PubMed]

47. Bektaş, S.; Bahadir, B.; Kandemir, N.O.; Barut, F.; Gul, A.E.; Ozdamar, S.O. Intraobserver and Interobserver Variability of Fuhrman and Modified Fuhrman Grading Systems for Conventional Renal Cell Carcinoma. *Kaohsiung J. Med Sci.* **2009**, *25*, 596–600. [CrossRef]
48. Cui, E.; Li, Z.; Ma, C.; Li, Q.; Lei, Y.; Lan, Y.; Yu, J.; Zhou, Z.; Li, R.; Long, W.; et al. Predicting the ISUP grade of clear cell renal cell carcinoma with multiparametric MR and multiphase CT radiomics. *Eur. Radiol.* **2020**, *30*, 2912–2921. [CrossRef]
49. He, X.; Zhang, H.; Zhang, T.; Han, F.; Song, B. Predictive models composed by radiomic features extracted from multi-detector computed tomography images for predicting low-and high-grade clear cell renal cell carcinoma: A STARD-compliant article. *Medicine* **2019**. [CrossRef]
50. Shu, J.; Wen, D.; Xi, Y.; Xia, Y.; Cai, Z.; Xu, W.; Meng, X.; Liu, B.; Yin, H. Clear cell renal cell carcinoma: Machine learning-based computed tomography radiomics analysis for the prediction of WHO/ISUP grade. *Eur. J. Radiol.* **2019**, *121*, 108738. [CrossRef]
51. Sun, X.; Liu, L.; Xu, K.; Li, W.; Huo, Z.; Liu, H.; Shen, T.; Pan, F.; Jiang, Y.; Zhang, M. Prediction of ISUP grading of clear cell renal cell carcinoma using support vector machine model based on CT images. *Medicine* **2019**, *98*, e15022. [CrossRef] [PubMed]
52. Yip, S.S.F.; Aerts, H.J.W.L. Applications and limitations of radiomics. *Phys. Med. Biol.* **2016**, *61*, R150–R166. [CrossRef] [PubMed]
53. Lubner, M.G. Radiomics and Artificial Intelligence for Renal Mass Characterization. *Radiol. Clin. North Am.* **2020**, *58*, 995–1008. [CrossRef] [PubMed]
54. Yoshida, R.; Yoshizako, T.; Hisatoshi, A.; Mori, H.; Tamaki, Y.; Ishikawa, N.; Kitagaki, H. The additional utility of apparent diffusion coefficient values of clear-cell renal cell carcinoma for predicting metastasis during clinical staging. *Acta Radiol. Open* **2017**, *6*. [CrossRef] [PubMed]
55. Rosenkrantz, A.B.; Niver, B.E.; Fitzgerald, E.F.; Babb, J.S.; Chandarana, H.; Melamed, J. Utility of the Apparent Diffusion Coefficient for Distinguishing Clear Cell Renal Cell Carcinoma of Low and High Nuclear Grade. *Am. J. Roentgenol.* **2010**, *195*, W344–W351. [CrossRef]
56. Maruyama, M.; Yoshizako, T.; Uchida, K.; Araki, H.; Tamaki, Y.; Ishikawa, N.; Shiina, H.; Kitagaki, H. Comparison of utility of tumor size and apparent diffusion coefficient for differentiation of low- and high-grade clear-cell renal cell carcinoma. *Acta Radiol.* **2015**, *56*, 250–256. [CrossRef] [PubMed]
57. Larsen, K.; Petersen, J.H.; Budtz-Jørgensen, E.; Endahl, L. Interpreting Parameters in the Logistic Regression Model with Random Effects. *Biometrics* **2000**, *56*, 909–914. [CrossRef]
58. Bektas, C.T.; Kocak, B.; Yardimci, A.H.; Turkcanoglu, M.H.; Yucetas, U.; Koca, S.B.; Erdim, C.; Kilickesmez, O. Clear Cell Renal Cell Carcinoma: Machine Learning-Based Quantitative Computed Tomography Texture Analysis for Prediction of Fuhrman Nuclear Grade. *Eur. Radiol.* **2019**, *29*, 1153–1163. [CrossRef]
59. Nazari, M.; Shiri, I.; Hajianfar, G.; Oveisi, N.; Abdollahi, H.; Deevband, M.R.; Oveisi, M.; Zaidi, H. Noninvasive Fuhrman grading of clear cell renal cell carcinoma using computed tomography radiomic features and machine learning. *Radiol. Med.* **2020**, *125*, 754–762. [CrossRef]
60. Xu, K.; Liu, L.; Li, W.; Sun, X.; Shen, T.; Pan, F.; Jiang, Y.; Guo, Y.; Ding, L.; Zhang, M. CT-Based Radiomics Signature for Preoperative Prediction of Coagulative Necrosis in Clear Cell Renal Cell Carcinoma. *Korean J. Radiol.* **2020**, *21*, 670–683. [CrossRef]
61. Frank, I.; Blute, M.L.; Cheville, J.C.; Lohse, C.M.; Weaver, A.L.; Zincke, H. An outcome prediction model for patients with clear cell renal cell carcinoma treated with radical nephrectomy based on tumor stage, size, grade and necrosis: The SSIGN score. *J. Urol.* **2002**, *168*, 2395–2400. [CrossRef]
62. Klatte, T.; Patard, J.-J.; De Martino, M.; Bensalah, K.; Verhoest, G.; De La Taille, A.; Abbou, C.-C.; Allhoff, E.P.; Carrieri, G.; Riggs, S.B.; et al. Tumor Size Does Not Predict Risk of Metastatic Disease or Prognosis of Small Renal Cell Carcinomas. *J. Urol.* **2008**, *179*, 1719–1726. [CrossRef] [PubMed]
63. Motzer, R.J.; Jonasch, E.; Agarwal, N.; Bhayani, S.; Bro, W.P.; Chang, S.S.; Choueiri, T.K.; Costello, B.A.; Derweesh, I.H.; Fishman, M.; et al. Kidney Cancer, Version 2.2017, NCCN Clinical Practice Guidelines in Oncology. *J. Natl. Compr. Cancer Netw.* **2017**, *15*, 804–834. [CrossRef] [PubMed]

Journal of
Personalized Medicine

Article

Ultrasonography in the Differentiation of Endometriomas from Hemorrhagic Ovarian Cysts: The Role of Texture Analysis

Roxana-Adelina Ștefan [1,2,†], Paul-Andrei Ștefan [3,4,*,†], Carmen Mihaela Mihu [1,4], Csaba Csutak [4,5], Carmen Stanca Melincovici [1,4], Carmen Bianca Crivii [3], Andrei Mihai Maluțan [2,6], Liviu Hîțu [7] and Andrei Lebovici [4,5]

[1] Histology, Morphological Sciences Department, "Iuliu Hațieganu" University of Medicine and Pharmacy, Louis Pasteur Street, Number 4, 400349 Cluj-Napoca, Romania; roxanalupean92@gmail.com (R.-A.Ș.); carmenmihu@umfcluj.ro (C.M.M.); carmen.melincovici@umfcluj.ro (C.S.M.)
[2] Obstetrics and Gynecology Clinic "Dominic Stanca", County Emergency Hospital, 21 Decembrie 1989 Boulevard, Number 55, 400094 Cluj-Napoca, Romania; amalutan@umfcluj.ro
[3] Anatomy and Embryology, Morphological Sciences Department, "Iuliu Hațieganu" University of Medicine and Pharmacy, Victor Babes, Street, Number 8, 400012 Cluj-Napoca, Romania; bianca.crivii@umfcluj.ro
[4] Radiology and Imaging Department, County Emergency Hospital, Cluj-Napoca, Clinicilor Street, Number 5, 400006 Cluj-Napoca, Romania; csutakcsaba@yahoo.com (C.C.); andrei1079@yahoo.com (A.L.)
[5] Radiology, Surgical Specialties Department, "Iuliu Hațieganu" University of Medicine and Pharmacy, Clinicilor Street, Number 3-5, 400006 Cluj-Napoca, Romania
[6] Obstetrics and Gynecology Clinic II, Mother and Child Department, "Iuliu Hațieganu" University of Medicine and Pharmacy, 21 Decembrie 1989 Boulevard, Number 55, 400094 Cluj-Napoca, Romania
[7] Doctoral School, Iuliu Hațieganu University of Medicine and Pharmacy, 400012 Cluj-Napoca, Romania; Liviu.Hitu@umfcluj.ro
* Correspondence: stefan.paul@umfcluj.ro or stefan_paul@ymail.com
† Authors contributed equally to this work.

Citation: Ștefan, R.-A.; Ștefan, P.-A.; Mihu, C.M.; Csutak, C.; Melincovici, C.S.; Crivii, C.B.; Maluțan, A.M.; Hîțu, L.; Lebovici, A. Ultrasonography in the Differentiation of Endometriomas from Hemorrhagic Ovarian Cysts: The Role of Texture Analysis. *J. Pers. Med.* **2021**, *11*, 611. https://doi.org/10.3390/jpm11070611

Academic Editor:
Anastasia Prodromidou

Received: 1 June 2021
Accepted: 25 June 2021
Published: 28 June 2021

Abstract: The ultrasonographic (US) features of endometriomas and hemorrhagic ovarian cysts (HOCs) are often overlapping. With the emergence of new computer-aided diagnosis techniques, this is the first study to investigate whether texture analysis (TA) could improve the discrimination between the two lesions in comparison with classic US evaluation. Fifty-six ovarian cysts (endometriomas, 30; HOCs, 26) were retrospectively included. Four classic US features of endometriomas (low-level internal echoes, perceptible walls, no solid components, and less than five locules) and 275 texture parameters were assessed for every lesion, and the ability to identify endometriomas was evaluated through univariate, multivariate, and receiver operating characteristics analyses. The sensitivity (Se) and specificity (Sp) were calculated with 95% confidence intervals (CIs). The texture model, consisting of seven independent predictors (five variations of difference of variance, image contrast, and the 10th percentile; 100% Se and 100% Sp), was able to outperform the ultrasound model composed of three independent features (low-level internal echoes, perceptible walls, and less than five locules; 74.19% Se and 84.62% Sp) in the diagnosis of endometriomas. The TA showed statistically significant differences between the groups and high diagnostic value, but it remains unclear if the textures reflect the intrinsic histological characteristics of the two lesions.

Keywords: computer-aided diagnosis; endometrioma; hemorrhagic cyst; ultrasonography; texture analysis

1. Introduction

Transvaginal ultrasonography (TVUS) is the primary diagnostic modality in investigating endometriomas. Usually, this technique can provide enough information for adequate preoperative planning [1]. However, endometriomas share some imaging features with functional hemorrhagic ovarian cysts (HOCs) [2]. Correctly distinguishing the two lesions is vital not only to avoid unnecessary surgery [3] but also because endometriomas are a sign of the presence of other endometriotic lesions at the pelvic and intestinal levels, which can cause a series of complications [4]. As a result, the imaging distinction between the two lesions strongly impacts the course of both medical and surgical treatment [5].

Since it was first described more than 25 years ago [6], the classic "ground glass" appearance of endometriomas has been constantly reevaluated; because of this, researchers have assigned it different levels of diagnostic utility [7–10] and even integrated it into decision trees, along with other ultrasonographic, clinical, and biological parameters [11]. The ultrasound (US) appearance of endometriomas is highly variable, being influenced by the time-lapse of blood degradation [12]. Moreover, the US features of endometriomas overlap with other lesions such as dermoids, cystic adnexal lesions complicated by bleeding, and cystic ovarian neoplasms [13]. Often, endometriomas and HOCs are indistinguishable, especially in the early stages [2], as they share the characteristic of a cystic mass with bloody content [14]. For these reasons, recent studies [15] concluded that only 60% of endometriomas larger than 2 cm can be appropriately diagnosed with US.

Furthermore, the variety of ultrasound-based descriptors and scoring systems may cause confusion, particularly because their parameters are changeable, sophisticated, and frequently of arbitrary importance [16,17]. Furthermore, the interpretation of medical images is always subjective and observer-dependent [18].

Computer-aided discrimination (CAD) systems have emerged in recent years and attempt to overcome these limitations and increase confidence in the US detection and characterization of ovarian masses [19]. Some of the recently developed CAD techniques focus on the US identification of ovarian malignancies [20–24] and mostly rely on texture analysis (TA) to autonomously detect the presence of a disease based on grayscale variations within TVUS images [25]. TA is a method for extracting and processing parameters that describe pixel intensity and variation patterns, resulting in a quantitative and comprehensive representation of image content [26,27]. The basic concept of texture analysis of ultrasound images is that a diseased process that affects the tissue produces an altered signal, which gives textural features different values than those of the normal structure [28].

This is the first study to provide an ultrasound-based texture characterization of endometriomas and HOCs. We investigated whether texture parameters could be used as an objective diagnostic criterion for distinguishing between the two lesions and whether these parameters were able to outperform the classic US features.

2. Materials and Methods

2.1. Study Group

This Health Insurance Portability and Accountability Act–compliant, a single-institution, retrospective pilot study, was approved by the institutional review board, and informed consent was waived because of its retrospective nature. From September 2017 to March 2019, a keyword search (using the terms "hemorrhagic + cyst", alternatives and combinations) in the imaging database of our institution was conducted to identify TVUS images corresponding to ovarian cystic lesions. The keyword search resulted in 235 image reports. Each report was analyzed by one researcher, who excluded all studies that referred to previously documented ovarian malignant or benign tumors (other than endometriomas) ($n = 57$), lesions that were described as having features strongly suggesting malignancy ($n = 31$), and lesions that measured less than 2 cm ($n = 28$). The medical records of the remaining 119 patients were retrieved from the archive of our healthcare institution and investigated for disease-related data. Further, all patients that were transferred to another institution ($n = 19$) and all lesions that were not removed and did not undergo histopathological analysis were also excluded ($n = 33$). The US examinations of the remaining 67 patients were reviewed by one gynecologist who selected only B-mode images that were not affected by artifacts or technique errors. After applying these criteria, US images from 30 endometriomas and 26 hemorrhagic cysts were selected.

2.2. Reference Standard

All included lesions underwent pathological analysis after surgical removal. For endometriomas, 12 lesions were removed and analyzed, along with subsequent diseases (uterine fibromatosis, $n = 9$; adenomyosis, $n = 3$). All HOCs underwent pathological analysis because they were included in the surgical specimen analyzed for another condition (atypical endometrial hyperplasia, $n = 1$; adnexal torsion, $n = 2$; uterine leiomyosarcoma, $n = 2$; mucinous cystadenoma, $n = 2$; cystadenofibroma, $n = 3$; serous ovarian carcinoma, $n = 3$; serous cystadenomas, $n = 3$; ovarian teratoma, $n = 4$; uterine fibromatosis, $n = 6$).

For pathological analysis, a solution of 10% buffered formalin was used to fixate the surgical samples overnight. Further, using tissue processors, the samples were embedded in paraffin according to the standard protocol of the pathological anatomy laboratory of our institution. The resulting samples were sectioned at 5 µm and stained with hematoxylin and eosin. All resulting samples underwent examination by a pathologist with 9 years of experience in gynecological disease. Following the analysis workflow, a final diagnosis was possible in all the included cases.

2.3. Image Acquisition and Interpretation

All the included images were acquired by four gynecologists with at least 8 years of experience in gynecological ultrasound. All examinations were performed on the same machine (Aplio 300, Toshiba Medical Systems, Tokyo, Japan) using a dedicated endovaginal probe (4–10 MHz).

In the first step of image interpretation, each examination was reviewed by one researcher (R.A.Ș.) who was aware of the patients' pathological findings, clinical outcomes, and final diagnoses. The medical data were cross-referenced with the images to ensure the selection of only the lesions that underwent pathological analysis. Respective lesions were marked, and only one image that was considered representative from each examination was retrieved and anonymized.

In the second step, the typical greyscale US characteristics of endometriomas ("a cyst with internal homogeneous low-level echoes, a perceptible . . . , no solid component, and a maximum of five locules for multilocular lesions"), as described by Collins et al. [12], were quantified using anonymized images by another researcher (A.M.M.) who was also blinded to the patients' outcomes. The homogeneous low-level echoes (or ground glass) appearance was considered if this was the dominant pattern in more than 90% of the lesion's content. The lesions were considered to have a wall if a structure at least 2 mm thick that surrounded at least 50% of the visible portion of the cyst could be observed. Since only gray-scale images were retrieved, any structure that was adjacent to the walls was considered a solid component (including hyperechoic foci, papillary projections, and retracting clots). Furthermore, unilocular lesions were also considered to have a maximum of five locules.

2.4. Statistical Analysis

To quantify the information in a quantitative way, for each lesion, each ultrasound parameter was given the value of "1" if present or "0" if absent. A multiple regression (multivariate) analysis was conducted to investigate which ultrasound features could independently predict the presence of endometriomas. The analysis was conducted using the "enter" input model, which involved entering all variables into the model in one single step. A conventional p-value of less than 0.05 was used to determine the corresponding independent variables that contributed significantly to the differentiation of endometriomas from HOCs, whereas variables with a p-value of more than 0.01 were omitted. In addition, the coefficient of determination (R^2, the proportion of the variation in the dependent variable explained by the regression model, measuring of the goodness of fit of the model), the R^2-adjusted coefficient (the coefficient of determination adjusted for the number of independent variables in the regression model), the multiple correlation coefficient (measuring how tightly the data points clustered around the regression plane, calculated by taking the square root of the coefficient of determination), and the variance inflation factor (VIF, an indicator of multicollinearity) were calculated. After the analysis, the predicted values were saved and then used in a receiver operating characteristic (ROC) analysis to determine the prediction model's ability to identify endometriomas. The ROC analysis was also used to test the ability of each ultrasound feature in the diagnosis of endometriomas. The DeLong et al. technique was used to compute the ROC curves, and the binomial exact confidence intervals for the areas under the curve (AUC) were stated. The optimal cut-off values for predicting patients with malignancies were determined using a common optimization step that maximized the Youden index (J). Specificity (Sp) and sensitivity (Se) were calculated from the same data, without other adjustments, using a 95% confidence interval (CI).

2.5. Texture Analysis Protocol

The radiomics approach consisted of five steps: image pre-processing, lesion segmentation, feature extraction, feature selection, and prediction.

2.5.1. Image Pre-Processing and Segmentation

Images were retrieved in Digital Imaging and Communications in Medicine (DICOM) format and were further converted into Joint Photographic Experts Group format (JPG) and imported into a dedicated software (Topaz DeNoise AI, Topaz Labs, TX, USA) in which the negative impact of the speckle noise was reduced using a denoising technique based on convolutional neural networks [29]. Afterward, images were reconverted into bitmap format and transferred to a dedicated texture analysis software (MaZda, Institute of Electronics, Technical University of Lodz, Lodz, Poland) [30]. Using this program, the image grey levels were normalized based on the mean and three standard deviations of grey level intensities to reduce the contrast and brightness variations.

The image segmentation process was performed by a second researcher (P.A.Ș.) who was blinded to the outcomes of the patients. The researcher incorporated each lesion into a two-dimensional region of interest (ROI). The first step of the ROI definition process was performed semi-automatically. The researcher drew a circle inside each lesion and the software automatically delineated the structure of interest based on gradient and geometry coordinates. In the second step, if a complete overlap between the ROI and the structure's contours was detected, the ROI was manually adjusted (Figure 1).

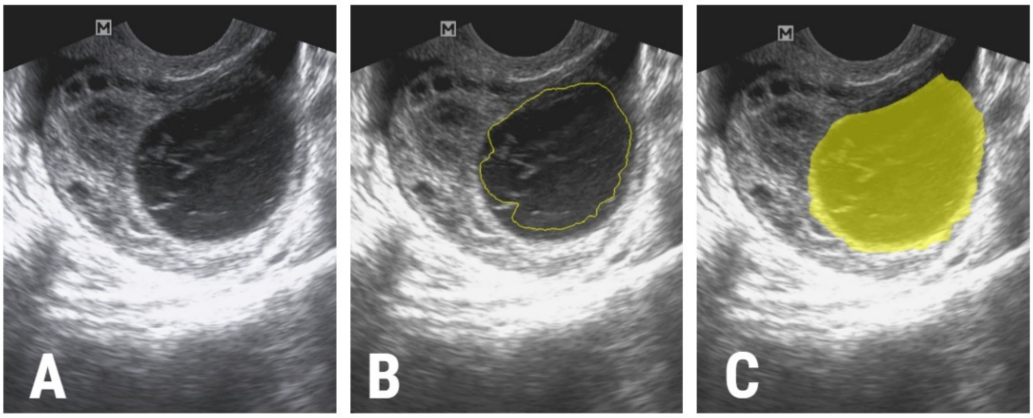

Figure 1. (**A**) The ultrasound image of a 29-year-old patient with s histologically proven hemorrhagic ovarian cyst, (**B**) the initial ROI that was automatically delineated by the software (yellow line), and (**C**) the final ROI after manual adjustments (yellow).

2.5.2. Feature Extraction

The texture features (or parameters) were automatically extracted by the software after the definition and positioning of each ROI. From each lesion, a total of 275 parameters were computed [31]. The parameters are described in Table 1.

Table 1. Texture parameters.

Class	Parameters	Computation	Variations	Number of Parameters
Histogram	Mean, Variance, Skewness, Kurtosis, Perc.01–99%	-	-	5
Absolute gradient	GrMean, GrVariance, GrSkewness, GrKurtosis, GrNonZeros, percentage of pixels with nonzero gradient	4 bits/pixel	-	5
Run Length Matrix	RLNonUni, GLevNonU, LngREmph, ShrtREmp, Fraction	6 bits/pixel	4 directions	20
Co-occurrence Matrix	AngScMom, Contrast, Correlat, SumOfSqs, InvDfMom, SumAverg, SumVarnc, SumEntrp, Entropy, DifVarnc, DifEntrp	6 bits/pixel; 5 between-pixel distances	4 directions	220
Auto-regressive Model	Teta 1–4, Sigma	-	-	5
Wavelet transformation	WavEn	5 scales	4 frequency bands	20

Mean, histogram's mean; Variance, histogram's variance; Skewness, histogram's skewness; Kurtosis, histogram's kurtosis; Perc.01–99%, 1st to 99th percentile; GrMean, absolute gradient mean; GrVariance, absolute gradient variance; GrSkewness, absolute gradient skewness; GrKurtosis, absolute gradient kurtosis; GrNonZeros, percentage of pixels with nonzero gradient); RLNonUni, run-length nonuniformity; GLevNonU, grey level nonuniformity; LngREmph, long-run emphasis; ShrtREmp, short-run emphasis; Fraction, the fraction of image in runs; AngScMom, angular second moment; Contrast, contrast; Correlat, correlation; SumOfSqs, the sum of squares; InvDfMom, inverse difference moment; SumAverg, sum average; SumVarnc, sum variance; SumEntrp, sum entropy; Entropy, entropy; DifVarnc, difference of variance; DifEntrp, difference of entropy; Teta 1–4, parameters $\theta 1$–$\theta 4$; Sigma, parameter σ; WavEn, wavelet energy.

For each lesion, the segmentation and extraction of texture parameters were repeated 1 week apart, and the process was carried out by the same researcher. The resulting values were used to evaluate the intra-reader agreement using the intraclass coefficient.

2.5.3. Feature Selection

In order to identify the best-suited texture parameters for differentiating between the two histopathological groups, three methods were applied successively. The first step comprised of applying three reduction methods (based on mutual information (MI), Fisher coefficients (F, the ratio of between-class to within-class variance), and the probability of classification error and average correlation coefficients (POE + ACC)) [32]. Each of the three selection methods provided a set of ten unique parameters.

Second, the intraclass correlation coefficient (ICC) was calculated using the absolute agreement between the same rater for the all-subjects model, and average values along with the 95% confidence interval were reported. Features that demonstrated an ICC of below 0.85 were excluded from further analysis.

Third, the absolute values of the remaining parameters were compared between the two groups using the Mann–Whitney U test. The statistically significant level was set at a *p*-value of below 0.0016 after Bonferroni correction (which implied dividing the classic 0.05 level by 30, considering the 27 unique parameters that resulted after applying the reduction techniques as well as age and the two separate histopathological entities). All texture parameters that showed univariate analysis results below this threshold were excluded from further processing.

2.5.4. Class Prediction

To investigate which of the previously selected texture features were independent predictors of endometriomas, a multiple regression analysis was performed following the same computational method as was used for the ultrasound features. Furthermore, features with a VIF greater than 10^4 were withdrawn from further testing because a high VIF value indicates multicollinearity. The predicted values were saved and then used in an ROC analysis to determine the prediction model's ability to identify endometriomas.

The ROC analysis was also used to test the diagnostic utility of the features that were independently associated with endometriomas, following the same workflow as described for the ultrasound features. Statistical analysis was performed using a commercially available dedicated software, MedCalc version 14.8.1 (MedCalc Software, Mariakerke, Belgium). The workflow model is summarized in Figure 2.

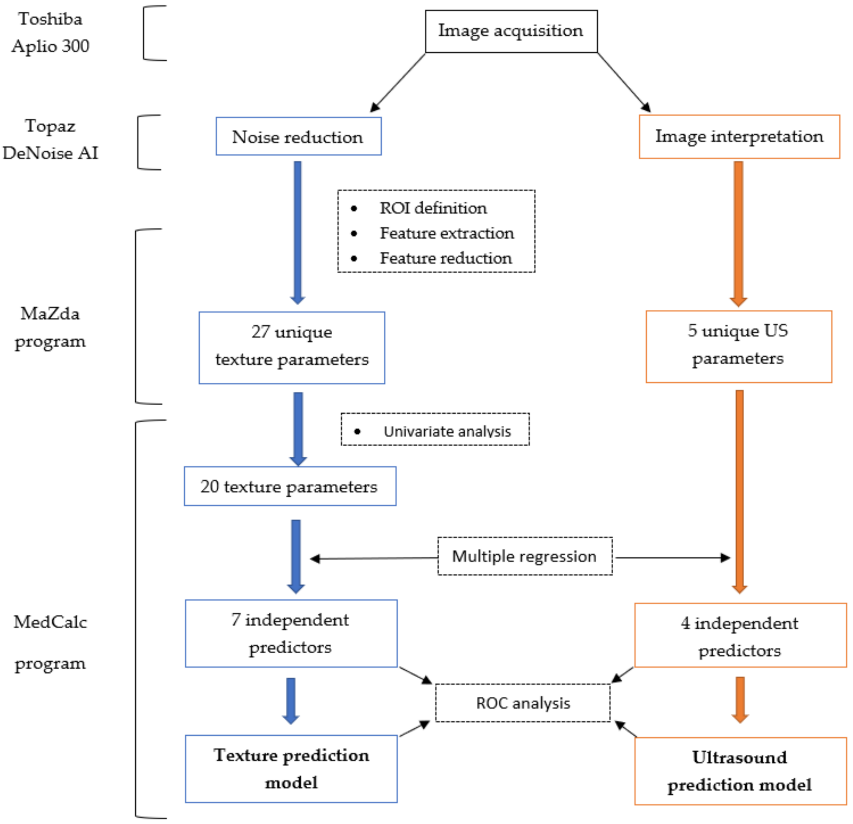

Figure 2. Workflow model summarizing the construction of the texture (blue) and ultrasound (orange) prediction models. US, ultrasound; ROI, region of interest; ROC, receiver operating characteristic.

3. Results

Fifty-six patients (average age ± standard deviation: 38.27 ± 14.68 years; age range: 22–54 years) were included according to their final diagnosis. Patients were divided into an endometrioma group ($n = 30$) and an HOC group ($n = 26$).

When analyzing the gray-scale features, three out of four characteristics (internal homogeneous low-level echoes, a perceptible wall, and a maximum of five locules) were independently associated with endometriomas (Table 2). The multivariate analysis showed a significance level of $p < 0.0001$, an R^2 coefficient of determination of 0.3856, an adjusted R^2 value of 0.3384, and a multiple correlation coefficient of 0.621. The diagnostic performance of the three independent US features and the prediction model is displayed in Table 3.

For the texture analysis, one variation of the difference of variance parameter (CN5D6-DifVarnc) was selected by both the Fisher and POE + ACC methods, while two variations of the same feature (CN4D6DifVarnc and CH5D6DifVarnc) were highlighted by both the Fisher and MI methods. In total, 27 unique parameters resulted after applying the three reduction techniques. The results of the univariate analysis and intra-reader agreement evaluation are displayed in Table 4.

Table 2. The multivariate analysis showing independent features associated with the presence of endometriomas. The cases in which a specific feature could be found in either group are displayed as number/total.

Parameter	Endometriomas	HOCs	Coefficient	Standard Error	*p*-Value	VIF
Internal homogeneous low-level echoes	23/30	7/26	0.3151	0.1177	**0.0099**	1.178
Perceptible wall	17/30	8/26	−0.4162	0.1557	**0.01**	1.197
No solid component	12/30	6/26	0.1977	0.1234	0.1153	1.123
Maximum of 5 locules	21/30	26/26	0.2971	0.1167	**0.0139**	1.144

Bold values are statistically significant ($p < 0.05$). VIF, variance inflation factor.

Table 3. The receiver operating characteristic analysis results of the prediction model and the ultrasound parameters that were independently associated with endometriomas.

US Feature	AUC	Sign.lvl.	J	Cut-Off	Se (%)	Sp (%)
Internal homogeneous low-level echoes	0.736 (0.603–0.844)	**0.0001**	0.47	>0	74.19 (55.4–88.1)	73.08 (52.2–88.4)
Perceptible wall	0.62 (0.482–0.746)	0.0631	0.24	>0	54.84 (36–72.7)	69.23 (48.2–85.7)
Maximum of 5 locules	0.661 (0.524–0.781)	**0.0002**	0.32	≤0	32.26 (16.7–51.4)	100 (86.8–100)
US prediction model	0.857 (0.739–0.936)	**<0.0001**	0.58	>0.42	74.19 (55.4–88.1)	84.62 (65.1–95.6)

The values corresponding to 95% confidence intervals are shown in parentheses. Bold values are statistically significant. US, ultrasound; US prediction model, the model composed of the predictive values provided by the multivariate analysis of ultrasound features; Sign.lvl., significance level; J, Youden index; Se, sensitivity; Sp, specificity.

Table 4. The univariate analysis (Mann–Whitney U test) and the intra-reader agreement evaluation results.

Parameter	*p*-Value	Endometriomas		Hemorrhagic Cysts		Agreement	
		Median	IQR	Median	IQR	ICC	95% CI
Fisher							
CN5D6DifVarnc	**0.0001**	8.33	4.73–14.81	22.85	18.94–32.58	0.98	0.97–0.99
CN4D6DifVarnc	**0.0002**	7.95	3.95–14.7	20.79	18.27–30.62	0.98	0.98–0.99
CV5D6DifVarnc	**0.0002**	7.77	4.28–15.01	23.61	16.32–28.37	0.98	0.97–0.99
CZ5D6DifVarnc	**0.0002**	8.37	4.75–15.55	23.25	16.6–30.34	0.98	0.97–0.99
CN3D6DifVarnc	**0.0002**	7.04	3.61–14.55	20.82	15.5–28.04	0.93	0.98–0.99
CV4D6DifVarnc	**0.0003**	7.43	3.71–14.88	22.12	15.46–26.6	0.99	0.98–0.99
CZ4D6DifVarnc	**0.0004**	7.81	4.49–15.16	22.67	15.14–27.66	0.99	0.98–0.99
CH5D6DifVarnc	**0.0006**	7.03	3.63–14.39	22.11	13.52–27.51	0.99	0.99–0.99
CZ3D6DifVarnc	**0.0005**	7.38	3.95–14.6	21.67	13.97–25.14	0.99	0.98–0.99
WavEnHL_s-2	**0.0008**	10.65	5.33–20.82	29.68	16.84–38.2	0.99	0.99–0.99
POE + ACC							
RZD6Fraction	0.0445	0.74	0.7–0.8	0.67	0.43–0.76	0.99	0.98–0.99
RVD6GLevNonU	**0.0006**	2849.65	1420.58–3750.88	1081.5	575.26–1718.42	0.99	0.99–0.99
WavEnHL_s-5	0.007	30.72	22.22–61.06	69.11	47.55–124.11	0.99	0.99–0.99
RVD6LngREmph	0.0103	2.27	1.78–2.69	5.67	2.35–37.05	0.98	0.97–0.99

Table 4. *Cont.*

Parameter	p-Value	Endometriomas		Hemorrhagic Cysts		Agreement	
		Median	IQR	Median	IQR	ICC	95% CI
ATeta4	0.5085	0.15	0.01–0.38	0.16	0.12–0.31	0.99	0.99–0.99
GD4Kurtosis	0.2783	10.59	0.1–67.8	48.14	28.16–58.71	0.99	0.98–0.99
Perc10	**0.0005**	31.5	24–39	4	1–19	0.99	0.99–0.99
CN5D6Correlat	0.0569	0.57	0.5–0.71	0.45	0.25–0.59	0.98	0.96–0.98
RZD6GLevNonU	**0.0009**	3041.64	1300.63–3769.19	1079.18	559.01–1829.93	0.99	0.99–0.99
Mutual Information							
WavEnHH_s-3	0.0011	8.46	3.95–10.79	15.6	9.8–19.88	0.99	0.98–0.99
CN3D6Contrast	**0.0005**	15.81	7.45–19.29	28.84	22.47–37.86	0.99	0.98–0.99
WavEnLH_s-3	**0.0008**	23.73	17.75–30.86	46.16	30.64–60.69	0.97	0.94–0.98
WavEnHH_s-4	0.0055	7.18	5.42–12.16	13.69	11.17–17.1003	0.96	0.94–0.98
CH4D6DifVarnc	**0.0009**	6.18	3.2–14.51	20.33	12.47–24.73	0.99	0.99–0.99
CV5D6Contrast	**0.0007**	16.91	9.03–21.58	33.39	23.8–40.08	0.98	0.97–0.99
CN4D6Contrast	**0.0005**	17.49	8.44–21.16	31.49	23.18–39.65	0.98	0.97–0.99
CH4D6Contrast	0.0033	13.22	6.17–17.78	26.23	16.25–33.47	0.99	0.99–0.99

Statistically significant results from the Mann—Whitney U-test are highlighted in bold. IQR, interquartile range; POE + ACC, probability of classification error and average correlation coefficient; ICC, intraclass coefficient; DifVarnc, difference of variance; WavEn, wavelet energy; Fraction, the fraction of image in runs; GLevNonU, grey level nonuniformity; GLevNonU, long-run emphasis; Teta, parameter θ4; Kurtosis, histogram's kurtosis; Perc10, 10th percentile; Correlat, correlation; Contrast, contrast.

Twenty parameters showed statistically significant results in the univariate analysis and underwent multiple regression analysis. The parameter CN4D6DifVarnc was excluded from the analysis because it had a VIF greater than 10^4. The multivariate analysis showed a significance level of $p < 0.001$, an R^2 coefficient of determination of 0.435, an adjusted R^2 value of 0.427, and a multiple correlation coefficient of 0.634. The multiple regression analysis identified seven parameters as independent predictors of endometriomas (Table 5).

Table 5. Multivariate analysis results showing the texture parameters independently associated with the presence of endometriomas.

Parameter	Coefficient	Standard Error	p-Value	VIF
CH4D6DifVarnc	0.2662	0.1931	0.1808	2965.650
CH5D6DifVarnc	−0.2735	0.1944	0.1722	3131.661
CN3D6DifVarnc	−0.04859	0.2082	0.8174	3440.996
CN5D6DifVarnc	0.4225	0.1255	**0.0026**	1425.172
CV4D6DifVarnc	0.01293	0.2247	0.9546	4143.205
CV5D6DifVarnc	−0.5476	0.1931	**0.0091**	3225.142
CZ3D6DifVarnc	−0.4053	0.1928	**0.0462**	3080.372
CZ4D6DifVarnc	1.0179	0.2813	**0.0014**	6825.702
CZ5D6DifVarnc	−0.4797	0.1352	**0.0016**	1621.315
CN3D6Contrast	0.2624	0.1357	0.0651	2136.581
CN4D6Contrast	−0.4877	0.1945	**0.0193**	5009.060
CV5D6Contrast	0.2167	0.1179	0.0784	1795.666

Table 5. *Cont.*

Parameter	Coefficient	Standard Error	*p*-Value	VIF
Perc10	0.01755	0.004113	**0.0003**	3.535
RVD6GLevNonU	0.0002	0.0002	0.4101	123.113
RZD6GLevNonU	−0.0001	0.0002	0.6515	125.807
WavEnHH_s_3	0.01052	0.02963	0.7255	29.482
WavEnHL_s_2	0.017	0.01602	0.2993	37.886
WavEnLH_s_3	0.008	0.006074	0.1791	7.886

Bold values are statistically significant ($p < 0.05$). VIF, variance inflation factor.

The ROC analysis showed that the prediction model exceeded the individual diagnostic ability of all independent features in terms of both sensitivity and specificity (Table 6, Figure 3). The texture maps that display the distribution of selected texture features in images from each entity are shown in Figure 4.

Table 6. The receiver operating characteristic analysis results of the prediction model and the texture parameters that were independently associated with endometriomas.

Parameter	AUC	Sign.lvl.	J	Cut-Off	Se (%)	Sp (%)
CN5D6DifVarnc	0.882 (0.747–0.960)	**<0.0001**	0.7128	≤16.73	86.67 (69.3–96.2)	84.62 (54.6–98.1)
CV5D6DifVarnc	0.856 (0.716–0.944)	**<0.0001**	0.659	≤21.26	96.67 (82.8–99.9)	69.23 (38.6–90.9)
CZ3D6DifVarnc	0.838 (0.694–0.933)	**0.0001**	0.659	≤20.12	96.67 (82.8–99.9)	69.23 (38.6–90.9)
CZ4D6DifVarnc	0.841 (0.697–0.934)	**0.0001**	0.625	≤19.43	93.33 (77.9–99.2)	69.23 (38.6–90.9)
CZ5D6DifVarnc	0.859 (0.719–0.946)	**<0.0001**	0.6462	≤15.67	80 (61.4–92.3)	84.62 (54.6–98.1)
CN4D6Contrast	0.838 (0.694–0.933)	**<0.0001**	0.6897	≤21.16	76.67 (57.7–90.1)	92.31 (64–99.8)
Perc10	0.836 (0.691–0.931)	**<0.0001**	0.6462	>19	80 (61.4–92.3)	84.62 (54.6–98.1)
Texture prediction model	1 (0.918–1)	**<0.0001**	1	>0.4	100 (88.4–100)	100 (75.3–100)

The values corresponding to 95% confidence intervals are shown in parentheses. Bold values are statistically significant. Texture prediction model, the model composed of the predictive values provided by the multivariate analysis of the texture features; Sign.lvl., significance level; J, Youden index; Se, sensitivity; Sp, specificity.

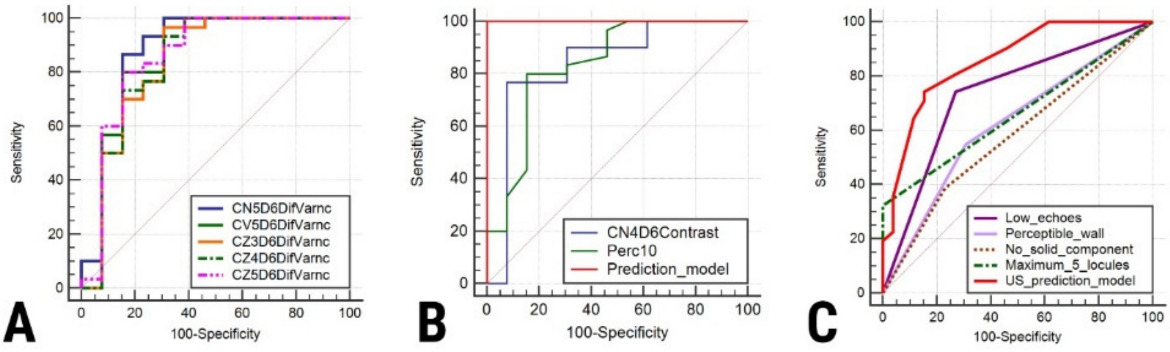

Figure 3. Comparison of areas under the curve for the differentiation of endometriomas from hemorrhagic cysts based on (**A**) the difference of variance parameters, (**B**) contrast and percentile parameters and the prediction model composed of independent texture parameters, and (**C**) classic ultrasound features of endometriomas and their combined diagnostic value.

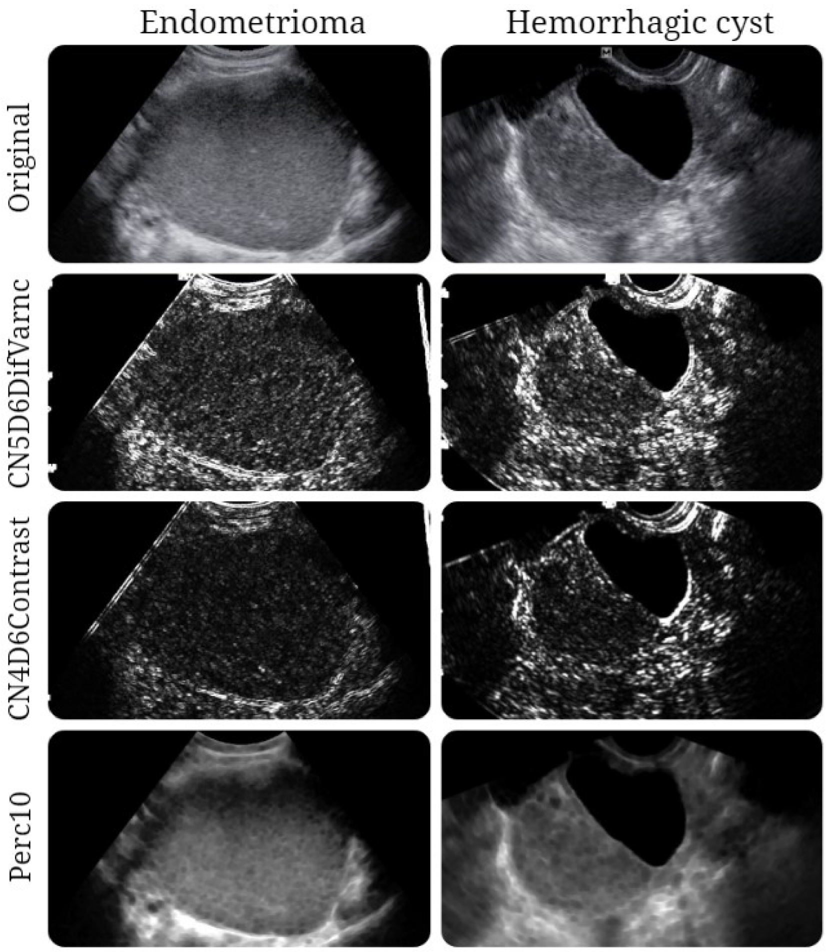

Figure 4. Texture maps showing the distribution of three texture parameters (CN5D6DifVarnc, CN4D6Contrast, and Perc10) in images of patients with a histologically proven endometrioma and hemorrhagic ovarian cyst.

4. Discussion

Our results showed that the majority of the included endometriomas (n = 23) expressed low-level internal echoes, while this indicator was encountered in less than 30% of HOCs (n = 7). As expected, this feature was the most distinctive sign of endometriomas, as previously described since the first research was conducted in the field (Table 7). However, we were unable to find a study that specifically aimed to address the distinction between endometriomas and HOCs based on grey-level ultrasound features, with most research focusing on distinguishing endometriomas from other ovarian tumors (sometimes including HOCs) [7,11]. In our study, the low-level internal echoes (or ground glass appearance) showed similar sensitivity (74.19%) but lower specificity for the diagnosis of endometriomas compared with the most recent research in the field (73% Se; 94% Sp) [11]. Moreover, when other features were added to the model, the overall sensitivity did not increase.

Hemorrhagic ovarian cysts are caused by bleeding inside functional cysts that are spontaneously resorbed [2]. They also progress slowly through different stages of acute hemorrhage, clot development, and retraction, resulting in a shifting sonographic appearance until they fully resolve in 6 weeks or shrink significantly in size [33]. In the early stages, they appear as solid masses with thin walls. Furthermore, their content may express variable echogenicity with reticular strands. When the clot retracts, its attachment to the wall can mimic a papillary projection, and a fluid layer also develops within the cyst [34].

At the beginning of their formation, the US appearance of endometriomas can be indistinguishable from that of HOCs. In time, as the bleeding becomes chronic, endometriomas build up more hemorrhagic debris [2], which is responsible for their classic US appearance (of a "unilocular cyst with fluid content expressing ground glass echogenicity" or "ground glass") [35,36]. However, further research [11] demonstrated that less than 50% of endometriomas exhibit these characteristics, with even lower rates in the postmenopausal population. This is most likely because endometriomas express cyclic bleeding, which results in different time stages of blood degradation, thereby generating variable US appearance [37].

Table 7. Research involving endometriomas' classic ultrasound features.

Imaging Feature	Author/Year	Diagnostic Value
Low-level internal echoes	Patel et al. (1999) [7]	95% Se; 49% Sp
Low-level internal echoes, no neoplastic features, and no fibrinous strands or retracting clots	Patel et al. (1999) [7]	65% Se; 76% Sp
Low-level internal echoes, no neoplastic features, and no hyperechoic wall foci	Patel et al. (1999) [7]	30% Se; 86% Sp
Low-level internal echoes, no neoplastic features, and hyperechoic wall foci or multilocularity	Patel et al. (1999) [7]	45% Se; 90% Sp
"Round, intraovarian, homogeneous, hypoechoic tissue, with a clear demarcation from the parenchyma and without papillary proliferations"	Mais et al. (1993) [6]	84% Se; 90% Sp
"A cystic structure with low, homogeneous echogenicity and a thick cystic wall with regular margins" but not excluding "very fine papillary structures, not exceeding 3 mm"	Volpi et al. (1995) [8]	82.4% Se; 97.7% Sp
"The presence of a round-shaped homogeneoushypoechoic mass of low-level echoes"	Alcazar et al. (1997) [9]	88.9% Se; 91% Sp
"Round-shaped homogeneous hypoechoic 'tissue' of low-level echoes within the ovary"	Guerriero et al. (1996) [10]	79% Se; 76% Sp
Ground glass echogenicity of cyst fluid	Van Holsbeke et al. (2010) [11]	73% Se; 94% Sp

Se, sensitivity; Sp, specificity.

In practice, the grayscale imaging of endometriomas and HOCs can be identical due to bleeding features of different ages, making distinction difficult [2]. On one hand, sonographic observation of fibrin strands and/or retracting clots within an adnexal cyst reflects a recent episode of hemorrhage [35]. Due to the cyclic bleeding characteristic of endometriomas, the appearance of fibrin stands can easily mimic the features of an HOC [38]. On the other hand, HOCs can also demonstrate diffuse low-level internal echoes [7], most likely because in some cases, they do not regress and instead accumulate various quantities of intracellular deoxyhemoglobin and methemoglobin [39].

Considering the information above, together with the subjective nature of the interpretation of US images, a clear differentiation between the two lesion types can be performed only through microscopic evaluation [40]. The cell population found within endometriomas consists of degenerate erythrocytes, hemosiderin-laden macrophages, and endometrial and epithelial cells [41–44]. Functional hemorrhagic cysts' content is composed of a mixture of blood products along with plasma proteins, mucopolysaccharides, and hyaluronic acid [45], and these lesions also have rich cellularity [43]. It is possible that all the histopathological characteristics are reflected within US images, subtly influencing the pixel intensity and distribution, which may be detected and quantified through texture parameters.

Our results showed that five variations of the difference of variance parameter were independent predictors of endometriomas (CN5D6DifVarnc, CV5D6DifVarnc, CZ3D6DifVarnc, CZ4D6DifVarnc, and CZ5D6DifVarnc). The variance is a measure of contrast severity, which can be used to create descriptors of relative smoothness. [46]. The difference of variance measures the variance of the difference of grey level values (reflecting the randomness within an image [47,48]. In all scenarios, this feature exhibited higher values for HOCs than for endometriomas.

The contrast parameter shows the local variations present in an image, expressing higher values when an image contains a large number of pixels with different grey level values [47]. We obtained higher values for the HOCs than for endometriomas.

The first-order histogram parameters (mean, standard deviation, variance, skewness, kurtosis, and percentiles) reflect the value of the pixel intensity, without considering the spatial relations between the pixels [49]. The percentile number (n) is the point in the histogram where n% of the pixel values are found to the left [50]. A percentile, in other words, is the highest grey level value at which a given percentage of the pixels in an image are contained [51]. This signifies that 10% of the pixels within images were distributed under higher values for endometriomas than for HOCs.

Although it was expected that endometriomas would show a higher degree of echogenic randomness because of the multitude of contained elements, the parameters indicating these characteristics showed higher values for HOCs. This observation is in accordance with the literature, which indicates that HOCs have more complex and heterogenous content on TVUS (probably because they more often express fine linear strands and retracting clots) [52].

In the current study, the texture model was able to diagnose endometriomas with almost perfect rates: 100% Se (CI, 88.4–100%) and 100% Sp (CI, 75.3–100%). In a similar study, based on magnetic resonance (MRI) images [53], the texture model was able to distinguish endometriomas from HOCs with similar rates, showing a sensitivity of 100% (CI, 85.8–100%) and a specificity of 100% (CI, 71.5–100%). Once again, this model [53] outperformed the classic MRI features of endometriomas ("T2 shading", 75.86% Se and 35.71% Sp and "T2 dark spots", 55.17% Se and 64.29% Sp). However, the current model comprised different texture parameters (five variations of difference of variance, image contrast, and 10th percentile) compared to those extracted from MRI images (which included mostly variations of entropy) [53]. The high accuracy rates accomplished by both models could indicate that TA is feasible in distinguishing the two lesions in both types of imaging examinations. However, these excellent results may be influenced by the reduction techniques (especially the Fisher method); although they provide the most distinguishing parameters, these parameters are highly correlated [32], and they could therefore influence the diagnostic value of the prediction model [54]. In order to at least partially counteract this effect, in addition to the Fisher method, two other selection methods were used that did not provide parameters with a high degree of correlation (POE + ACC and Mutual Information). Moreover, parameters that showed statistical significance in the univariate analysis but also demonstrated a VIF $>10^4$ were excluded from the final model.

Because the ultrasound features of the two lesions may overlap, sometimes the diagnosis cannot be straightforward. Our TA model may be useful in providing more confidence in the diagnosis of a newly discovered bleeding ovarian lesion. Moreover, if this approach is further validated, it could offer an alternative to more expensive and time-consuming approaches for characterizing adnexal lesions, such as MRI examinations. However, the role of MRI in the characterization of endometriomas will not be diminished since some lesions could remain inapparent to TVUS despite the visualization of the ovaries because of their location or the presence of periovarian adhesions [55].

Our study had several limitations. Due to the retrospective design and the decision to include only pathologically proven lesions, the study may possess selection and verification bias. In the final step of patient selection, all lesions below 2 cm ($n = 33$) were excluded. This threshold was necessary to provide a sufficient area for the software to analyze and extract the pixel pattern. Therefore, the study population was relatively low. The small population was also due to the limited time approved for this research by the ethics committee and the strict exclusion and inclusion criteria. The menstrual phase, CA-125 levels, and menopausal status were not reported since they were inconsistently mentioned in the retrieved medical data. Few of the selected patients had Doppler images stored in our database; therefore, only grey scale images were selected. For this reason, other classic features of endometriomas, such as no internal vascularity and avascular internal nodules [12], could not be quantified. However, the use of color Doppler imaging does not improve the diagnostic accuracy of transvaginal ultrasonography alone in the diagnosis of ovarian endometrioma [56]. On the other hand, it is documented that the presence of intracystic vascularization poses doubts about malignancy [57]. However, this was not the case for selected lesions, as the pathological analysis did not raise suspicions of malignancy in any case. A limitation was that one investigator was aware of the final diagnoses of the lesions. However, since many patients had several adnexal lesions at the time of the US evaluation, this strategy was necessary for selecting only documented lesions. This researcher was not involved in the image segmentation, statistical analysis, or reporting of the results after this point. Considering these limitations and the pilot nature of this research, the presented TA model for discriminating endometriomas from HOCs requires prospective research for both validation and establishment of its clinical utility compared with the classic imaging methods.

5. Conclusions

We demonstrated a statistically significant difference between the texture features of endometriomas and hemorrhagic ovarian cysts. Although this approach outperformed the classic ultrasound evaluation, it remains unclear if textures reflect the lesions' pathological characteristics. Further studies are required to identify the exact substrate that determines textural differentiation.

Author Contributions: Conceptualization, R.-A.Ș.; data curation, C.C.; formal analysis, C.S.M., A.M.M. and L.H.: investigation, P.-A.Ș., C.S.M., C.B.C., A.M.M. and L.H.; methodology, R.-A.Ș., C.M.M. and C.C.; project administration, A.L.; resources, C.S.M.; software, L.H.; supervision, A.L.; validation, C.B.C. and A.L.; visualization, P.-A.Ș. and C.C.; writing–original draft, R.-A.Ș. and P.-A.Ș.; writing–review & editing, C.B.C. and C.M.M. All authors have read and agreed to the published version of the manuscript.

Funding: This project was co-financed by the Human Capital Operational Program 2014–2020, project no. POCU/380/6/13/125171.

Institutional Review Board Statement: The study was conducted according to the guidelines of the Declaration of Helsinki and approved by the Ethics Committee of the Iuliu Hațieganu University of Medicine and Pharmacy Cluj-Napoca (protocol code: 52; date of approval: 11 March 2019).

Informed Consent Statement: Patient consent was waived due to the retrospective nature of the study.

Acknowledgments: This paper was published under the framework of the European Social Fund, Human Capital Operational Programme 2014–2020, project no. POCU/380/6/13/125171.

Conflicts of Interest: The authors declare no conflicts of interest. The funders had no role in the design of the study; in the collection, analyses, or interpretation of data; in the writing of the manuscript; or in the decision to publish the results.

References

1. Bosch, T.V.D.; Van Schoubroeck, D. Ultrasound diagnosis of endometriosis and adenomyosis: State of the art. *Best Pract. Res. Clin. Obstet. Gynaecol.* **2018**, *51*, 16–24. [CrossRef]
2. Batur, A.; Yavuz, A.; Ozgokce, M.; Bora, A.; Bulut, M.D.; Arslan, H.; Alpaslan, M. The utility of ultrasound elastography in differentiation of endometriomas and hemorrhagic ovarian cysts. *J. Med. Ultrason.* **2016**, *43*, 395–400. [CrossRef]

3. Kim, H.-J.; Lee, S.-Y.; Shin, Y.R.; Park, C.S.; Kim, K. The Value of Diffusion-Weighted Imaging in the Differential Diagnosis of Ovarian Lesions: A Meta-Analysis. *PLoS ONE* **2016**, *11*, e0149465. [CrossRef] [PubMed]
4. Redwine, D.B. Ovarian endometriosis: A marker for more extensive pelvic and intestinal disease. *Fertil. Steril.* **1999**, *72*, 310–315. [CrossRef]
5. Tanase, Y.; Kawaguchi, R.; Takahama, J.; Kobayashi, H. Factors that Differentiate between Endometriosis-associated Ovarian Cancer and Benign Ovarian Endometriosis with Mural Nodules. *Magn. Reson. Med. Sci.* **2018**, *17*, 231–237. [CrossRef]
6. Mais, V.; Guerriero, S.; Ajossa, S.; Angiolucci, M.; Paoletti, A.M.; Melis, G.B. The efficiency of transvaginal ultrasonography in the diagnosis of endometrioma. *Fertil. Steril.* **1993**, *60*, 776–780. [CrossRef]
7. Patel, M.D.; Feldstein, V.A.; Chen, D.C.; Lipson, S.D.; Filly, R.A. Endometriomas: Diagnostic Performance of US. *Radiology* **1999**, *210*, 739–745. [CrossRef] [PubMed]
8. Volpi, E.; De Grandis, T.; Zuccaro, G.; La Vista, A.; Sismondi, P. Role of transvaginal sonography in the detection of endometriomata. *J. Clin. Ultrasound* **1995**, *23*, 163–167. [CrossRef]
9. Alcázar, J.L.; Laparte, C.; Jurado, M.; Lopez-Garcia, G. The role of transvaginal ultrasonography combined with color velocity imaging and pulsed Doppler in the diagnosis of endometrioma. *Fertil. Steril.* **1997**, *67*, 487–491. [CrossRef]
10. Guerriero, S.; Mais, V.; Ajossa, S.; Paoletti, A.M.; Angiolucci, M.; Melis, G.B. Transvaginal ultrasonography combined with CA-125 plasma levels in the diagnosis of endometrioma. *Fertil. Steril.* **1996**, *65*, 293–298. [CrossRef]
11. Van Holsbeke, C.; Van Calster, B.; Guerriero, S.; Savelli, L.; Paladini, D.; Lissoni, A.A.; Czekierdowski, A.; Fischerová, D.; Zhang, J.; Mestdagh, G.; et al. Endometriomas: Their ultrasound characteristics. *Ultrasound Obstet. Gynecol.* **2010**, *35*, 730–740. [CrossRef] [PubMed]
12. Collins, B.G.; Ankola, A.; Gola, S.; McGillen, K.L. Transvaginal US of Endometriosis: Looking Beyond the Endometrioma with a Dedicated Protocol. *Radiographics* **2019**, *39*, 1549–1568. [CrossRef] [PubMed]
13. Bennett, G.L.; Slywotzky, C.M.; Cantera, M.; Hecht, E.M. Unusual Manifestations and Complications of Endometriosis—Spectrum of Imaging Findings: Pictorial Review. *Am. J. Roentgenol.* **2010**, *194*, WS34–WS46. [CrossRef]
14. Athey, P.; Diment, D.D. The spectrum of sonographic findings in endometriomas. *J. Ultrasound Med.* **1989**, *8*, 487–491. [CrossRef]
15. Asch, E.; Levine, D. Variations in appearance of endometriomas. *J. Ultrasound Med.* **2007**, *26*, 993–1002. [CrossRef]
16. Gramellini, D.; Fieni, S.; Sanapo, L.; Casilla, G.; Verrotti, C.; Nardelli, G.B. Diagnostic accuracy of IOTA ultrasound morphology in the hands of less experienced sonographers. *Aust. N. Z. J. Obstet. Gynaecol.* **2008**, *48*, 195–201. [CrossRef] [PubMed]
17. Timmerman, D. Lack of standardization in gynecological ultrasonography. *Ultrasound Obstet. Gynecol.* **2000**, *16*, 395–398. [CrossRef] [PubMed]
18. Guerriero, S.; Ajossa, S.; Garau, N.; Piras, B.; Paoletti, A.M.; Melis, G.B. Ultrasonography and color Doppler-based triage for adnexal masses to provide the most appropriate surgical approach. *Am. J. Obstet. Gynecol.* **2005**, *192*, 401–406. [CrossRef] [PubMed]
19. Acharya, U.R.; Molinari, F.; Sree, S.V.; Swapna, G.; Saba, L.; Guerriero, S.; Suri, J.S. Ovarian Tissue Characterization in Ultrasound. *Technol. Cancer Res. Treat.* **2015**, *14*, 251–261. [CrossRef]
20. Ștefan, P.-A.; Lupean, R.-A.; Mihu, C.; Lebovici, A.; Oancea, M.; Hîțu, L.; Duma, D.; Csutak, C. Ultrasonography in the Diagnosis of Adnexal Lesions: The Role of Texture Analysis. *Diagnostics* **2021**, *11*, 812. [CrossRef]
21. Acharya, U.R.; Sree, S.V.; Krishnan, M.M.R.; Saba, L.; Molinari, F.; Guerriero, S.; Suri, J.S. Ovarian tumor characterization using 3D ultrasound. *Technol. Cancer Res. Treat.* **2012**, *11*, 543–552. [CrossRef] [PubMed]
22. Acharya, U.R.; Mookiah, M.R.K.; Sree, S.V.; Yanti, R.; Martis, R.J.; Saba, L.; Molinari, F.; Guerriero, S.; Suri, J.S. Evolutionary Algorithm-Based Classifier Parameter Tuning for Automatic Ovarian Cancer Tissue Characterization and Classification. *Ultraschall Med.* **2012**, *35*, 237–245. [CrossRef]
23. Acharya, U.R.; Sree, S.V.; Saba, L.; Molinari, F.; Guerriero, S.; Suri, J.S. Ovarian Tumor Characterization and Classification Using Ultrasound—A New Online Paradigm. *J. Digit. Imaging* **2012**, *26*, 544–553. [CrossRef]
24. Khazendar, S.; Sayasneh, A.; Al-Assam, H.; Du, H.; Kaijser, J.; Ferrara, L.; Timmerman, D.; Jassim, S.; Bourne, T. Automated characterization of ultrasound images of ovarian tumours: The diagnostic accuracy of a support vector machine and image processing with a local binary pattern operator. *Facts Views Vis. ObGyn* **2015**, *7*, 7–15. [PubMed]
25. Acharya, U.R.; Sree, S.V.; Kulshreshtha, S.; Molinari, F.; Koh, J.E.W.; Saba, L.; Suri, J.S. GyneScan: An Improved Online Paradigm for Screening of Ovarian Cancer via Tissue Characterization. *Technol. Cancer Res. Treat.* **2014**, *13*, 529–539. [CrossRef] [PubMed]
26. Gadkari, D. Image Quality Analysis Using GLCM. Master's Thesis, University of Central Florida, Orlando, FL, USA, 2004.
27. Larroza, A.; Bodí, V.; Moratal, D. Texture Analysis in Magnetic Resonance Imaging: Review and Considerations for Future Applications. In *Assessment of Cellular and Organ Function and Dysfunction Using Direct and Derived MRI Methodologies*; IntechOpen: London, UK, 2016.
28. Morris, D. An evaluation of the use of texture measurements for the tissue characterization of ultrasonic images of in vivo human placentae. *Ultrasound Med. Biol.* **1988**, *14*, 387–395. [CrossRef]
29. Liu, Z.; Yan, W.Q.; Yang, M.L. Image denoising based on a CNN model. In Proceedings of the 4th International Conference on Control, Automation and Robotics (ICCAR), Auckland, New Zealand, 20–23 April 2018; pp. 389–393.
30. Strzelecki, M.; Szczypinski, P.; Materka, A.; Klepaczko, A. A software tool for automatic classification and segmentation of 2D/3D medical images. *Nucl. Instrum. Methods Phys. Res. Sect. A* **2013**, *702*, 137–140. [CrossRef]
31. MaZda. Available online: http://www.eletel.p.lodz.pl/programy/mazda/index.php?action=docs (accessed on 26 May 2021).

32. Mayerhoefer, M.E.; Breitenseher, M.; Amann, G.; Dominkus, M. Are signal intensity and homogeneity useful parameters for distinguishing between benign and malignant soft tissue masses on MR images? Objective evaluation by means of texture analysis. *Magn. Reson. Imaging* **2008**, *26*, 1316–1322. [CrossRef]
33. Jain, K.A. Sonographic Spectrum of Hemorrhagic Ovarian Cysts. *J. Ultrasound Med.* **2002**, *21*, 879–886. [CrossRef]
34. Untrasonography in the Evaluation of Adnexae. Available online: https://www.glowm.com/pdf/Ultrasound_in_obstetrics_and_gynecology-chapter12.pdf (accessed on 26 May 2021).
35. Jain, K. Prospective evaluation of adnexal masses with endovaginal gray-scale and duplex and color Doppler US: Correlation with pathologic findings. *Radiology* **1994**, *191*, 63–67. [CrossRef]
36. Sayasneh, A.; Ekechi, C.; Ferrara, L.; Kaijser, J.; Stalder, C.; Sur, S.; Timmerman, D.; Bourne, T. The characteristic ultrasound features of specific types of ovarian pathology (Review). *Int. J. Oncol.* **2014**, *46*, 445–458. [CrossRef]
37. Guerriero, S.; Saba, L.; Pascual, M.A.; Ajossa, S.; Rodriguez, I.; Mais, V.; Alcazar, J.L. Transvaginal ultrasound vs magnetic resonance imaging for diagnosing deep infiltrating endometriosis: Systematic review and meta-analysis. *Ultrasound Obstet. Gynecol.* **2018**, *51*, 586–595. [CrossRef]
38. Patel, M.D.; Feldstein, V.A.; Filly, R.A. The Likelihood Ratio of Sonographic Findings for the Diagnosis of Hemorrhagic Ovarian Cysts. *J. Ultrasound Med.* **2005**, *24*, 607–614. [CrossRef]
39. Kanso, H.N.; Hachem, K.; Aoun, N.J.; Atallah, D.; Buy, J.-N.; Ghossain, M.A.; Haddad-Zebouni, S.; Klein-Tomb, L. Variable MR findings in ovarian functional hemorrhagic cysts. *J. Magn. Reson. Imaging* **2006**, *24*, 356–361. [CrossRef] [PubMed]
40. Damario, M.A.; Rock, J.A. Classification and Staging of Endometriosis. In *Endometriosis: Advanced Management and Surgical Techniques*; Nezhat, C.R., Berger, G.S., Nezhat, F.R., Buttram, V.C., Nezhat, C.H., Eds.; Springer: New York, NY, USA, 1995; pp. 27–36.
41. Mulvany, N.J. Aspiration Cytology of Ovarian Cysts and Cystic Neoplasms. *Acta Cytol.* **1996**, *40*, 911–920. [CrossRef] [PubMed]
42. Greenebaum, E. Aspirating Nonneoplastic Ovarian Cysts: Rationale, Technique, and Controversy. *Lab. Med.* **1996**, *27*, 462–467. [CrossRef]
43. Russel, P. Surface Epithelial—Stromal Tumors of the Ovary. In *Blaustein's Pathology of the Female Genital Tract*, 4th ed.; Kurman, R.J., Ed.; Springer: New York, NY, USA, 1994; pp. 705–782.
44. Wood, D.; Fitzpatrick, T.; Bibbo, M. Peritoneal Washings and Ovary. In *Comprehensive Cytopathology*; Wilbur, D., Ed.; Elsevier: Amsterdam, The Netherlands, 2014; pp. 291–301.
45. Ontobee: UBERON. Available online: http://www.ontobee.org/ontology/UBERON?iri=http://purl.obolibrary.org/obo/UBERON_0000038 (accessed on 7 March 2020).
46. Armi, L.; Fekri-Ershad, S. Texture Image Analysis and Texture Classification Methods—A Review. 2019. Available online: https://arxiv.org/ftp/arxiv/papers/1904/1904.06554.pdf (accessed on 26 May 2021).
47. Biomedical Informatics 260. Computational Feature Extraction: Texture Features Lecture 6 David Paik. Available online: https://docplayer.net/188454072-Biomedical-informatics-260-computational-feature-extraction-texture-features-lecture-6-david-paik-phd-spring-2019.html (accessed on 26 May 2021).
48. Durgamahanthi, V.; Christaline, J.A.; Edward, A.S. GLCM and GLRLM Based Texture Analysis: Application to Brain Cancer Diagnosis Using Histopathology Images. In *Intelligent Computing and Applications*; Dash, S.S., Das, S., Panigrahi, B.K., Eds.; Springer: Singapore, 2020; pp. 691–706.
49. Szczypinski, P.M.; Klepaczko, A. MaZda—A Framework for Biomedical Image Texture Analysis and Data Exploration. In *Biomedical Texture Analysis: Fundamentals, Tools and Challenges*; Szczypinski, P.M., Klepaczko, A., Depeursinge, A., Al-Kadi, O.S., Mitchell, J.R., Eds.; Academic Press: Cambridge, MA, USA, 2017.
50. Huang, Y.-Q.; Liang, H.-Y.; Yang, Z.-X.; Ding, Y.; Zeng, M.-S.; Rao, S.-X. Value of MR histogram analyses for prediction of microvascular invasion of hepatocellular carcinoma. *Medicine* **2016**, *95*, e4034. [CrossRef]
51. Castellano, G.; Bonilha, L.; Li, L.; Cendes, F. Texture analysis of medical images. *Clin. Radiol.* **2004**, *59*, 1061–1069. [CrossRef]
52. Rezvani, M. In Nonneoplastic Ovarian Lesions: Endometrioma. In *Diagnostic Imaging: Gynecology*, 2nd ed.; Shaaban, A.M., Menias, C.O., Tubay, M.S., Eds.; Elsevier: Amsterdam, The Netherlands, 2015; p. 190.
53. Lupean, R.-A.; Ștefan, P.-A.; Csutak, C.; Lebovici, A.; Măluțan, A.; Buiga, R.; Melincovici, C.; Mihu, C. Differentiation of Endometriomas from Ovarian Hemorrhagic Cysts at Magnetic Resonance: The Role of Texture Analysis. *Medicina* **2020**, *56*, 487. [CrossRef] [PubMed]
54. Hassan, I.; Kotrotsou, A.; Bakhtiari, A.S.; Thomas, G.A.; Weinberg, J.S.; Kumar, A.J.; Sawaya, R.; Luedi, M.M.; Zinn, P.O.; Colen, R.R. Radiomic Texture Analysis Mapping Predicts Areas of True Functional MRI Activity. *Sci. Rep.* **2016**, *6*, 25295. [CrossRef]
55. Guerriero, S.; Mais, V.; Ajossa, S.; Paoletti, A.M.; Angiolucci, M.; Labate, F.; Melis, G.B. The role of endovaginal ultrasound in differentiating endometriomas from other ovarian cysts. *Clin. Exp. Obstet. Gynecol.* **1995**, *22*, 20–22. [PubMed]
56. Wu, M.-H.; Cheng, Y.-C.; Chang, F.-M. Ultrasonographic Assessment of Ovarian Endometrioma. *J. Med. Ultrasound* **2008**, *16*, 241–248. [CrossRef]
57. Na, K.; Park, S.Y.; Kim, H.-S. Clinicopathological Characteristics of Primary Ovarian Adenomyoma: A Single-institutional Experience. *Anticancer. Res.* **2017**, *37*, 2565–2574. [CrossRef] [PubMed]

Acta Radiologica
0(0) 1–7

DOI: 10.1177/0284185117727787
journals.sagepub.com/home/acr

Diagnostic value of apparent diffusion coefficient in differentiating between high-grade gliomas and brain metastases

Ionut Caravan[1], Cristiana Augusta Ciortea[2], Alexandra Contis[1] and Andrei Lebovici[1,2]

Abstract

Background: High-grade gliomas (HGGs) and brain metastases (BMs) can display similar imaging characteristics on conventional MRI. In HGGs, the peritumoral edema may be infiltrated by the malignant cells, which was not observed in BMs.
Purpose: To determine whether the apparent diffusion coefficient values could differentiate HGGs from BMs.
Material and Methods: Fifty-seven patients underwent conventional magnetic resonance imaging (MRI) and diffusion-weighted imaging (DWI) before treatment. The minimum and mean ADC in the enhancing tumor (ADC_{min}, ADC_{mean}) and the minimum ADC in the peritumoral region (ADC_{edema}) were measured from ADC maps. To determine whether there was a statistical difference between groups, ADC values were compared. A receiver operating characteristic (ROC) curve analysis was used to determine the cutoff ADC value for distinguishing between HGGs and BMs.
Results: The mean ADC_{min} values in the intratumoral regions of HGGs were significantly higher than those in BMs. No differences were observed between groups regarding ADC_{mean} values. The mean ADC_{min} values in the peritumoral edema of HGGs were significantly lower than those in BMs. According to ROC curve analysis, a cutoff value of $1.332 \times 10^{-3}\,mm^2/s$ for the ADC_{edema} generated the best combination of sensitivity (95%) and specificity (84%) for distinguishing between HGGs and BMs. The same value showed a sensitivity of 95.6% and a specificity of 100% for distinguishing between GBMs and BMs.
Conclusion: ADC values from DWI were found to distinguish between HGGs and solitary BMs. The peritumoral ADC values are better than the intratumoral ADC values in predicting the tumor type.

Keywords
Diffusion-weighted imaging (DWI), apparent diffusion coefficient (ADC), high-grade glioma, brain metastasis, peritumoral edema

Date received: 6 June 2017; accepted: 22 July 2017

Introduction

High-grade gliomas (HGGs) are the most common malignant brain tumors in adults (1). According to the 2007 World Health Organization (WHO) Classification of Tumors of the Central Nervous System (2), HGGs include a variety of glial tumors: WHO grade III (anaplastic astrocytoma, anaplastic oligoastrocytoma, anaplastic oligodendroglioma) and WHO grade IV (glioblastoma multiforme [GBM]). It should be mentioned that a new classification based on molecular parameters has been available since 2016, but it was not used in this study. Brain metastases (BMs) affect 20–30% of patients with cancer. The most common primary cancers that metastasize to the brain are lung, breast, melanoma, and gastrointestinal cancers (3).

Magnetic resonance imaging (MRI) plays a critical role in the preoperative assessment of brain tumors.

---

[1] "Iuliu Hatieganu" University of Medicine and Pharmacy, Cluj-Napoca, Romania
[2] Department of Radiology, Emergency County Hospital, Cluj-Napoca, Romania

Corresponding author:
Cristiana Augusta Ciortea, Department of Radiology, Emergency County Hospital, Cluj-Napoca, Romania.
Email: cristianaciortea@yahoo.com

When patients present multiple lesions and there is history of a known primary tumor, the diagnosis of BM is straightforward. However, in many cases there is a solitary lesion. Thus, the differentiation of HGGs from BMs represents a common differential diagnosis problem since both tumors may display similar imaging characteristics and contrast enhancement patters on conventional MRI (4).

Diffusion-weighted imaging (DWI) findings and apparent diffusion coefficient (ADC) measurements provide additional information about the tissue microstructure. An inverse relationship was observed between ADC values and tumor cellularity (5). Previous studies had shown that ADC values can be used in differentiating between certain types of cerebral tumors: malignant and benign meningiomas; high-grade and low-grade gliomas; meningiomas and gliomas; meningiomas and metastases; and meningiomas and vestibular schwannomas (6–10). However, the usefulness of the ADC values to differentiate HGGs from BMs remains controversial.

Therefore, the purpose of this study was to determine whether the ADC values in contrast-enhancing tumors and peritumoral edema could differentiate HGGs from BMs.

Material and Methods

Patients

Institutional review board approval was obtained for this study. Images of all HGGs and BMs treated at our institution between August 2015 and December 2016 were analyzed retrospectively. Our inclusion criteria were: adult with a solitary, contrast-enhancing brain lesion, preoperatively investigated by DWI. Exclusion criteria were: no available preoperative DWI examination (n = 136); artifacts on ADC maps (n = 4); and tumors below 10 mm in diameter (n = 1). In total, 57 patients (25 men, 32 women; age range = 36–79 years; mean age = 58.3 ± 10.6 years) fulfilled the inclusion and exclusion criteria and were adopted for further analysis.

Gliomas were classified according to the 2007 WHO Classification of Tumors of the Central Nervous System (2). Out of 57 patients, WHO grade III glioma was diagnosed in five cases (four anaplastic astrocytomas and one anaplastic oligodendroglioma), WHO grade IV glioblastoma in 25 cases, and metastasis in 27 cases. Metastatic lesions included lung carcinoma (n = 12), breast carcinoma (n = 7), colorectal carcinoma (n = 3), melanoma (n = 3), sarcoma (n = 1), and renal carcinoma (n = 1).

Examination protocols

All presurgical MRI examinations were performed on 1.5-T systems with an eight-channel head coil: Siemens Magnetom Symphony Tim Upgrade (Siemens Healthineers, Erlangen, Germany) and General Electric Optima 360 (GE Healthcare, Fairfield, CT, USA). Conventional sequences, including T1-weighted (T1W) images, T2-weighted (T2W) images, FLAIR images, and contrast-enhanced T1W images were obtained. DWI was performed using a single-shot echo-planar imaging sequence with three gradient directions (b-values = 0 and 1000 s/mm^2). MRI parameters for each system are shown in Tables 1 and 2.

DWI data processing

All measurements were performed on a PACS station (KODAK/Carestream Version 10.2; Carestream Health, Rochester, NY, USA). Image interpretation was done by one radiologist (AL, nine years of experience in neuroradiology, five years of experience interpreting DWI) and a sixth-year medical student (IC, previously trained for the interpretation of DWI images and ADC maps). The investigators were unaware of the patients' clinical and pathologic information.

Table 1. Description of MRI parameters for Siemens Magnetom Symphony Tim Upgrade system.

	T1W imaging	T2W imaging	FLAIR	DWI
TR (ms)	9	3110	9000	4600
TE (ms)	2.38	92	85	105
TI (ms)	–	–	2500	–
Slice thickness (mm)	2.2	5	5	5
Field of view (mm^2)	180 × 240	180 × 240	180 × 240	230 × 230
Matrix	256 × 256	180 × 320	256 × 256	192 × 192
b-values	–	–	–	0, 1000

Table 2. Description of MRI parameters for General Electric Optima 360 system.

	T1W imaging	T2W imaging	FLAIR	DWI
TR (ms)	480	7300	9300	8900
TE (ms)	11.7	107	117	105
TI (ms)	–	–	2400	–
Slice thickness (mm)	4	4	4	4
Field of view (mm^2)	240 × 192	240 × 240	240 × 240	240 × 240
Matrix	320 × 224	384 × 384	320 × 224	128 × 128
b-values	–	–	–	0, 1000

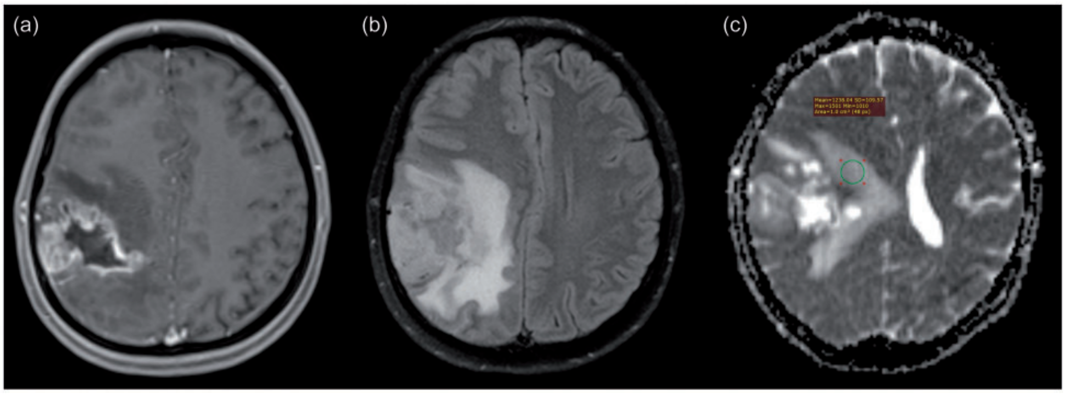

Fig. 1. GBM in the right parietal lobe of a 47-year-old woman. (a) Contrast-enhanced T1W imaging shows an inhomogeneous enhanced mass in the right parietal lobe. (b) FLAIR image shows extensive peritumoral edema. (c) On ADC map, the mass exhibits central cystic changes. The peritumoral edema shows inhomogeneous signal intensity, indicating the presence of tumor infiltration. Minimum ADC value in this case is $1.01 \times 10^{-3}\,mm^2/s$ within the peritumoral edema.

ADC maps were generated from the DWI sequence. The ADC values of each tumor were obtained by using the region of interest (ROI) analysis. First, we inspected all continuous sections that included the enhancing tumor and the peritumoral region. Then, we selected at least five sections for ROI analysis. In the intratumoral region, 5–8 ROIs were placed in the solid parts of the tumor. These ROIs were drawn to avoid hemorrhagic, cystic, and necrotic components. Their diameter was in the range of 10–120 mm^2 according to the size and morphology of each tumor. The ROI with the lowest ADC value was chosen as the minimum ADC (ADC_{min}) and an average value from multiple ROIs was chosen as the mean ADC (ADC_{mean}). The peritumoral region was defined as the area outside the margin of the solid part of the tumor. At least 2–3 ROIs ($\sim 100\,mm^2$) were placed as closely as possible to the tumoral margin using T1W post-contrast reference images. The ROI with the lowest ADC value was chosen as the minimum ADC (ADC_{edema}). If there were controversies between investigators, an average value for ADC was chosen by consensus (Figs. 1 and 2).

Statistical analysis

For statistical analysis, the GraphPad Prism software package was used (GraphPad Prism 6.0, GraphPad Software Inc., La Jolla, CA, USA). To determine whether there was a statistical difference between groups, we compared minimum and mean ADC values using the two-sided Mann–Whitney U test. A P value < 0.05 was considered statistically significant.

Furthermore, the receiver operating characteristic (ROC) curve was used to evaluate the diagnostic ability of the ADC value to differentiate between HGGs and BMs. The cutoff value was chosen to maximize the Youden index. Sensitivity, specificity, and area under the curve (AUC) were calculated.

Results

The ADC_{min}, ADC_{mean}, and ADC_{edema} values in HGGs and BMs are shown in Table 3.

The mean ADC_{min} value in the intratumoral region was significantly lower in BMs ($0.672 \pm 0.107 \times$

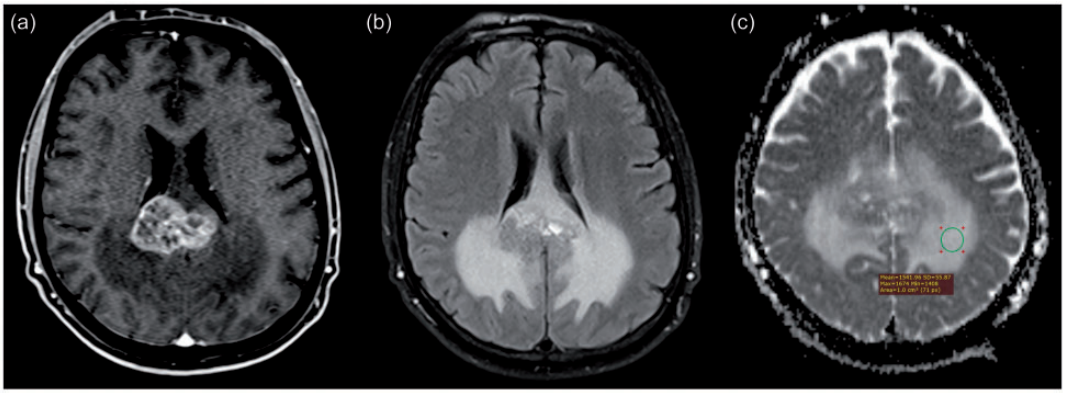

Fig. 2. Solitary metastasis derived from lung adenocarcinoma in the corpus callosum of a 57-year-old man. (a) Contrast-enhanced T1W imaging shows a well-defined mass with uneven enhancement in the right corpus callosum. (b) FLAIR image shows extensive peritumoral edema. (c) On ADC map, the mass exhibits central cystic changes. The peritumoral edema shows homogeneous signal intensity. Minimum ADC value in this case is 1.41×10^{-3} mm^2/s within the peritumoral edema.

Table 3. ADC values for gliomas and metastases.

ADC values ($\times 10^{-3}$ mm^2/s)	WHO III gliomas (n = 5)	WHO IV gliomas (n = 25)	High-grade gliomas (n = 30)	Metastases (n = 27)
ADC$_{min}$	0.706 ± 0.079	0.746 ± 0.077*	0.739 ± 0.078*	0.672 ± 0.107
ADC$_{mean}$	0.841 ± 0.063	0.869 ± 0.057	0.864 ± 0.058	0.822 ± 0.106
ADC$_{edema}$	1.468 ± 0.026	1.217 ± 0.068*	1.257 ± 0.113*	1.461 ± 0.074

*Statistical significance compared to metastases.

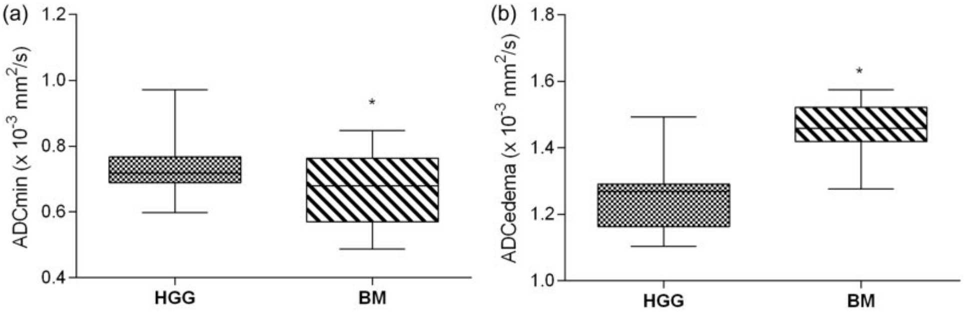

Fig. 3. Comparison of ADC values between HGGs and BMs. (a) Intratumoral ADC$_{min}$ values in BMs are significantly lower in comparison to those in HGGs ($P = 0.03$). (b) Peritumoral ADC$_{min}$ values in HGGs are significantly lower than those in BMs ($P < 0.001$). Data are expressed as mean ± standard deviation.

10^{-3} mm^2/s) in comparison with HGGs ($0.739 \pm 0.078 \times 10^{-3}$ mm^2/s; $P = 0.03$) (Fig. 3a). There were no statistical differences between the two groups regarding intratumoral ADC$_{mean}$ values ($P > 0.05$).

The mean ADC$_{min}$ value in the peritumoral edema of HGGs ($1.257 \pm 0.113 \times 10^{-3}$ mm^2/s) was significantly lower than that in BMs ($1.416 \pm 0.074 \times 10^{-3}$ mm^2/s; $P < 0.001$) (Fig. 3b).

An ADC$_{edema}$ value of less than 1.332×10^{-3} mm^2/s was determined as the threshold in differentiating between HGGs and BMs (sensitivity = 95%, specificity = 84%, Youden index = 0.79). ROC analysis showed that the AUC was 0.906 (Fig. 4a). The same value of ADC$_{edema}$ generated the best combination of sensitivity (95.6%) and specificity (100%) for distinguishing GBMs from BMs (AUC = 0.985) (Fig. 4b).

Discussion

DWI depicts the microscopic rate of water diffusion within the tissue. The lower intratumoral ADC values have been linked to increased cellularity; thus, the

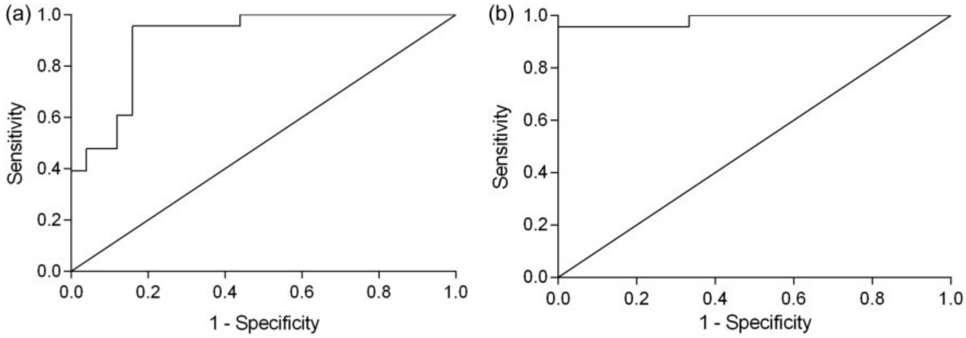

Fig. 4. ROC curve analysis of minimum ADC_{edema} values for use in differentiation of HGGs from BMs, respectively, GBMs from BMs. (a) For a cutoff value of ADC_{edema} of 1.332×10^{-3} mm²/s, the best combination of sensitivity (95%) and specificity (84%) was obtained for distinguishing HGGs and BMs (AUC = 0.906). (b) The same cutoff value of ADC_{edema} generated a sensitivity of 95.6% and a specificity of 100% for distinguishing GBMs and BMs (AUC = 0.985).

regions with minimum ADC reflect the highest tumoral density (5).

Several authors have investigated DWI ability in distinguishing between HGGs and metastatic brain tumors (11–19). Whereas some studies have shown that intratumoral ADC value is not useful to differentiate HGGs and BMs (11–16), others have reported some differences. For example, there were studies that have found higher intratumoral ADC values in BMs compared to HGGs, but they have serious limitations such as small number of patients (17,18). However, Server et al. have reported lower ADC values in BMs as compared to HGGs (19).

In the current study, we have observed lower minimum intratumoral ADC values in BMs in comparison to HGGs. Higher ADC values in the enhancing area of HGGs might be explained by the presence of microcystic degeneration, necrosis foci, and the overproduction of extracellular matrix components of glioblastoma cells (20,21). Moreover, BMs represent a heterogeneous group of tumors and their microscopic characteristics may depend on their origin. This could lead to different results in different studies. It is important to note that ADC values obtained from the enhancing lesion could be inaccurate due to the presence of various degrees of necrosis, hemorrhage, and susceptibility artifacts (15).

Vasogenic edema is frequently associated with brain tumors. There is significant escape of plasma fluid and protein to the extracellular space, due to disturbance of vascular permeability. In metastatic lesions peritumoral edema is "pure vasogenic" since there is no microscopic evidence of tumor cells outside of the contrast-enhanced margin of the lesion. HGGs are characterized by the ability to grow outside of their margins and to invade along the white matter tracts, thus peritumoral edema is better referred to as "infiltrative edema" in this case (22,23). Therefore, the key to distinguishing between HGGs and BMs could be the detection of tumor infiltration within the peritumoral edema.

Conventional MRI has limited ability in differentiation between the two types of edema since both have a high-intensity signal on T2W imaging. However, the usefulness of DWI is still controversial. Some studies reported no differences between HGGs and BMs regarding the ADC values in peritumoral edema (12,19,23). Contrary to these observations there have been other studies showing that ADC measurements in the peritumoral edema may discriminate the two types of tumors (15,16,24).

We found that minimum ADC value of peritumoral edema in HGGs was lower than that in BMs. This difference was even more pronounced between GBMs and BMs. This finding suggests there is restricted water diffusion in the edema surrounding HGGs, probably due to the neoplastic cell infiltration.

Our results are consistent with other studies. For example, Lee et al. have found lower ADC values in GBMs as compared to BMs (15). They reported a cutoff value of 1.302×10^{-3} mm²/s for distinguishing between GBMs and BMs, with a sensitivity of 83% and a specificity of 79%. Han et al. have also reported lower ADC values associated with the peritumoral edema of the HGGs than those for the peritumoral edema of BMs (16). At $b = 1000$ s/mm², the cutoff value of 1.316×10^{-3} mm²/s for ADC_{min} was found to provide the best combination of sensitivity (87%) and specificity (82%) for distinguishing between HGGs and BMs.

In the current study, using a cutoff value of 1.332×10^{-3} mm²/s for peritumoral ADC_{min}, HGGs could be differentiated from BMs with a sensitivity of 95% and a specificity of 84%. For the same cutoff value, GBMs and BMs could be differentiated with a sensitivity of 95% and a specificity of 100%.

DWI examinations included in our study were performed on two different MR scanners, but the same b-value was used for acquisition. It was previously reported that ADC values from different scanners may be different (25). In our study, there were no significant differences between scanners regarding ADC values for HGGs (cases: 16 vs. 14; ADC_{min} = 700.8 ± 41.3 vs. 783.4 ± 88.4; ADC_{mean} = 860.1 ± 52.1 vs. 870.3 ± 66.4; ADC_{edema} = 1237 ± 97.6 vs. 1276 ± 127.1) and for BMs (cases: 15 vs. 12; ADC_{min} = 629.2 ± 103.3 vs. 724.6 ± 90.4; ADC_{mean} = 792.6 ± 102 vs. 857.8 ± 104.7; ADC_{edema} = 1475 ± 79.4 vs. 1455 ± 54.1).

Other advanced MRI techniques, including perfusion imaging, diffusion tensor imaging, spectroscopy, and quantitative MRI, have been used to detect tumor invasion in the peritumoral area and could be able to differentiate between HGGs and BMs (8,20,26-28). For example, several studies have reported that the relative cerebral blood volume ratio and fractional anisotropy in the peritumoral region of HGGs were significantly higher than in BMs (8,20,27). Moreover, it was reported that the choline-to-creatine ratio in the peritumoral region of BMs was significantly lower than in HGGs (20,26). All these observations support the hypothesis that the tumor-infiltrated edema associated with HGGs can be differentiated from pure vasogenic edema associated with BMs. Quantitative MRI analysis could also reflect tumor invasion into the peritumoral edema of HGGs (28). In the present study, only ADC values were analyzed because DWI is available in most hospitals, the post-processing of data is simple and it is the least time-consuming technique.

Based on the results of our study, we may recommend the analysis of multiple ROIs of the peritumoral region for an accurate differentiation between HGGs and BMs. Thus, at least two or three ROIs should be placed within the peritumoral edema, as closely as possible to the tumoral margin, but without risking any contamination with tumoral tissue.

Our study has several limitations. First, the lack of direct correlation of ADC values with histological findings in the same area. Then, the sample size for this study is relatively small. Therefore, larger studies are needed to confirm these results. Finally, we used a retrospective approach to select the cases and the placement of ROIs could be subjective.

In conclusion, our study showed that intratumoral and peritumoral ADC values can help distinguishing HGGs from solitary BMs. Peritumoral ADC values are better than intratumoral ADC values at predicting the tumor type. The results of the present study support the hypothesis that the minimum ADC values within peritumoral edema can detect neoplastic cell infiltration in HGGs.

Declaration of Conflicting Interests

The author(s) declared no potential conflicts of interest with respect to the research, authorship, and/or publication of this article.

Funding

The author(s) received no financial support for the research, authorship, and/or publication of this article.

References

1. Ostrom QT, Bauchet L, Davis FG, et al. The epidemiology of glioma in adults: a "state of the science" review. Neuro Oncol 2014;16:896–913.
2. Louis DN, Ohgaki H, Wiestler OD, et al. The 2007 WHO classification of tumours of the central nervous system. Acta Neuropathol 2007;114:97–109.
3. Patchell RA. Brain metastases. Neurol Clin 1991;9: 817–827.
4. Oh J, Cha S, Aiken AH, et al. Quantitative apparent diffusion coefficients and T2 relaxation times in characterizing contrast enhancing brain tumors and regions of peritumoral edema. J Magn Reson Imaging 2005;21: 701–708.
5. Chen L, Liu M, Bao J, et al. The correlation between apparent diffusion coefficient and tumor cellularity in patients: a meta-analysis. PLoS One 2013;8:e79008.
6. Surov A, Ginat DT, Sanverdi E, et al. Use of diffusion weighted imaging in differentiating between malignant and benign meningiomas. A multicenter analysis. World Neurosurg 2016;88:598–602.
7. Kono K, Inoue Y, Nakayama K, et al. The role of diffusion-weighted imaging in patients with brain tumors. Am J Neuroradiol 2011;22:1081–1088.
8. Svolos P, Tsolaki E, Kapsalaki E, et al. Investigating brain tumor differentiation with diffusion and perfusion metrics at 3T MRI using pattern recognition techniques. Magn Reson Imaging 2013;31:1567–1577.
9. Fan GG, Deng QL, Wu ZH, et al. Usefulness of diffusion/perfusion-weighted MRI in patients with non-enhancing supratentorial brain gliomas: a valuable tool to predict tumour grading? Br J Radiol 2006;79:652–658.
10. Xu XQ, Li Y, Hong XN, et al. Radiological indeterminate vestibular schwannoma and meningioma in cerebellopontine angle area: differentiating using whole-tumor histogram analysis of apparent diffusion coefficient. Int J Neurosci 2016;127:183–190.
11. Stadnik TW, Chaskis C, Michotte A, et al. Diffusion-weighted MR imaging of intracerebral masses: comparison with conventional MR imaging and histologic findings. Am J Neuroradiol 2001;22:969–976.
12. Kitis O, Altay H, Calli C, et al. Minimum apparent diffusion coefficients in the evaluation of brain tumors. Eur J Radiol 2005;55:393–400.
13. Yamasaki F, Kurisu K, Satoh K, et al. Apparent diffusion coefficient of human brain tumors at MR imaging. Radiology 2005;235:985–991.
14. Rollin N, Guyotat J, Streichenberger N, et al. Clinical relevance of diffusion and perfusion magnetic resonance imaging in assessing intra-axial brain tumors. Neuroradiology 2006;48:150–159.
15. Lee EJ, terBrugge K, Mikulis D, et al. Diagnostic value of peritumoral minimum apparent diffusion coefficient for differentiation of glioblastoma multiforme from solitary metastatic lesions. Am J Roentgenol 2011;196:71–76.

16. Han C, Huang S, Guo J, et al. Use of a high b-value for diffusion weighted imaging of peritumoral regions to differentiate high-grade gliomas and solitary metastases. J Magn Reson Imaging 2015;42:80–86.
17. Chiang IC, Kuo YT, Lu CY, et al. Distinction between high-grade gliomas and solitary metastases using peritumoral 3-T magnetic resonance spectroscopy, diffusion, and perfusion imagings. Neuroradiology 2004;46:619–627.
18. Krabbe K, Gideon P, Wagn P, et al. MR diffusion imaging of human intracranial tumors. Neuroradiology 1997; 39:483–489.
19. Server A, Kulle B, Maehlen J, et al. Quantitative apparent diffusion coefficients in the characterization of brain tumors and associated peritumoral edema. Acta Radiol 2009;50:682–689.
20. Tsougos I, Svolos P, Kousi E, et al. Differentiation of glioblastoma multiforme from metastatic brain tumor using proton magnetic resonance spectroscopy, diffusion and perfusion metrics at 3 T. Cancer Imaging 2012;12: 423–436.
21. Pope WB, Mirsadraei L, Lai A, et al. Differential gene expression in glioblastoma defined by ADC histogram analysis: relationship to extracellular matrix molecules and survival. Am J Neuroradiol 2012;33:1059–1064.
22. Cha S. Update on brain tumor imaging: from anatomy to physiology. Am J Neuroradiol 2006;27:475–487.
23. Bertossi M, Virgintino D, Maiorano E, et al. Ultrastructural and morphometric investigation of human brain capillaries in normal and peritumoral tissues. Ultrastruct Pathol 1997;21:41–49.
24. Pavlisa G, Rados M, Pavic L, et al. The differences of water diffusion between brain tissue infiltrated by tumor and peritumoral vasogenic edema. Clin Imaging 2009;33: 96–101.
25. Belli G, Busoni S, Ciccarone A, et al. Quality assurance multicenter comparison of different MR scanners for quantitative diffusion-weighted imaging. J Magn Reson Imaging 2016;43:213–219.
26. Server A, Josefsen R, Kulle B, et al. Proton magnetic resonance spectroscopy in the distinction of high-grade cerebral gliomas from single metastatic brain tumors. Acta Radiol 2010;51:316–325.
27. Wang S, Kim S, Chawla S, et al. Differentiation between glioblastomas, solitary brain metastases, and primary cerebral lymphomas using diffusion tensor and dynamic susceptibility contrast-enhanced MR imaging. Am J Neuroradiol 2011;32:507–514.
28. Blystad I, Warntjes JBM, Smedby Ö, et al. Quantitative MRI for analysis of peritumoral edema in malignant gliomas. PLoS One 2017;12:e0177135.

brain sciences

MDPI

Article

Differentiating High-Grade Gliomas from Brain Metastases at Magnetic Resonance: The Role of Texture Analysis of the Peritumoral Zone

Csaba Csutak [1,2], Paul-Andrei Ștefan [1,3,*], Lavinia Manuela Lenghel [1,2], Cezar Octavian Moroșanu [4], Roxana-Adelina Lupean [5], Larisa Șimonca [6], Carmen Mihaela Mihu [1,5] and Andrei Lebovici [1,2]

[1] Radiology and Imaging Department, County Emergency Hospital, Cluj-Napoca, Clinicilor Street, Number 5, Cluj-Napoca, 400006 Cluj, Romania; csutakcsaba@yahoo.com (C.C.); pop.lavinia@umfcluj.ro (L.M.L.); carmenmihu@umfcluj.ro (C.M.M.); andrei1079@yahoo.com (A.L.)

[2] Radiology, Surgical Specialties Department, "Iuliu Haţieganu" University of Medicine and Pharmacy, Clinicilor Street, number 3–5, Cluj-Napoca, 400006 Cluj, Romania

[3] Anatomy and Embryology, Morphological Sciences Department, "Iuliu Haţieganu" University of Medicine and Pharmacy, Victor Babeș Street, number 8, Cluj-Napoca, 400012 Cluj, Romania

[4] Department of Neurosurgery, North Bristol Trust, Southmead Hospital, Southmead Road, Westbury on Trym, Bristol BS2 8BJ, UK; cezar.morosanu@nbt.nhs.uk

[5] Histology, Morphological Sciences Department, "Iuliu Hațieganu" University of Medicine and Pharmacy, Louis Pasteur Street, number 4, Cluj-Napoca, 400349 Cluj, Romania; roxanalupean92@gmail.com

[6] Department of Paediatric Surgery, Bristol Royal Hospital for Children, Upper Maudlin Street, Bristol BS2 8BJ, UK; larisa.simonca@UHBristol.nhs.uk

* Correspondence: stefan_paul@ymail.com; Tel.: +40-743-957-206

Received: 12 August 2020; Accepted: 14 September 2020; Published: 16 September 2020

Abstract: High-grade gliomas (HGGs) and solitary brain metastases (BMs) have similar imaging appearances, which often leads to misclassification. In HGGs, the surrounding tissues show malignant invasion, while BMs tend to displace the adjacent area. The surrounding edema produced by the two cannot be differentiated by conventional magnetic resonance (MRI) examinations. Forty-two patients with pathology-proven brain tumors who underwent conventional pretreatment MRIs were retrospectively included (HGGs, $n = 16$; BMs, $n = 26$). Texture analysis of the peritumoral zone was performed on the T2-weighted sequence using dedicated software. The most discriminative texture features were selected using the Fisher and the probability of classification error and average correlation coefficients. The ability of texture parameters to distinguish between HGGs and BMs was evaluated through univariate, receiver operating, and multivariate analyses. The first percentile and wavelet energy texture parameters were independent predictors of HGGs (75–87.5% sensitivity, 53.85–88.46% specificity). The prediction model consisting of all parameters that showed statistically significant results at the univariate analysis was able to identify HGGs with 100% sensitivity and 66.7% specificity. Texture analysis can provide a quantitative description of the peritumoral zone encountered in solitary brain tumors, that can provide adequate differentiation between HGGs and BMs.

Keywords: glioblastoma; computer-aided diagnosis; magnetic resonance imaging; texture analysis

1. Introduction

High-grade gliomas (HGGs) are the most common malignant brain tumors in adults, while brain metastases (BMs) affect 20–30% of patients with cancer [1]. The clinical and imaging differentiation between the two entities is crucial, as they have very different management strategies [2].

Tumor angiogenesis with disruption of the blood–brain barrier (BBB) is responsible for the vasogenic edema encountered in both benign and malignant brain lesions. Two types of vasogenic peritumoral edema have been defined. The first type is due to parenchymal compression which can lead to secondary ischemia and can be found near low-grade and nonglial tumors [3]. Because there is no histological evidence of tumoral cellularity outside the margins of metastatic lesions, this edema is considered "pure vasogenic" [1]. The second type is encountered in high-grade glial tumors and is caused by additional derangements of the BBB by malignant cell infiltration [3]. Thus, it is possible that an accurate imaging assessment of the malignant cell infiltration within the peritumoral edema can provide a noninvasive diagnostic alternative in distinguishing HGGs from brain metastases. Conventional magnetic resonance imaging (MRI) examination often shows common features of solitary metastatic brain tumors and high-grade gliomas [4,5], as they both express surrounding edema, necrotic center, and irregular enhancing margins [6]. These similarities lead to imaging misclassification in more than 40% of cases [7]. Because BMs tend to displace rather than invade surrounding tissues, the peritumoral edema is considered pure vasogenic [8,9]. On the other hand, HGGs and especially glioblastomas usually invade the surrounding structures, tumor cells infiltrating the white matter [10]. An important key point in discriminating HGGs from BMs may lie in detecting the differences between the two types of edemas.

Although conventional MRI brain examinations are widely available, the standard sequences lack pathology-specific biomarkers and the signal does not possess biological specificity. Thus, a nonspecific increase in the blood–brain barrier permeability is reflected by contrast enhancement, and the tissue water content influences T2-weighted signal abnormalities. Due to these factors, conventional MRI is unable to accurately characterize the surrounding edema of solitary brain tumors [11]. More advanced MRI techniques such as spectroscopy, perfusion, diffusion-weighted, and diffusion tensor imaging have also been used to quantify the peritumoral zone, but the results are often contradictory [10,12,13].

Most certainly, standard MRI sequences carry additional diagnostic information, but this information is difficult to be assessed during the routine evaluation of medical images. The histopathological particularities of the two types of edema may influence the pixel intensity and spatial distribution within MRI images, but these changes are too subtle to be macroscopically quantified.

Computer-aided diagnostic methods involving medical images have advanced in recent years from a small research topic to a successful implementation in some areas of clinical practice [14]. Many of these augmented diagnostic methods rely on the evaluation of textures and promise major upgrades in the way physicians interpret examinations [15]. Textures represent the intrinsic and intuitive properties of surfaces such as roughness, granulation, and regularity [16]. In recent years, texture analysis (TA) has emerged as a noninvasive method for quantifying the information composed especially in magnetic resonance images [17]. TA represents a noninvasive radiomics method to assess macroscopic tissue heterogeneity which is indirectly linked to microscopic tissue heterogeneity indiscernible to human visual perception [18]. Through specific parameters, TA aims to offer a quantitative assessment of image contents by analyzing the distribution patterns and intensity of the pixels [19]. So far, most TA studies involving gliomas have focused on solid tumor components [20,21], while the surrounding peritumoral aspects remained relatively unexplored.

Our objective was to analyze the peritumoral zone of solitary intracerebral brain lesions with texture analysis to determine noninvasive differentiation criteria for HGGs and BMs. We aimed to assess the diagnostic power of texture parameters by evaluating their individual and combined capability of discriminating between the two entities.

2. Materials and Methods

2.1. Patients

This Health Insurance Portability and Accountability Act-compliant, single-institution, retrospective pilot study was approved by the institutional review board (ethics committee of the

"Iuliu Hațieganu" University of Medicine and Pharmacy Cluj-Napoca; registration number, 50; date, 11 March 2019), and a waiver consent was obtained owing to its retrospective nature. The database was obtained from our radiology information system (RIS) and consisted of all the reports of MRI brain examinations performed between May 2016 and March 2020. The original search yielded 1765 reports. Each report was analyzed, and those reports that did not refer to a supratentorial intraparenchymal brain mass were excluded (n = 942), as well as those that refer to the recurrence of a malignant lesion (n = 196). The medical records of the remaining 627 patients were retrieved from the archive of our healthcare unit to be investigated for disease-related data. Further exclusion criteria were: the benign nature of a lesion (n = 263), the absence of a final histopathological result (n = 84), and nonsolitary lesions (n = 177). The remaining 103 studies were reviewed by one radiologist, which excluded all examinations with artifacts affecting the quality of the T1- and T2-weighted images (T2WI, n = 19), tumors below 25 mm (n = 61), and lesions with a maximum diameter of the peritumoral edema below 15 mm as visible on fluid-attenuated inversion recovery (FLAIR) sequence (n = 23; Figure 1).

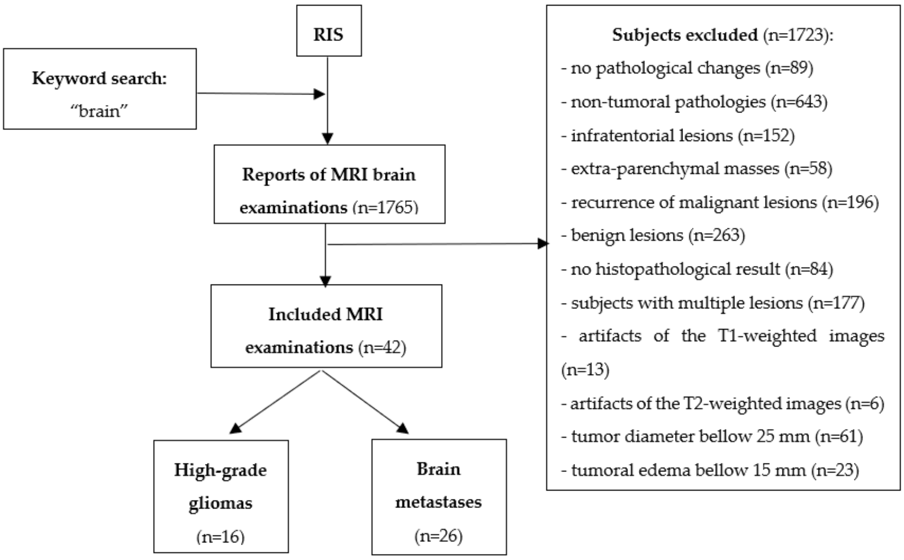

Figure 1. Patients. RIS, radiology information system; MRI, magnetic resonance imaging.

Of the 1765 patients who referred to our department during the study period, 42 were included in the study after applying the inclusion and exclusion criteria (29 men, 17 women; mean age = 62.6 ± 12.3 years; age range = 32–81 years). Subjects were further divided according to the final pathological diagnosis of their lesions in high-grade gliomas (HGGs, n = 16) and brain metastases (BMs, n = 26). Gliomas were classified according to the 2016 World Health Organization (WHO) classification of tumors of the central nervous system. Out of 42 patients, WHO grade IV glioblastoma was diagnosed in 11 patients (six males (m)/5 females (f)) and WHO grade III glioma in five patients (three anaplastic astrocytomas (2m/1f) and two anaplastic oligoastrocytomas (2m)). The brain metastases group included: 13 subjects with pulmonary adenocarcinoma (13m/4f), four with melanoma (2m/2f), three patients with colorectal carcinoma (1m/2f), two with pulmonary squamous cell carcinoma (2m), two with breast cancer (2f), one with a neuroendocrine tumor of the mesentery, (1f) and one with clear cell renal carcinoma (1m).

2.2. MRI Protocol

All scans were performed on the same unit (1.5-T, SIGNA™ Explorer, General Electric, GE Healthcare, Fairfield, Waukesha, WI, USA). Conventional sequences, including T1-weighted images, T2-weighted images, fluid-attenuated inversion recovery images, diffusion-weighted images, and contrast-enhanced T1-weighted images were obtained. Although the protocol varied because the examinations were retrieved from a range of approximately 4 years, each protocol included an axial T2-weighted Periodically Rotated Overlapping Parallel Lines with Enhanced Reconstruction (PROPELLER) sequence (repetition time, 7300 ms; echo time, 107 ms; slice thickness, 4 mm; field of view, 240 × 240 mm^2; matrix, 384 × 384), and a contrast-enhanced T1-weighted fast spin echo (FSE) sequence (repetition time, 9 ms; echo time, 2.38 ms; slice thickness, 2.2 mm; field of view, 180 × 240 mm^2; matrix, 256 × 256), which were the only ones used for the texture computation.

2.3. Texture Analysis Protocol

The traditional approach of radiomics consists of four steps: image segmentation using regions of interest, feature extraction, feature selection, and prediction. On a dedicated workstation (General Electric, Advantage workstation, 4.7 edition), all examinations were reviewed by two radiologists, blinded to the final diagnosis. The two examiners develop a common opinion about the slice considered to be the most representative for the peritumoral region from the postcontrast T1-weighted (T1W) sequence. The selected slice, along with the corresponding image on the T2-weighted (T2W) sequence, were retrieved in Digital Imaging and Communications in Medicine (DICOM) format and further imported in a texture analysis software, MaZda version 5 (Institute of Electronics, Technical University of Lodz, Łódź, Poland) [22]. The area outside the solid part of the tumor was defined as the peritumoral region. On the postcontrast T1W reference images, a region of interest (ROI) was placed as closely as possible to the tumoral margin. A semiautomatic level set technique was used for the definition and positioning of each ROI. One researcher placed a seed near the tumoral boundaries, and the software automatically delineated the peritumoral zone based on gradient and geometric coordinates. Since this technique did not involve manual delimitation of the structure of interest contours, the assessment of inter- or intraobserver reproducibility was not performed in the current study. Once defined, the ROI was transferred to the corresponding T2W slice, on which texture analysis was performed (Figure 2). Since contrast and brightness variations can affect the true texture of the image, a gray-level normalization for each ROI was performed by using the limitation of dynamics to $\mu \pm 3\sigma$ (μ = gray-level mean; and σ = gray-level standard deviation) [23].

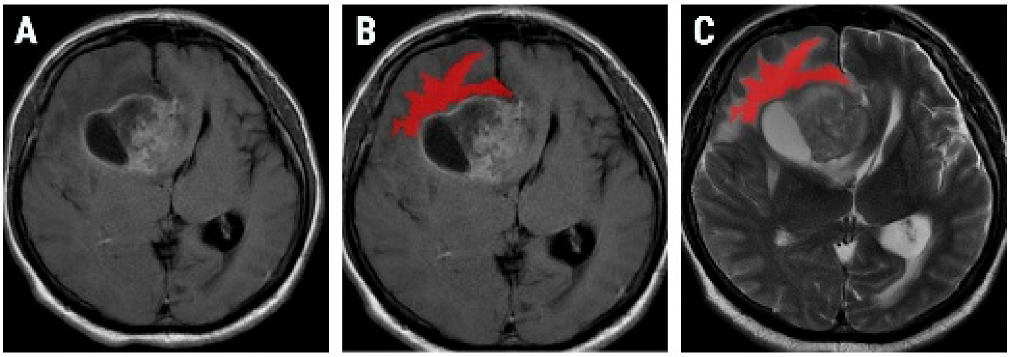

Figure 2. Axial contrast-enhanced T1-weighted image of a 56-year-old patient with pathologically proven glioblastoma (**A**) and the region of interest (red) overlapping the peritumoral area (**B**) on a postcontrast T1-weighted image, which was consequentially transferred on to a synchronized slice on the T2-weighted sequence (**C**).

The features computed by the software′ generator originated from the gray-level histogram, the absolute gradient, the wavelet transformation, the co-occurrence matrix, the run-length matrix, and the autoregressive model. The features generated by MaZda software include several hundred elements per ROI. Since such a large number of data is hard to be handled by common statistical analysis software, the MaZda software allows the selection of the most discriminative features through reduction techniques. These techniques highlight subsets of features that allow minimum error classification of analyzed image textures [24]. One such technique is represented by the Fisher selection method. The Fisher coefficient (F) defines the ratio of between-class variances to within-class variances [25].

Overall, this method provides a set of 10 features that have a high discriminatory ability. Alongside the Fisher method, another selection technique based on the probability of classification error and average correlation coefficients (POE + ACC) was utilized [24]. By applying these selection methods, two sets, each containing 10 features, were selected. The first one contained highly discriminative features produced by the Fisher method, and the second one was based on the minimization of classification error generated by the POE + ACC technique.

To evaluate texture features and individual ability to discriminate within groups, their absolute values were compared using the independent samples *t*-test. The receiver operating characteristic (ROC) analysis was performed, with the calculation of the area under the curve (AUC) with 95% confidence intervals (CIs) for the parameters showing *p*-values below 0.05 on the univariate analysis. Optimal cut-off values were chosen using an optimization step that maximized the Youden index for predicting patients with HGGs, and sensitivity and specificity were computed from the same data, without other adjustments. The ROC curves' comparisons were conducted using the DeLong et al. method [26]. Secondly, a multiple regression analysis was performed, using an "enter" input model (which consisted of inputting all variables in the model in one single step), to identify which of the texture parameters that showed statistically significant results at the univariate analysis are also independent predictors of HGGs. The coefficient of determination (R-squared) was computed, and the diagnostic value of the prediction model was evaluated using ROC analysis. Statistical analysis was performed using a commercially available dedicated software MedCalc version 14.8.1 (MedCalc Software, Mariakerke, Belgium).

The feature name generated by MaZda software contains abbreviations of feature characteristics produced by the extraction algorithm. The outermost symbol from the left indicates the first imaging processing procedure. The first letter indicates the color channel ("C" implies that a black and gray image was computed, "R" identifies the red color channel). The second symbol stands for image normalization (N) after which comes the encoding for the method used, in this case "S", which represents image normalization using the limitation of dynamics to $\mu \pm 3\sigma$. The following number indicates the feature was quantized to use that particular number of bits per pixel. The direction is coded using letters: H (horizontal), V (vertical), Z (45°), and N (135°). The next group of letters identifies the extraction algorithm (e.g., Wav, Haar wavelet transformation). The feature name is usually the last group of letters (LngREmph, long-run emphasis; ShrtREmp, short-run emphasis; En, energy) [27]. The MaZda software was also used to generate maps that show the distribution of a particular texture parameter in computed images.

3. Results

Most texture features selected by the Fisher method derived from the first-order histogram and run-length matrix, while the ones highlighted by the POE + ACC method originated from the co-occurrence matrix and wavelet transformation. Four texture parameters (1% percentile (Perc01), 10% percentile (Perc10), wavelet energy (WavEnLL_s-4), and the fraction of image in runs (RNS6Fraction)) were highlighted following both selection methods. The comparison of HGGs and BMs based on the absolute values of the parameters selected by the Fisher method held statistically significant results in all 10 cases. The comparison between the two entities based on POE + ACC set reached statistically significant results for five parameters, of which four were the same previously selected by the Fisher method. The feature sets selected by Fisher and POE + ACC methods along with the univariate analysis results are displayed in Table 1. Overall, the parameters showing statistically significant results derived from histogram analysis, wavelet transformation, and the run-length matrix (Table 2).

Table 1. Sets of features generated by each selection method and the univariate analysis results following the comparison of high-grade gliomas with brain metastases.

Fisher	F	*p*-Value	POE + ACC	PP	*p*-Value
Perc01 *	2.31	**<0.0001**	CV5S6SumOfSqs	0.39	0.0883
Perc10 *	1.73	**0.0002**	CV4S6InvDfMom	0.41	0.0997
Mean	1.27	**0.0013**	WavEnHH_s-1	0.46	**0.0067**
Perc50	1.22	**0.0015**	WavEnHL_s-4	0.47	0.3853
WavEnLL_s-4 *	1.2	**0.0062**	Perc10 *	0.47	**0.0002**
RNS6ShrtREmp	0.96	**0.0045**	RNS6Fraction *	0.49	**0.0057**
Perc90	0.92	**0.0053**	WavEnLL_s-4 *	0.49	**0.0062**
RNS6Fraction *	0.9	**0.0057**	CZ5S6SumAverg	0.49	0.5007
RNS6LngREmph	0.81	**0.0083**	WavEnLH_s-4	0.49	0.7559
Perc99	0.78	**0.0096**	Perc01 *	0.64	**<0.0001**

* parameters highlighted by both classification methods. Bold values are statistically significant. F, Fisher coefficients; POE + ACC, probability of classification error and average correlation; PP, POE + ACC coefficients; *p*-value showing the univariate analysis result; Perc 01/10/50/90/99, 1%/10%/50%/90%/99% percentile; Mean, histogram mean; WavEn, wavelet energy; ShrtREmp, short-run emphasis; Fraction, the fraction of image in runs; LngREmph, long-run emphasis; SumOfSqs, the sum of squares; InvDfMom, inverse difference moment; SumAverg, sum average.

Table 2. The parameters that show statistically significant results at the univariate analysis and their average values recorded in each group.

Parameter	HGGs	BMs
Perc01	33,848.43 ±328.15	34,308.65 ± 298.8
Perc10	33,994.5 ± 363.17	34,437 ± 322.34
Perc50	34,182.12 ± 433.34	34,581.69 ± 325.32
Perc90	34,331.18 ± 466.79	34,699.46 ± 341.39
Perc99	34,411.31 ± 489.28	34,765.03 ± 352.9
Mean	34,171.97 ± 420.92	34,573.13 ± 325.66
WavEnLL_s-4	10,272.3 ± 4385.84	6579.94 ± 2732.81
WavEnHH_s-1	6.25 ± 3.47	10.96 ± 7.11
RNS6Fraction	0.9 ± 0.02	0.93 ± 0.02
RNS6ShrtREmp	0.93 ± 0.01	0.94 ± 0.01
RNS6LngREmph	1.32 ± 0.11	1.23 ± 0.08

Data are expressed as mean ± standard deviation. HGGs, high-grade gliomas; BMs, brain metastases; Perc 01/10/50/90/99, 1%/10%/50%/90%/99% percentile; Mean, histogram mean; WavEn, wavelet energy; ShrtREmp, short-run emphasis; Fraction, the fraction of image in runs; LngREmph, long-run emphasis.

The ROC analysis results are displayed in Table 3. Considering all calculated parameters, Perc01 yielded the highest AUC (0.858; CI, 0.716–0.946) which was statistically different from all parameters derived from histogram analysis, but from the ones computed by wavelet transformation and run-length matrix (Table 4). Overall, the first-order histogram-derived parameters obtain a high specificity at a cost of a medium-to-high sensibility for the differentiation of HGGs from BMs, while parameters computed from wavelet transformation and rung-length matrix showed opposite results. The *p*-values for the ROC curve comparisons are reported in Table 4. The ROC curves of the six parameters that showed the highest AUCs are displayed in Figure 3.

Table 3. Receiver operating characteristic (ROC) analysis results of the texture parameters in high-grade gliomas' assessment.

Parameter	Sign. Lvl.	AUC	J	Cut-Off	Sensitivity (%)	Specificity (%)
Perc01	<0.0001	0.858 (0.716–0.946)	0.63	≤34,039	75 (47.6–92.7)	88.46 (69.8–97.6)
Perc10	0.0031	0.748 (0.59–0.869)	0.53	≤34,081	68.75 (41.3–89)	84.62 (65.1–95.6)
Perc50	0.0003	0.772 (0.616–0.887)	0.42	≤34,466	81.25 (54.4–96)	61.54 (40.6–79.8)
Perc90	0.006	0.726 (0.567–0.852)	0.37	≤34,728	87.5 (61.7–98.4)	87.5 (61.7–98.4)
Perc99	0.0084	0.719 (0.559–0.846)	0.37	≤34,831	87.5 (61.7–98.4)	87.5 (61.7–98.4)
Mean	0.0002	0.774 (0.619–0.889)	0.42	≤34,154.86	50 (24.7–75.3)	92.31 (74.9–99.1)
WavEnLL_s-4	0.0009	0.757 (0.6–0.876)	0.41	>6458.11	87.5 (61.7–98.4)	53.85 (33.4–73.4)
WavEnHH_s-1	0.0294	0.68 (0.519–0.816)	0.38	≤14.8	100 (79.4–100)	38.46 (20.2–59.4)
RNS6Fraction	0.0004	0.748 (0.606–0.88)	0.46	≤0.94	100 (79.4–100)	46.15 (22.6–66.6)
RNS6ShrtREmp	0.0001	0.776 (0.622–0.89)	0.46	≤0.95	100 (79.4–100)	46.15 (22.6–66.6)
RNS6LngREmph	0.0041	0.728 (0.596–0.854)	0.38	>1.23	81.25 (54.4–96)	57.69 (36.9–76.6)

Between brackets are the values corresponding to the 95% confidence interval. Sign.lvl., significance level; J, Youden index; Perc 01/10/50/90/99, 1%/10%/50%/90%/99% percentile; Mean, histogram mean; WavEn, wavelet energy; ShrtREmp, short-run emphasis; Fraction, the fraction of image in runs; LngREmph, long-run emphasis; AUC, area under the curve.

Table 4. Comparison of ROC curves in the differentiation of high-grade gliomas from brain metastases. Numbers represent *p*-values. Each *p*-value column represents the comparison between all parameters and the reference one (REF). Values in bold are statistically significant.

Perc01	**REF**	**0.0021**	**0.0362**	**0.0109**	**0.0095**	**0.0231**	0.2766	0.0572	0.2933	0.3627	0.17
Perc10	**0.0021**	REF	0.5385	0.6518	0.5633	0.4581	0.9311	0.552	0.9007	0.7992	0.872
Perc50	**0.0362**	0.5385	REF	**0.0203**	**0.0264**	0.7778	0.8862	0.3996	0.7568	0.964	0.7041
Perc90	**0.0109**	0.6518	**0.0203**	REF	0.3795	**0.0233**	0.7691	0.6882	0.7568	0.6589	0.9843
Perc99	**0.0095**	0.5633	**0.0264**	0.3795	REF	**0.0256**	0.7191	0.7373	0.7122	0.6169	0.9377
Mean	**0.0231**	0.4581	0.7778	**0.0233**	**0.0256**	REF	0.8668	0.1105	0.9103	0.9817	0.6822
WavEnLL_s-4	0.2766	0.9311	0.8862	0.7691	0.7191	0.8668	REF	0.4324	0.9553	0.8246	0.7434
WavEnHH_s-1	0.0572	0.552	0.3996	0.6882	0.7373	0.1105	0.4324	REF	0.1105	0.0655	0.3928
RNS6Fraction	0.2933	0.9007	0.7568	0.7568	0.7122	0.9103	0.9553	0.1105	REF	0.358	0.0693
RNS6ShrtREmp	0.3627	0.7992	0.964	0.6589	0.6169	0.9817	0.8246	0.0655	0.358	REF	0.0705
RNS6LngREmph	0.17	0.872	0.7041	0.9843	0.9377	0.6822	0.7434	0.3928	0.0693	0.0705	REF

Perc 01/10/50/90/99, 1%/10%/50%/90%/99% percentile; Mean, histogram mean; WavEn, wavelet energy; ShrtREmp, short-run emphasis; Fraction, the fraction of image in runs; LngREmph, long-run emphasis.

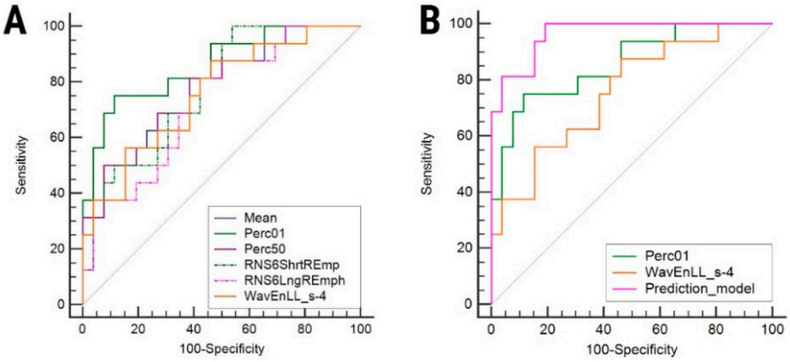

Figure 3. Comparison of receiver operating characteristic (ROC) curves between (**A**) the six texture parameters that showed the highest area under the curve, and (**B**) independent parameters and the predictive model for the diagnosis of high-grade gliomas. Mean, histogram mean; Perc01/50, 1%/50% percentile; ShrtREmp, short-run emphasis; LngREmph, long-run emphasis; WavEn, wavelet energy.

The multiple regression analysis that integrated all parameters showing statistically significant results at the univariate analysis showed that Perc01 ($p = 0.037$) and WavEnLL_s-4 ($p = 0.031$) were independent predictors of high-grade gliomas (Table 5). The variance inflation factor (VIF) yielded high values for most texture parameters, which indicates the multicollinearity of the independent variables.

The mean parameter was excluded from the prediction model due to the high VIF values (VIF > 10^4). The overall prediction model showed an approximately equal sensitivity (100%; CI, 29.2–100%) and specificity (66.7%; CI, 49.8–80.9%), and a highest AUC (0.964; CI, 0855–0.997) for the diagnosis of HGGs than the ones exhibited by the parameters included in the model. The ROC comparison between the prediction model and the two independent predictors showed statistically significant results (Perc01, $p = 0.04$; WavEnLL_s-4, $p = 0.003$; Figure 2B).

Table 5. Multivariate analysis of factors independently associated with the presence of high-grade gliomas. Bold values are statistically significant.

Independent Variable	Coefficient	Standard Error	*p*-Value	VIF
Perc01	−0.002	0.001	**0.0370**	67.869
Perc10	0.001	0.002	0.4061	247.596
Perc50	0.0008	0.003	0.7806	555.997
Perc90	−0.006	0.006	0.3198	2433.857
Perc99	0.005	0.004	0.2162	1245.022
RNS6Fraction	0.91	77.72	0.9906	1224.984
RNS6LngREmph	3.08	10.38	0.7682	405.915
RNS6ShrtREmp	−19.75	49.49	0.6925	270.604
WavEnHH_s-1	−0.004157	0.01405	0.7692	2.693
WavEnLL_s-4	0.0000413	0.0000182	**0.0311**	1.672
Sign. level.	**0.0002**			
R^2	0.6180			
R^2 adjusted	0.4948			
M.R. Coef.	0.7861			

VIF, variance inflation factor; R^2, coefficient of determination; R^2 adjusted, coefficient of determination adjusted for the number of independent variables in the regression model; Sign. level, the significance level of the multivariate analysis; M.R. Coef., multiple correlation coefficient.

4. Discussion

Our results show that 16 individual texture parameters were highlighted by the selection methods, with 11 recorded statistically significant results at the univariate analysis. Perc01 showed the highest AUC (0.858; CI, 0.716–0.946), while also being an independent predictor of HGGs, together with the WavEnLL_s-4 parameter.

Because the edemas encountered in HGGs and BMs express high-intensity signals on both T2W and FLAIR sequences, it is very difficult for them to be macroscopically differentiated through conventional MRI examinations [1]. Mucio and colleagues [28] observed a moderate diagnostic value when differentiating between the two based on signal alteration in the adjacent cortex (sensitivity, 60.7%; specificity, 67.9%). Additionally, the results of functional MRI diffusion-weighted sequences show contradictions. Some studies [10,29,30] found a restricted water diffusion along the margins of HGGs and attributed it to malignant cell infiltration, while others [28,31,32] concluded that there is no difference in diffusion measurements of the peritumoral edema between the two entities. More advanced MRI techniques such as multivoxel proton magnetic resonance spectroscopy have also been used to assess the two types of peritumoral regions, with uncertain outcomes. Tsugos and colleagues [33] found a decrease in N-acetyl-aspartate/Creatinine ratio in the peritumoral areas of glioblastomas compared to BMs, Jiun-Lin Yan et al. [34] found no statistically significant difference between the two, and Wijnen et al. [35] reported an increase of this ratio. Perfusion MRI techniques such as dynamic susceptibility contrast MRI can also be used to quantify the peritumoral infiltration of glioblastomas due to their increased perfusion and angiogenesis [12]. The high values of the relative cerebral blood volume (rCBV) in the peritumoral area were found to be strongly correlated with cellular proliferation of HGGs by some authors [13,34], while others [36] found it to be a poor diagnostic feature. In terms of fractional anisotropy, Bette et al. [37] evaluated 294 patients with HGGs and BMs and found no significant differences in the peritumoral area.

Most texture analysis studies involving gliomas focus on intratumoral characteristics, while the surrounding area of these lesions remains relatively unexplored. Differentiating high-grade from low-grade gliomas is one of the most researched topics in this domain [20,21,38–40]. Despite variability in image segmentation and TA software, the entropy parameter computed from apparent diffusion coefficient (ADC) maps consistently showed very good results in differentiating the two [20,39]. We were able to find only a few studies compatible with our research. Skogen et al. [41] investigated the utility of TA in the differentiation of glioblastomas from brain metastases based on the peritumoral area as seen on diffusion tensor images (DTI). Although a similar number of patients were enrolled (n = 43), the workflow was almost entirely different. TA was performed on a commercially available software (TexRAD) which provided the analysis of five texture parameters (mean, standard deviation, entropy, skewness, and kurtosis) and the ROIs were freehand-drawn within 1 cm of the tumor boundaries of fractional anisotropy (FA) and ADC maps. Entropy was again the parameter with the highest discriminatory ability following its computation from FA maps (80% sensitivity, 90% specificity, and an AUC of 0.88) followed by the standard deviation [41]. Furthermore, TA of the peritumoral area was also performed by Mouthuy et al., [42] who concluded that by combining texture features with rCBV parameters, the differentiation of two entities has an increased performance (92% sensitivity, 71% specificity). The good results of the peritumoral area assessment using TA were also observed by Artzi et al., [43], which by the use of a machine-learning algorithm (support-vector-machine) accomplished an overall 87% accuracy, 86% sensitivity, and 89% specificity for the training test data in distinguishing the two entities.

The first-order histogram is one of the most common statistical methods for image feature computation. The histogram does not consider the spatial relations between the pixels, reflecting only the value of their intensity [44] through parameters such as mean, standard deviation, variance, skewness, kurtosis, and percentiles. Out of nine histogram features that can be generated by MaZda [22], six were highlighted by the selection methods and showed statistically significant results when comparing HGGs and BMs. In all six cases, the average values were higher for BMs than for HGGs. The mean parameter reflects the average value of the pixels within the ROI [45]. The percentile number (n) is the point at which n% of the pixel values that form the histogram are found to the left [46]. In other words, a percentile gives the highest gray-level value under which a given percentage of the pixels in the image are contained [47]. This signifies that 1%, 10%, 50%, 90%, and 99% of the pixels within images were distributed under lower values for HGGs than for BMs, and the average pixel intensity was lower for the primary tumors. It is possible that the higher pixel values recorded in the peritumoral zone of BMs could be a result of the pure vasogenic edema that surrounds these lesions, the increase extracellular water due to the breakdown of the blood–brain barrier could lead to an increase in the T2W signal. Previous studies have also successfully demonstrated the role of first-order histogram percentiles in the diagnosis of glial tumors. Two studies [20,48] using texture features computed from ADC maps showed that the 5th percentile derived from the whole-tumor ROI successfully differentiated between high- and low-grade gliomas, while also being strongly correlated with the Ki-67 labeling index (p = 0.003) [48]. Additionally, in our study, one of the highest AUCs was obtained by two percentiles (Perc01, AUC = 0.858; Perc50, AUC = 0.772) which indicates that they possess a high practical value for the diagnosis of gliomas.

The gray-level run-length matrix (RLM) is a method of extracting higher-order statistical texture features [49]. The RLM quantifies pixel runs with a specific grayscale level and length [27]. A run is a line of pixels having the same intensity values. There are four directions of pixel runs. The number of pixels within a run defines the run length, and the value of the run length is given by the number of occurrences [49]. Three parameters derived from the RLM, all computed for the 135° direction, showed statistically significant results when comparing HGGs with BMs: short-run emphasis (RNS6ShrtREmp, p = 0.0045), long-run emphasis (RNS6LngREmph, p = 0.0083), and the fraction of image in runs (RNS6Fraction, $p = 0.0057$). Short- and long-run emphasis reflects the distribution of short or long homogeneous runs in an image [50]. Higher values of short-run emphasis indicate fine textures, while higher values of long-run emphasis reflect coarse surfaces [51]. The percentage of pixels that are part of any of the runs is measured through the fraction of images in runs [47]. The latter reflects the ration of the total number of runs in the image to the total number of pixels in the image and it is not relevant from a histopathological or imaging point of view in this case. We obtained higher average values of short-run emphasis for BMs and higher average long-run emphasis values for HGGs. These reflect a rougher peritumoral zone in the case of gliomas. This could reflect the difference between neoplastic invasion and vasogenic edema, the infiltrative growth of HGGs causing irregularities in pixel intensities, and breaking the pixel runs. The maps that show the distribution of short- and long-run emphasis in images of HGGs and BMs are shown in Figure 4.

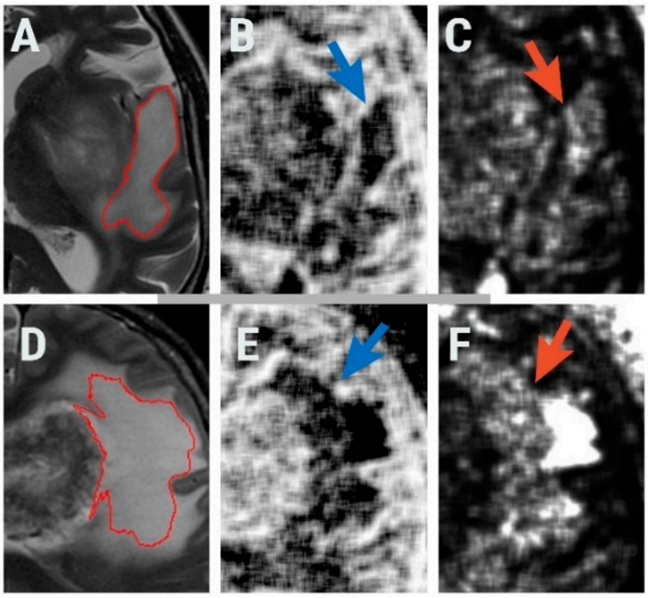

Figure 4. Axial T2-weighted image of a 61-year-old patient with glioblastoma (**A**) and the region of interest (red) used for texture analysis; (**B**) generated map based on short-run emphasis parameter (blue arrow pointing to the peritumoral zone); (**C**) generated map based on long-run emphasis parameter (orange arrow pointing to the peritumoral zone; axial T2-weighted image of a 68-year-old patient with brain metastases (**D**) and the region of interest (red) used for texture analysis; (**E**) generated map based on short-run emphasis parameter (blue arrow pointing to the peritumoral zone); (**F**) generated map based on long-run emphasis parameter (orange arrow pointing to the peritumoral zone.

Wavelet transformation is a multiresolution technique that aims to transform images into a representation that can contain spatial as well as frequency information [52]. This transformation allows the quantification of the frequency content of an image, which is directly proportional to the gray-level variations within that image. Firstly, images are scaled up five times both in vertical and horizontal directions. Furthermore, two types of filters (high and low pass) are applied to separate the image data [53]. Finally, different subbands are extracted from an image that becomes subdivided into four parts, corresponding to different frequency components. The result is a five-scaled image with four frequency bands on every scale, each labeled as low–low (LL), high–low (HL), low–high (LH), and high–high (HH). The LL band contains low-frequency signal contents, whereas the HH band contains high-frequency signal contents, which carry less importance than the LL band [52]. A five-level decomposition diagram of a T2W image of glioblastoma is displayed in Figure 5. The energy feature can be computed from each subband [52]. Wavelet energy quantifies the distribution of energy along the frequency axis over scale and orientation [54]. Energy measures the local uniformity within an image. When the gray levels of an image are distributed under a constant or periodical form, energy becomes high. Contrary, the value of this parameter decreases when multiple entries are present within the image matrix. [24]. Two wavelet-based energy features showed statistical significance when comparing HGGs with BMs: energy computed from the low–low frequency band within the forth image scale (WavEnLL_s-4, $p = 0.0062$) and energy computed from the high–high frequency band within the first image scale (WavEnHH_s-1, $p = 0.0067$). The first parameter (WavEnLL_s-4) showed higher values for HGGs than for BMs (10,272.3 ± 4385.8 versus 6579.94 ± 2732.81), while in the case of the second feature (WavEnHH_s-1), the values were reversed (6.25 ± 3.47 for HGGs versus 10.96 ± 7.11 for BM). Since the LL band frequency carry less important textural information than HH [24], we consider WavEnLL_s-4 values as a predictor of irregularity in the peritumoral zone where gliomas neoplastic infiltration determines nonuniform pixel intensity variations within the edema [41].

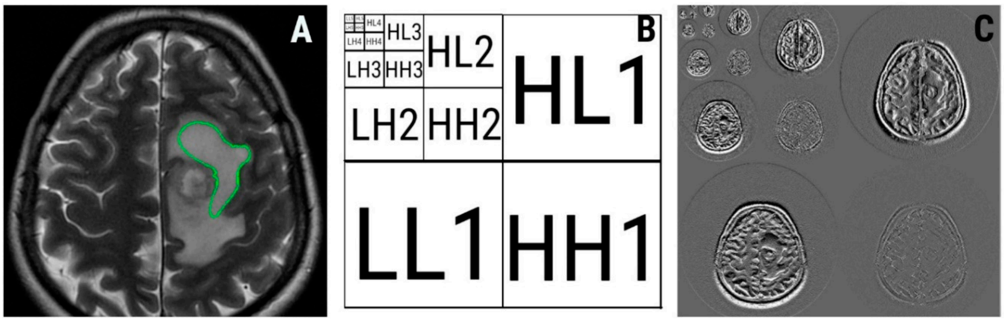

Figure 5. Axial T2-weighted image of a 72-year-old patient with glioblastoma (**A**) and the region of interest (green) used for texture analysis; (**B**) five-level wavelet decomposition diagram; (**C**) five-level wavelet decomposition of (**A**). The numbers represent the decomposition levels. Frequency bands are noted: LL, low–low; HL, high–low; LH, low–high; HH, high–high.

In our study, we demonstrated via texture analysis that the peritumoral edema of HGGs is more heterogeneous and contains higher pixel intensity variations compared to BMs. Additionally, the peritumoral zone of BMs seems to exhibit higher signal intensities on T2W images, probably due to the absence of contamination with tumoral cells. These observations are compatible with previous research. Skogen et al. [41] concluded that the peritumoral edema of glioblastomas expresses a high degree of irregularity on FA and ADC maps, as quantified through the texture parameters entropy and standard deviation of pixel intensity. However, we consider that the use of a classic T2W sequence is more approachable since it is routinely performed on every MRI brain examination and has fewer limitations than DTI [55]. Additionally, it is possible that the TA characteristics of any examined tissue are better highlighted as there are more computed TA features, as they can offer a more complete and complex characterization of the regions of interest.

Signal-to-noise ratio, spatial resolution, magnetic strength as well as other acquisition parameters can have an important influence on TA results [56]. We counteracted such effects through ROI normalization but also by selecting only examinations performed by the same protocol and on the same machine, thus providing a high degree of homogeneity in the current study. Supra-tentorial resection of gliomas is guided by the tumoral margins, visible on the FLAIR sequence because it can provide superior delineation of the white matter lesions [28,57]. The only issue is that the spatial orientation of the FLAIR sequence was volatile in the included examinations (alternating between axial and coronal). To preserve the homogeneity of the lot, a T2W sequence was used that was the same in all studies. The strict selection of supratentorial lesions together with the above-mentioned procedures allowed us to counteract the variations of the textural measurements produced by the use of multiple scanners or different examination protocols [27,58].

When investigating through different modalities (such as spectroscopy or diffusion tensor imaging) the MRI characteristics of peritumoral zones of gliomas, most researchers used a freehand ROI to cover these regions [59,60]. Although such modalities are dependent on the examiners' experience, they produce inconsistencies between the measurements made even by the same researcher [61].

Besides, it is important to consider that the peritumoral cellular infiltration gradually decreases from the tumor edges towards the periphery [62] and can be present even in areas with normal T2 signals [61]. For this reason, it might be possible that a semiautomatic or fully automated technique based on a regional gradient would better encompass the extension of this area.

Advanced MRI techniques such as spectroscopy [13,33,34], perfusion MRI [12], and DTI [41] were shown to be useful in assessing both the tumor and the peritumoral region of gliomas. However, rather than performing advanced techniques and adding on sequences, it is important to quantify and utilize information from images already obtained, as they can carry additional diagnostic information. In this regard, we chose to assess texture information from a basic MRI sequence since it is routinely used in brain examination protocols. However, despite the promising results, texture analysis (and particularly histogram analysis) is not incorporated in most guidelines [63,64]. To enter clinical practice, TA techniques require large prospective multicentric studies and adequate software to be incorporated in workstations.

Our study has several limitations. Firstly, the number of BMs included exceeded one of the HGGs by about 60%, and the overall number of lesions was relatively small. Due to the organization of our healthcare unit, we preferably perform the postsurgical follow-up examinations, while the preoperative assessment is mostly performed in another sector. Secondly, the lack of direct correlation of texture parameters with histological findings in the peritumoral zone can also be viewed as a limitation. Furthermore, owing to its retrospective design, it may have selection bias. Thirdly, a multivariate analysis (such as logistic regression) was also demonstrated to be a useful modality to select discriminative texture features in previous studies [65,66]. To build a robust predictive model, the feature subset should contain mostly uncorrelated parameters [66]. Therefore, our selection method involving Fisher coefficients highlights parameters that besides having a high discriminatory potential, are also well correlated with each other [67]. Thus, this aspect may have affected the overall diagnostic value of our combined prediction model. Additionally, the ROI segmentation employed in this pilot study comprised a single largest cross-section-based delineation instead of a multislice or three-dimensional volume analysis. However, previous studies using the filtration-histogram technique have demonstrated the comparison of single-slice vs. multislice/volume analysis on computer tomography (CT) in primary colorectal cancer for prognostication [68] as well as on MRI in gliomas for IDH versus wild-type differentiation [69]. Interestingly the analysis demonstrated single-slice analysis was significant in predicting prognosis in colorectal cancer on CT [68] and IDH vs. wild-type differentiation in gliomas on MRI [69] and comparable to multislice/volume analysis. It is not therefore clear if there is any "significant" added-value of undertaking multislice/volumetric analysis which not only entails increased analysis time (barrier to adoption in a busy-clinic) and increased operator variability associated with multislice/volume analysis. Another limitation can potentially come from the fact that no intra- or interobserver agreement was assessed. However, previous studies on CT and MRI have demonstrated good reproducibility for filtration-histogram based TA using multicenter clinical validation [70,71], robustness to variation in image acquisition parameters [71–73], and good inter- and intraoperator repeatability (good intraclass correlation from test-retest technique) [74,75]. Additionally, previous research following the same method stated that due to the semiautomatic ROI positioning, this assessment is not necessary [76]. Additionally, the MaZda software used in this article can be regarded as outdated, since the official version had not received improvements in more than 10 years. However, in this study, we used a newly developed Beta version of this software, released in 2016 (Available online: https://data.mendeley.com/datasets/dkxyrzwpzs/1). Although modern dedicated TA software is both free and commercially available, MaZda steel represents a valid TA method, since it provides one of the largest numbers of feature customization, selection, extraction, and processing methods. Additionally, it offers an intuitive interface, and thus the possibility of being used by nonimage processing specialists, such as regular physicians. The MaZda software also enables the use of several classifiers. In this paper, we preferably applied a more conventional approach to the statistical processing of the parameters, since several of these classifiers (such as the artificial neural networks) require big data for an adequate classification procedure.

5. Conclusions

In conclusion, our study showed that high-grade gliomas and solitary brain metastases can be successfully differentiated based on the textural information extracted from the peritumoral zone. Features derived from the histogram analysis, wavelet transformation, and run-length matrix show high discriminatory potential both as stand-alone parameters as well as incorporated in a predictive model. The results of this study support the hypothesis that the textures of the peritumoral edema can reflect the neoplastic cell infiltration of high-grade gliomas, but further research is required to validate this method.

Author Contributions: Conceptualization, P.-A.Ș.; data curation, R.-A.L.; formal analysis, A.L. and L.M.L.; funding acquisition, L.Ș.; investigation, C.C., P.-A.Ș. and A.L.; methodology, P.-A.Ș. and A.L.; project administration, L.Ș. and C.M.M.; resources, L.Ș.; software, R.-A.L.; supervision, C.M.M.; validation, C.O.M.; visualization, C.C. and L.M.L.; writing—original draft preparation, C.C. and P.-A.Ș.; writing—review and editing, C.O.M., R.-A.L. and C.M.M. All authors have read and agreed to the published version of the manuscript.

Funding: This research received no external funding.

Conflicts of Interest: The authors declare no conflict of interest.

References

1. Caravan, I.; Ciortea, C.A.; Contis, A.; Lebovici, A. Diagnostic value of apparent diffusion coefficient in differentiating between high-grade gliomas and brain metastases. *Acta Radiol.* **2017**. [CrossRef] [PubMed]
2. Giese, A.; Westphal, M. Treatment of malignant glioma: A problem beyond the margins of resection. *J. Cancer Res. Clin. Oncol.* **2001**, *127*, 217–225. [CrossRef] [PubMed]
3. Ho, M.-L.; Rojas, R.; Eisenberg, R.L. Cerebral edema. *Am. J. Roentgenol.* **2012**. [CrossRef]
4. Lu, S.; Ahn, D.; Johnson, G.; Cha, S. Peritumoral diffusion tensor imaging of high-grade gliomas and metastatic brain tumors. *Am. J. Neuroradiol.* **2003**, *24*, 937–941. [PubMed]
5. Oh, J.; Cha, S.; Aiken, A.H.; Han, E.T.; Crane, J.C.; Stainsby, J.A.; Wright, G.A.; Dillon, P.D.; Nelson, S.J. Quantitative apparent diffusion coefficients and T2 relaxation times in characterizing contrast enhancing brain tumors and regions of peritumoral edema. *J. Magn. Reason. Imaging* **2005**, *21*, 701–708. [CrossRef]
6. Byrnes, T.J.D.; Barrick, T.R.; Bell, B.A.; Clark, C.A. Diffusion tensor imaging discriminates between glioblastoma and cerebral metastases in vivo. *NMR Biomed.* **2011**, *24*, 54–60. [CrossRef]
7. Blanchet, L.; Krooshof, P.W.T.; Postma, G.J.; Idema, A.J.; Goraj, B.; Heerschap, A.; Buydens, L.M.C. Discrimination between metastasis and glioblastoma multiforme based on morphometric analysis of MR images. *AJNR Am. J. Neuroradiol.* **2011**, *32*, 67–73. [CrossRef]
8. Wang, W.; Steward, C.E.; Desmond, P.M. Diffusion tensor imaging in glioblastoma multiforme and brain metastases: The role of p, q, L, and fractional anisotropy. *AJNR Am. J. Neuroradiol.* **2009**, *30*, 203–208. [CrossRef]
9. Neves, S.; Mazal, P.R.; Wanschitz, J.; Rudnay, A.C.; Drlicek, M.; Czech, T.; Wüstinger, C.; Budka, H. Pseudogliomatous growth pattern of anaplastic small cell carcinomas metastatic to the brain. *Clin. Neuropathol.* **2001**, *20*, 38–42.
10. Lee, E.J.; terBrugge, K.; Mikulis, D.; Choi, D.S.; Bae, J.M.; Lee, S.K.; Moon, S.Y. Diagnostic value of peritumoral minimum apparent diffusion coefficient for differentiation of glioblastoma multiforme from solitary metastatic lesions. *AJR Am. J. Roentgenol.* **2011**, *196*, 71–76. [CrossRef]
11. Upadhyay, N.; Waldman, A.D. Conventional MRI evaluation of gliomas. *Br. J. Radiol.* **2011**, *84*, 107–111. [CrossRef] [PubMed]
12. Price, S.J.; Young, A.M.H.; Scotton, W.J.; Ching, J.; Mohsen, L.A.; Boonzaier, N.R.; Lupsor, V.C.; Griffiths, J.R.; McLean, M.A.; Larkin, T.J. Multimodal MRI can identify perfusion and metabolic changes in the invasive margin of glioblastomas. *J. Magn. Reason. Imaging* **2016**, *43*, 487–494. [CrossRef]
13. Price, S.J.; Green, H.a.L.; Dean, A.F.; Joseph, J.; Hutchinson, P.J.; Gillard, J.H. Correlation of MR relative cerebral blood volume measurements with cellular density and proliferation in high-grade gliomas: An image-guided biopsy study. *AJNR Am. J. Neuroradiol.* **2011**, *32*, 501–506. [CrossRef] [PubMed]

14. Doi, K. Computer-Aided Diagnosis in Medical Imaging: Historical Review, Current Status and Future Potential. *Comput. Med. Imaging Graph.* **2007**, *31*, 198–211. [CrossRef]
15. Tourassi, G.D. Journey toward computer-aided diagnosis: Role of image texture analysis. *Radiology* **1999**, *213*, 317–320. [CrossRef] [PubMed]
16. Livens, S.; Scheunders, P.; Wouwer, G.; Dyck, D. Wavelets for texture analysis, an overview. In Proceedings of the 6th International Conference on Image Processing and its Applications, Dublin, Ireland, 14–17 July 1997; pp. 581–585. [CrossRef]
17. Raveane, W.; Arrieta, M.A.G. Texture Classification with Neural Networks. In *Distributed Computing and Artificial Intelligence*; Omatu, S., Neves, J., Rodriguez, J.M.C., Paz Santana, J.F., Gonzalez, S.R., Eds.; Springer International Publishing: Cham, Switzerland, 2013; pp. 325–332. [CrossRef]
18. Soni, N.; Priya, S.; Bathla, G. Texture Analysis in Cerebral Gliomas: A Review of the Literature. *AJNR Am. J. Neuroradiol.* **2019**, *40*, 928–934. [CrossRef]
19. Varghese, B.A.; Cen, S.Y.; Hwang, D.H.; Duddalwar, V.A. Texture Analysis of Imaging: What Radiologists Need to Know. *AJR Am. J. Roentgenol.* **2019**, *212*, 520–528. [CrossRef]
20. Kang, Y.; Choi, S.H.; Kim, Y.-J.; Kim, K.G.; Sohn, C.-H.; Kim, J.-H.; Yun, T.J.; Chang, K.-H. Gliomas: Histogram analysis of apparent diffusion coefficient maps with standard- or high-b-value diffusion-weighted MR imaging—Correlation with tumor grade. *Radiology* **2011**, *261*, 882–890. [CrossRef]
21. Raja, R.; Sinha, N.; Saini, J.; Mahadevan, A.; Rao, K.N.; Swaminathan, A. Assessment of tissue heterogeneity using diffusion tensor and diffusion kurtosis imaging for grading gliomas. *Neuroradiology* **2016**, *58*, 1217–1231. [CrossRef]
22. Strzelecki, M.; Szczypinski, P.; Materka, A.; Klepaczko, A. A software tool for automatic classification and segmentation of 2D/3D medical images. *Nucl. Instrum. Methods Phys. Res. Sect. A Accel. Spectrom. Detect. Assoc. Equip.* **2013**, *702*, 137–140. [CrossRef]
23. Collewet, G.; Strzelecki, M.; Mariette, F. Influence of MRI acquisition protocols and image intensity normalization methods on texture classification. *Magn. Reason. Imaging* **2004**, *22*, 81–91. [CrossRef] [PubMed]
24. Materka, A. Texture analysis methodologies for magnetic resonance imaging. *Dialogues Clin. Neurosci.* **2004**, *6*, 243–250. [PubMed]
25. Herlidou-Même, S.; Constans, J.M.; Carsin, B.; Olivie, D.; Eliat, P.A.; Nadal-Desbarats, L.; Gondry, C.; Rumeur, E.; Idy-Perreti, I.; de Certaines, J.D. MRI texture analysis on texture test objects, normal brain and intracranial tumors. *Magn. Reason. Imaging* **2003**, *21*, 989–993. [CrossRef]
26. DeLong, E.R.; DeLong, D.M.; Clarke-Pearson, D.L. Comparing the areas under two or more correlated receiver operating characteristic curves: A nonparametric approach. *Biometrics* **1988**, *44*, 837–845. [CrossRef]
27. Larroza, A.; Bodí, V.; Moratal, D. Texture Analysis in Magnetic Resonance Imaging: Review and Considerations for Future Applications. In *Assessment of Cellular and Organ Function and Dysfunction Using Direct and Derived MRI Methodologies*; Constantinides, C., Ed.; IntechOpen: London, UK, 2016. [CrossRef]
28. Muccio, C.F.; Tedeschi, E.; Ugga, L.; Cuocolo, R.; Esposito, G.; Caranci, F. Solitary Cerebral Metastases vs. High-grade Gliomas: Usefulness of Two MRI Signs in the Differential Diagnosis. *Anticancer Res.* **2019**, *39*, 4905–4909. [CrossRef]
29. Han, C.; Huang, S.; Guo, J.; Zhuang, X.; Han, H. Use of a high b-value for diffusion weighted imaging of peritumoral regions to differentiate high-grade gliomas and solitary metastases. *J. Magn. Reason. Imaging* **2015**, *42*, 80–86. [CrossRef]
30. Pavlisa, G.; Rados, M.; Pavic, L.; Potocki, K.; Mayer, D. The differences of water diffusion between brain tissue infiltrated by tumor and peritumoral vasogenic edema. *Clin. Imaging* **2009**, *33*, 96–101. [CrossRef]
31. Server, A.; Kulle, B.; Maehlen, J.; Josefsen, R.; Schellhorn, T.; Kumar, T.; Langberg, P.H.; Nakstad, P.H. Quantitative apparent diffusion coefficients in the characterization of brain tumors and associated peritumoral edema. *Acta Radiol.* **2009**, *50*, 682–689. [CrossRef]
32. Bertossi, M.; Virgintino, D.; Maiorano, E.; Occhiogrosso, M.; Roncali, L. Ultrastructural and morphometric investigation of human brain capillaries in normal and peritumoral tissues. *Ultrastruct. Pathol.* **1997**, *21*, 41–49. [CrossRef]
33. Tsougos, I.; Svolos, P.; Kousi, E.; Fountas, K.; Theodorou, K.; Fezoulidis, I.; Theodorou, K.; Frezoulidis, I.; Kapsalaki, E. Differentiation of glioblastoma multiforme from metastatic brain tumor using proton magnetic resonance spectroscopy, diffusion and perfusion metrics at 3 T. *Cancer Imaging* **2012**, *12*, 423–436. [CrossRef]

34. Yan, J.-L.; Li, C.; Boonzaier, N.R.; Fountain, D.M.; Larkin, T.J.; Matys, T.; van der Hoorn, A.; Price, S.J. Multimodal MRI characteristics of the glioblastoma infiltration beyond contrast enhancement. *Ther. Adv. Neurol. Disord.* **2019**, *12*, 1756286419844664. [CrossRef] [PubMed]
35. Wijnen, J.P.; Idema, A.J.S.; Stawicki, M.; Lagemaat, M.W.; Wesseling, P.; Wright, A.J.; Scheenen, T.W.J.; Heerschap, A. Quantitative short echo time 1H MRSI of the peripheral edematous region of human brain tumors in the differentiation between glioblastoma, metastasis, and meningioma. *J. Magn. Reason. Imaging* **2012**, *36*, 1072–1082. [CrossRef]
36. Jain, R.; Poisson, L.M.; Gutman, D.; Scarpace, L.; Hwang, S.N.; Holder, C.A.; Wintermark, M.; Rao, A.; Colen, R.R.; Kirby, J.; et al. Outcome prediction in patients with glioblastoma by using imaging, clinical, and genomic biomarkers: Focus on the nonenhancing component of the tumor. *Radiology* **2014**, *272*, 484–493. [CrossRef] [PubMed]
37. Bette, S.; Huber, T.; Wiestler, B.; Boeckh-Behrens, T.; Gempt, J.; Ringel, F.; Meyer, B.; Zimmer, C.; Kirsche, J.S. Analysis of fractional anisotropy facilitates differentiation of glioblastoma and brain metastases in a clinical setting. *Eur. J. Radiol.* **2016**, *85*, 2182–2187. [CrossRef]
38. Ryu, Y.J.; Choi, S.H.; Park, S.J.; Yun, T.J.; Kim, J.-H.; Sohn, C.-H. Glioma: Application of whole-tumor texture analysis of diffusion-weighted imaging for the evaluation of tumor heterogeneity. *PLoS ONE* **2014**, *9*, e108335. [CrossRef]
39. Kinoshita, M.; Sakai, M.; Arita, H.; Shofuda, T.; Chiba, Y.; Kagawa, N.; Watanabe, Y.; Hashimoto, N.; Fujimoto, Y.; Yoshimine, T.; et al. Introduction of High Throughput Magnetic Resonance T2-Weighted Image Texture Analysis for WHO Grade 2 and 3 Gliomas. *PLoS ONE* **2016**, *11*, e0164268. [CrossRef]
40. Skogen, K.; Schulz, A.; Dormagen, J.B.; Ganeshan, B.; Helseth, E.; Server, A. Diagnostic performance of texture analysis on MRI in grading cerebral gliomas. *Eur. J. Radiol.* **2016**, *85*, 824–829. [CrossRef]
41. Skogen, K.; Schulz, A.; Helseth, E.; Ganeshan, B.; Dormagen, J.B.; Server, A. Texture analysis on diffusion tensor imaging: Discriminating glioblastoma from single brain metastasis. *Acta Radiol.* **2019**, *60*, 356–366. [CrossRef]
42. Mouthuy, N.; Cosnard, G.; Abarca-Quinones, J.; Michoux, N. Multiparametric magnetic resonance imaging to differentiate high-grade gliomas and brain metastases. *J. Neuroradiol.* **2012**, *39*, 301–307. [CrossRef]
43. Artzi, M.; Liberman, G.; Blumenthal, D.T.; Aizenstein, O.; Bokstein, F.; Ben Bashat, D. Differentiation between vasogenic edema and infiltrative tumor in patients with high-grade gliomas using texture patch-based analysis. *J. Magn. Reason. Imaging* **2018**. [CrossRef] [PubMed]
44. Szczypinski, P.M.; Klepaczko, A. *MaZda—A Framework for Biomedical Image Texture Analysis and Data Exploration In Biomedical Texture Analysis: Fundamentals, Tools and Challenges*; Szczypinski, P.M., Klepaczko, A., Depeursinge, A., Al-Kadi, O.S., Mitchell, J.R., Eds.; Academic Press: Cambridge, MA, USA, 2017.
45. Miles, K.A.; Ganeshan, B.; Hayball, M.P. CT texture analysis using the filtration-histogram method: What do the measurements mean? *Cancer Imaging* **2013**, *13*, 400–406. [CrossRef] [PubMed]
46. Huang, Y.-Q.; Liang, H.-Y.; Yang, Z.-X.; Ding, Y.; Zeng, M.-S.; Rao, S.-X. Value of MR histogram analyses for prediction of microvascular invasion of hepatocellular carcinoma. *Medicine* **2016**, *95*, e4034. [CrossRef] [PubMed]
47. Castellano, G.; Bonilha, L.; Li, L.M.; Cendes, F. Texture analysis of medical images. *Clin. Radiol.* **2004**, *59*, 1061–1069. [CrossRef] [PubMed]
48. Mayerhoefer, M.E.; Breitenseher, M.J.; Kramer, J.; Aigner, N.; Hofmann, S.; Materka, A. Texture analysis for tissue discrimination on T1-weighted MR images of the knee joint in a multicenter study: Transferability of texture features and comparison of feature selection methods and classifiers. *J. Magn. Reason. Imaging* **2005**, *22*, 674–680. [CrossRef]
49. Kairuddin, W.N.H.W.; Mahmud, W.M.H.W. Texture Feature Analysis for Different Resolution Level of Kidney Ultrasound Images. *IOP Conf. Ser. Mater. Sci. Eng.* **2017**, *226*, 12136. [CrossRef]
50. Grey-Level Run Length Matrix (GLRLM) n.d. Available online: https://www.lifexsoft.org/index.php/resources/19-texture/radiomic-features/68-grey-level-run-length-matrix-glrlm (accessed on 21 May 2020).
51. cerr/CERR. GitHub n.d. Available online: https://github.com/cerr/CERR (accessed on 21 May 2020).
52. Yadav, A.K.; Roy, R.; Ch, S.; Kumar, E.; Praveen, A. Vaishali, Wavelet Based Texture Analysis for MedicalImages. *Int. J. Adv. Res. Electr. Electron. Instrum. Eng.* **2015**. [CrossRef]
53. Classifying Image data n.d. Available online: https://www.debugmode.com/imagecmp/classify.htm (accessed on 21 May 2020).
54. Dutra da Silva, R.; Minneto, R.; Schwartz, W.; Pedrini, H. Satellite Image Segmentation Using Wavelet Transform Based on Color and Texture Features. In *Advances in Visual Computing: 4th International Symposium,*

ISVC 2008, Las Vegas, NV, USA, 1–3 December 2008; Boyle, R., Parvin, B., Koracin, D., Porikli, F., Peters, J., Klosowski, J., Eds.; Part, II. Springer: Berlin, Germany, 2008; pp. 114–132.

55. Mori, S.; Zhang, J. Principles of Diffusion Tensor Imaging and Its Applications to Basic Neuroscience Research. *Neuron* **2006**, *51*, 527–539. [CrossRef]
56. Buch, K.; Kuno, H.; Qureshi, M.M.; Li, B.; Sakai, O. Quantitative variations in texture analysis features dependent on MRI scanning parameters: A phantom model. *J. Appl. Clin. Med. Phys.* **2018**, *19*, 253–264. [CrossRef]
57. Duffau, H. Long-term outcomes after supratotal resection of diffuse low-grade gliomas: A consecutive series with 11-year follow-up. *Acta Neurochir.* **2016**, *158*, 51–58. [CrossRef] [PubMed]
58. Nabors, L.B.; Portnow, J.; Ammirati, M.; Baehring, J.; Brem, H.; Butowski, N.; Fenstermaker, R.A.; Forsyth, P.; Hattangadi-Gluth, J.; Holdoff, M.; et al. NCCN Guidelines Insights: Central Nervous System Cancers, Version 1.2017. *J. Natl. Compr. Cancer Netw.* **2017**, *15*, 1331–1345. [CrossRef]
59. Blystad, I.; Warntjes, J.B.M.; Smedby, Ö.; Lundberg, P.; Larsson, E.-M.; Tisell, A. Quantitative MRI for analysis of peritumoral edema in malignant gliomas. *PLoS ONE* **2017**, *12*, e0177135. [CrossRef] [PubMed]
60. Kousi, E.; Tsougos, I.; Tsolaki, E.; Fountas, K.N.; Theodorou, K.; Fezoulidis, I.; Kapsalaki, E.; Kappas, C. Spectroscopic Evaluation of Glioma Grading at 3T: The Combined Role of Short and Long TE. *Sci. World J.* **2012**, *2012*, 546171. [CrossRef]
61. Lee, K.H. *Computers in Nuclear Medicine: A Practical Approach*; SNMMI: Reston, VA, USA, 2005; pp. 106–112.
62. Pirzkall, A.; McKnight, T.R.; Graves, E.E.; Carol, M.P.; Sneed, P.K.; Wara, W.W.; Nelson, S.J.; Verhey, L.J.; Larson, D.A. MR-spectroscopy guided target delineation for high-grade gliomas. *Int. J. Radiat. Oncol. Biol. Phys.* **2001**, *50*, 915–928. [CrossRef]
63. Price, S.J.; Gillard, J.H. Imaging biomarkers of brain tumour margin and tumour invasion. *Br. J. Radiol.* **2011**, *84*, 159–167. [CrossRef]
64. Herr, K.; Muglia, V.F.; Koff, W.J.; Westphalen, A.C. Imaging of the adrenal gland lesions. *Radiol. Bras.* **2014**, *47*, 228–239. [CrossRef]
65. Yagi, T.; Yamazaki, M.; Ohashi, R.; Ogawa, R.; Ishikawa, H.; Yoshimura, N.; Tsuchida, M.; Ajioka, Y.; Aoyama, H. HRCT texture analysis for pure or part-solid ground-glass nodules: Distinguishability of adenocarcinoma in situ or minimally invasive adenocarcinoma from invasive adenocarcinoma. *Jpn. J. Radiol.* **2018**, *36*, 113–121. [CrossRef]
66. Hassan, I.; Kotrotsou, A.; Bakhtiari, A.S.; Thomas, G.A.; Weinberg, J.S.; Kumar, A.J.; Sawaya, R.; Luedi, M.K.; Zinn, P.O.; Colen, R.R. Radiomic Texture Analysis Mapping Predicts Areas of True Functional MRI Activity. *Sci. Rep.* **2016**, *6*, 25295. [CrossRef]
67. Mayerhoefer, M.E.; Breitenseher, M.; Amann, G.; Dominkus, M. Are signal intensity and homogeneity useful parameters for distinguishing between benign and malignant soft tissue masses on MR images? Objective evaluation by means of texture analysis. *Magn. Reason. Imaging* **2008**, *26*, 1316–1322. [CrossRef]
68. Ng, F.; Kozarski, R.; Ganeshan, B.; Goh, V. Assessment of tumor heterogeneity by CT texture analysis: Can the largest cross-sectional area be used as an alternative to whole tumor analysis? *Eur. J. Radiol.* **2013**, *82*, 342–348. [CrossRef] [PubMed]
69. Lewis, M.A.; Ganeshan, B.; Barnes, A.; Bisdas, S.; Jaunmuktane, Z.; Brandner, S.; Endozo, R.; Groves, A.; Thust, S.C. Filtration-histogram based magnetic resonance texture analysis (MRTA) for glioma IDH and 1p19q genotyping. *Eur. J. Radiol.* **2019**, *113*, 116–123. [CrossRef] [PubMed]
70. Win, T.; Miles, K.A.; Janes, S.M.; Ganeshan, B.; Shastry, M.; Endozo, R.; Meagher, M.; Shortman, R.I.; Wan, S.; Kayani, I.; et al. Tumor heterogeneity and permeability as measured on the CT component of PET/CT predict survival in patients with non-small cell lung cancer. *Clin. Cancer Res.* **2013**, *19*, 3591–3599. [CrossRef]
71. Dohan, A.; Gallix, B.; Guiu, B.; Le Malicot, K.; Reinhold, C.; Soyer, P.; Bennouna, J.; Ghiringhelli, F.; Barbier, E.; Boige, V. Early evaluation using a radiomic signature of unresectable hepatic metastases to predict outcome in patients with colorectal cancer treated with FOLFIRI and bevacizumab. *Gut* **2020**, *69*, 531–539. [CrossRef]
72. Miles, K.A.; Ganeshan, B.; Griffiths, M.R.; Young, R.C.D.; Chatwin, C.R. Colorectal cancer: Texture analysis of portal phase hepatic CT images as a potential marker of survival. *Radiology* **2009**, *250*, 444–452. [CrossRef]
73. Yasaka, K.; Akai, H.; Mackin, D.; Court, L.; Moros, E.; Ohtomo, K.; Kiryu, S. Precision of quantitative computed tomography texture analysis using image filtering: A phantom study for scanner variability. *Medicine* **2017**, *96*, e6993. [CrossRef] [PubMed]

74. Gourtsoyianni, S.; Doumou, G.; Prezzi, D.; Taylor, B.; Stirling, J.J.; Taylor, N.J.; Siddique, M.; Cook, C.J.R.; Glyme-Jones, R.; Goh, V. Primary Rectal Cancer: Repeatability of Global and Local-Regional MR Imaging Texture Features. *Radiology* **2017**, *284*, 552–561. [CrossRef]
75. Cui, H.W.; Devlies, W.; Ravenscroft, S.; Heers, H.; Freidin, A.J.; Cleveland, R.O.; Ganeshan, B.; Turney, B.W. CT Texture Analysis of Ex Vivo Renal Stones Predicts Ease of Fragmentation with Shockwave Lithotripsy. *J. Endourol.* **2017**, *31*, 694–700. [CrossRef]
76. Mayerhoefer, M.E.; Schima, W.; Trattnig, S.; Pinker, K.; Berger-Kulemann, V.; Ba-Ssalamah, A. Texture-based classification of focal liver lesions on MRI at 3.0 Tesla: A feasibility study in cysts and hemangiomas. *J. Magn. Reason. Imaging* **2010**, *32*, 352–359. [CrossRef]